

**IMAGING HORSERADISH PEROXIDASE UNDER
ELECTROCHEMICAL CONDITIONS**

Baohua Zhang

School of Natural and Environmental Sciences

Newcastle University

A thesis submitted for the degree of

Doctor of Philosophy

September 2021

Abstract

In this work, potential dependent electrochemical characterisation has been performed on horseradish peroxidase (HRP) molecules immobilised on annealed highly oriented pyrolytic graphite (HOPG) surface immersed in phosphate buffer solution (PBS). Electrochemical impedance spectroscopy (EIS) was applied to investigate the HRP molecular capacitance. The observed HRP capacitance shows significant potential dependency, which is analogous to that of a typical metal oxide semiconductor (MOS) capacitor fabricated with p-type semiconductor materials. Accumulation region and depletion region has been observed from the capacitance (C)-potential (U) curve of the HRP molecules, and the “flat band potential”, at which there is no potential drop within the semiconductor layer, has been determined as the potential where dC/dU curve peaks. An MOS capacitor approximation is proposed to describe the potential dependent capacitance behaviour of HRP molecules.

Scanning electrochemical potential microscopy (SECPM) and electrochemical scanning tunnelling microscopy (EC-STM) has been applied to monitor the potential drop in HRP molecules at single molecular level. SECPM maps the potential distribution within the electrochemical double layer (EDL) and can resolve HRP molecules with Angstrom resolution. Potential drop within HRP molecules is reflected as potential dependent morphological variation in SECPM images. The observed HRP apparent size peaks at the flat band potential. Similar potential dependency of HRP apparent size is observed using EC-STM, as the potential drop being an influence on the bias voltage between tip and substrate.

SECPM was also used to directly measure the EDL profile with alternating electrode potential and electrolyte concentration. An exponential potential decay with reference to the tip-substrate separation has been observed as predicted by Gouy-Chapman-Stern model. Delayed response of potential decay, with significant dependence on the local electrical field and ionic strength, was also observed at close tip-substrate distance. A quantitative approach based on a novel mechanism which suggests high resolution SECPM imaging could be attributed to direct electron exchange between tip and substrate is proposed to interpret the delayed response of potential decay.

Acknowledgement

I would first like to thank all the heroes world widely working in the front lines to fight against the coronavirus. The world benefits from their selfless contribution and noble sacrifice. Without their efforts to control the spread of COVID-19, I cannot stay safe and sound to finish this thesis.

This work will not be complete without the guidance from my supervisor, Prof. Ulrich Stimming, who is a role model to me not only about scientific research, but also about working attitude. I must thank him for offering me this wonderful opportunity to work in Newcastle University and helping me through the experimental design and data analysis.

I am also deeply grateful to Dr. Benjamin Horrocks for all his help on the interpretation of SECPM potential profiling data. I benefit a lot from his expertise in physics and mathematics.

I would like to thank all the past and present members in this group that have helped me generously in scientific research and everyday life. Jingying introduced me how to perform the SPM experiments and Qiaochu guided me through the EIS theory, these two techniques consist the major part of the work in this thesis. Felix, Jack and Jochen helped a lot with the electrochemical experiments and also introduced me to the well-known bar culture in UK. Sameera impressed me so much by her persistence in work. It is a pity that I do not have the opportunity to work closely with Arlete, Arup, Faye and Jiabin but I am grateful to have the chance to work in the same group with all these amazing people.

I must thank Shaoshuai Jiang and Dr. Yi Jin for the valuable friendship I gained in UK. My life here would be more challenging without your companionship.

I am extremely grateful to my mother and my sister, who keep being nothing but helpful and supportive to me since the beginning of my life.

Last but not the least, to my late father: I did it.

Table of Contents

Abstract.....	i
Acknowledgement.....	ii
Table of Contents.....	iii
List of Figures.....	vii
List of Tables.....	xiv
Chapter 1. Introduction.....	1
1.1 A Brief History of STM and AFM.....	1
1.2 Application of SPM Technology in the Investigation of Biomolecules.....	2
1.3 Mechanism of Immobilised Heme Proteins as Bioelectrocatalysis.....	3
1.4 SECPM in the Investigation of Electrochemical Properties of Immobilised HRP 7	
1.5 SECPM for the Direct Probing of EDL Structure.....	9
1.6 Research Objectives.....	10
Chapter 2. Fundamentals.....	12
2.1 Electrochemical Double Layer.....	12
2.1.1 Helmholtz Model.....	12
2.1.2 Gouy-Chapman Model.....	13
2.1.3 Gouy-Chapman-Stern Model.....	15
2.1.4 Specific Adsorption.....	16
2.2 Electrochemical Impedance Spectroscopy.....	18
2.2.1 Concepts and Principles.....	18
2.2.2 Classic Electrochemical Reaction Models and the Corresponding Equivalent Circuits.....	19
2.2.3 EIS Application on Lithium-ion Batteries: Determining the State of Health 24	
2.3 Scanning Tunnelling Microscopy.....	29

2.3.1	Quantum Tunnelling Effect.....	29
2.3.2	STM Setup.....	31
2.3.3	STM Operation Modes.....	31
2.3.4	Electrochemical Scanning Tunnelling Microscopy.....	33
2.4	Scanning Electrochemical Potential Microscopy.....	34
2.4.1	SECPM Setup and Principles.....	35
2.4.2	SECPM Operation Modes.....	36
2.4.3	SECPM Potential Profiling.....	37
2.4.4	SECPM Tip Geometry.....	40
Chapter 3.	Experimental.....	42
3.1	Chemical and Materials.....	42
3.1.1	Chemicals.....	42
3.1.2	Preparation of Solutions and Electrolytes.....	43
3.2	Scanning Probe Microscopy Instruments.....	43
3.2.1	Atomic Force Microscopy.....	44
3.2.2	Scanning Tunnelling Microscopy.....	46
3.2.3	Scanning Electrochemical Potential Microscopy.....	49
3.3	Probe Fabrication.....	49
3.3.1	Probes for Imaging.....	50
3.3.2	Probes for SECPM Potential Profiling.....	51
3.4	Working Electrode.....	53
3.5	Counter and Reference Electrode.....	54
3.5.1	Counter Electrode.....	54
3.5.2	Reference Electrode.....	55
3.6	Electrochemical Setups and Instruments.....	57
3.6.1	Electrochemical Cell.....	57
3.6.2	Potentiostat.....	58
3.7	Sample Preparation.....	58

3.7.1	HOPG Functionalization	58
3.7.2	HRP Immobilisation	59
Chapter 4.	Potential Dependent Capacitance Behaviour of Horseradish Peroxidase	
	60	
4.1	Electrode Surface Morphology: SPM Characterisation	60
4.2	Electrochemical Characterisation: Cyclic Voltammetry	63
4.3	Potential Dependent Capacitance Measurement: Electrochemical Impedance Spectroscopy	66
4.3.1	Freshly Cleaved HOPG and Annealed HOPG.....	66
4.3.2	Annealed HOPG with HRP Adsorption: EIS Analysis	75
4.3.3	Annealed HOPG with HRP Adsorption: MOS Approximation	84
4.3.4	HRP-catalysed Oxygen Reduction Reactions	87
4.4	Conclusions.....	89
Chapter 5.	Potential Dependent Imaging of Horseradish Peroxidase Molecules Using Electrochemical Scanning Probe Microscopy	90
5.1	SECPM Imaging Single HRP Molecules on Annealed HOPG Surface	90
5.1.1	Experimental Details.....	90
5.1.2	SECPM Imaging HRP Molecules at Single Molecular Level.....	91
5.1.3	Discussions: Directly Monitoring the Potential Drop within HRP Molecular Structure.....	101
5.2	EC-STM Imaging HRP Molecules Immobilised on Annealed HOPG Surface	
	105	
5.2.1	Experimental Details.....	105
5.2.2	EC-STM Imaging: Single HRP Molecule and HRP Dimer	106
5.2.3	Discussions: Indirect Potential Drop Monitoring, Influence on the Bias Voltage	
	113	
5.3	Conclusions.....	116
Chapter 6.	Direct Probing of Electrochemical Double Layer Using Scanning Electrochemical Potential Microscopy	118

6.1	Debye Length Calculation and Experimental Parameter Selection.....	118
6.2	Potential Profiling Curve Analysis	120
6.3	Discussions	131
6.4	Conclusions	135
Chapter 7.	Conclusions	136
References	142

List of Figures

Figure 1.1 Chemical structures of heme groups: (A) heme <i>b</i> , (B) heme <i>c</i> , and (C) heme <i>d</i> ₁ . The Fisher numbering system for heme substituents is shown in (A). The curve in (B) represents a peptide segment; usually two residues separate the two Cys, and the His axial ligand follows the Cys attached to position 4. Heme <i>o</i> has a hydroxyfarnesyl group in place of vinyl 2 in (A), and heme <i>a</i> has a hydroxyfarnesyl group in place of vinyl 2 and a formyl group in place of methyl 8(Bowman & Bren, 2008).	4
Figure 1.2 Structural and physicochemical features of the heme proteins reviewed in the present work. The projected area at a surface and the molecular volume were estimated from the three-dimensional structure of a representative species of the family (Ranieri et al., 2019).	5
Figure 2.1 Helmholtz model for EDL at solid-liquid interface, where the metal electrode is negatively charged and the charged is balanced by counter positive ions placed at an increment of <i>d</i> away from the solid surface.	13
Figure 2.2 Illustration of Gouy-Chapman model for EDL.	14
Figure 2.3 Illustration of Gouy-Chapman-Stern model for EDL structure. <i>C_H</i> is the Helmholtz layer capacitance and <i>C_D</i> is the diffuse layer capacitance.	16
Figure 2.4 Illustration of Gouy-Chapman-Stern model modified by Graham with specific and non-specific ion-electrode interactions.	17
Figure 2.5 Nyquist plot for the equivalent circuit with a single capacitor.	20
Figure 2.6 Nyquist plot for the equivalent circuit of a resistor and a capacitor connected in series.	20
Figure 2.7 Diagram for a simplified Randles cell.	21
Figure 2.8 (A) Nyquist plot of a simplified Randles cell with input signal frequency close to zero; (B) The equivalent circuit represent the Randles cell corresponding to (A). .	22
Figure 2.9 Equivalent circuit for a Randle cell under high frequency input signal.	22
Figure 2.10 Nyquist plot for the equivalent circuit in figure 2.9.(Bard & Faulkner, 2000)	23
Figure 2.11 A general illustration of a Nyquist plot for a simplified Randles cell.(Bard & Faulkner, 2000).	23
Figure 2.12 Impedance spectrum representated by Nyquist plot and Bode plot.(Choi et al., 2020)	24

Figure 2.13 A simplified equivalent circuit for a lithium-ion battery half-cell system and the corresponding Nyquist plot. R_b is the bulk resistance of the cell; R_{SEI} and CPE_{SEI} stand for the resistance and capacitance (constant phase element) of the interfacial layer, respectively; R_{ct} and $CPE_{electrode}$ are charge-transfer resistance and double layer capacitance; $W_{Warburg}$ represents the diffusional effects of lithium ion on the host material. (Choi et al., 2020).....	25
Figure 2.14 Nyquist plot for lithium-ion battery with decreasing (A) SOC; (B) SOH; (C) temperature. (Westerhoff et al., 2016)	26
Figure 2.15 Shifts in the process frequencies depending on various factors of an impedance spectrum: a) impedance spectra, b) state of charge, c) state of health, d) temperature. (Westerhoff et al., 2016)	28
Figure 2.16 Diagram of the energy levels in an STM setup. (Baier, 2010).....	30
Figure 2.17 Scanning tunnelling microscopy setup. (Hugelmann, 2004)	31
Figure 2.18 Operation of STM technique. (A) Constant current mode; (B) Constant height mode. Both modes with scheme of detected tunnelling current. The red part represents atoms with LDOS different from the blue part.	33
Figure 2.19 Schematic drawing of an electrochemical scanning tunnelling microscope setup.....	34
Figure 2.20 Schematic drawing of an SPM setup with both electrochemical scanning tunnelling microscopy and scanning electrochemical potential microscopy integrated.	35
Figure 2.21 Potential measured at the probe ϕ_{pr} as it approaches the Au(111) surface; where ϕ_{pr0} is the OCP of the tip far away from the electrode surface. (Woo et al., 2004)	38
Figure 2.22 (a) Potentiometric approach curves on the Pt foil surface held respectively at +400 mV (filled black circles), +300 mV (filled grey triangles), and +200 mV vs PtPPy (empty grey boxes); (b) Influence of the electrolyte concentration on the double-layer profile obtained by approaching the Pt foil surface held at +400 mV vs PtPPy at 20 nm/s in 10 μ M (filled black circles), 100 μ M (filled grey triangles), and 1 mM (empty grey boxes) KCl.	39
Figure 2.23 The metallic protrusion apexes used in the simulation: (a) Geometry 1, (b) Geometry 2, and (c) Geometry 3. (Hamou et al., 2010b).....	41
Figure 3.1 Bruker STM setup. (A) Bruker multimode 8 SPM base; (B) Bruker Nanoscope V controller and universal bipotentiostat.	44

Figure 3.2 AFM setup and tip holders. (A): AFM head installed on the scanner; (B): MFMA stainless steel tip holder for AFM in air; (C): MTFML glass tip holder for AFM in liquid; (D): MMTMEC glass tip holder for EC-AFM.	45
Figure 3.3 STM converter head and tip holder.	46
Figure 3.4 EC-STM fluid cell, exploded (left) and assembled (right).....	47
Figure 3.5 Ring-shape counter electrode holding the electrolyte for EC-STM and SECPM.....	48
Figure 3.6 Environmental control hood to maintain the noble gas atmosphere and humidity.....	48
Figure 3.7 SECPM head and tip holder.	49
Figure 3.8 Schematic drawing of the tip insulating using melted plastic on top of a temperature-controlled soldering iron.....	51
Figure 3.9 Preparation of SECPM potential profiling probes.	52
Figure 3.10 SECPM potential profiling probe imaged by SEM from different angles.	52
Figure 3.11 SECPM potential profiling probe installation. (A) The probe holding tube with curvature; (B) Curvature of metal wire used to prepare the probes; (C) Probe installation; (D) illustration of relative position between the probe and the substrate.....	53
Figure 3.12 Schematic drawing for gold-gold oxide RE preparation.....	56
Figure 3.13 Modified SECPM head for electrochemical characterisation.	57
Figure 4.1 Images of f-HOPG and a-HOPG in 10 mM PBS (pH 7.4) captured by AFM in liquid (A and B), EC-STM (C and D) and SECPM (E and F).	61
Figure 4.2 AFM images of a-HOPG surfaces with HRP modification done by drop casting technique using (A) 1mg/mL, (B) 0.1 mg/mL and (C and D) 0.04 mg/mL HRP solutions.....	63
Figure 4.3 CV of (A1) f-HOPG, (B) a-HOPG and (C1) HRP-HOPG recorded in 10 mM PBS (pH 7.4) in argon atmosphere at various scan rates (black: 20 mV/s, green 50 mV/s, blue: 100 mV/s, red: 200 mV/s). (A2) and (C2) are amplification of the corresponding parts (in the red square) in (A1) and (C1), respectively.	64
Figure 4.4 Impedance spectra recorded on f-HOPG surface in 10 mM PBS. (A): Substrate potential changing pattern according to which the impedance spectra were recorded. (B): Nyquist plot. (C): Bode plot.....	68
Figure 4.5 Impedance spectra recorded on a-HOPG surface in 10 mM PBS. (A): Substrate potential changing pattern according to which the impedance spectra were recorded. (B): Nyquist plot. (C): Bode plot.....	69

Figure 4.6 Equivalent circuit model to analysis the impedance spectra of f-HOPG and a-HOPG in PBS. R_s is the solution ohmic resistance, C_{EDL} is the electrochemical double layer capacitance and R_{ct} is the charge transfer resistance of the electrode surface.....	70
Figure 4.7 Potential Dependency of R_{ct} for f-HOPG electrode.....	72
Figure 4.8 Potential Dependency of R_{ct} for a-HOPG electrode.....	73
Figure 4.9 Potential dependency of C_{EDL} at (A): f-HOPG/PBS and (B): a-HOPG/PBS interfaces.....	74
Figure 4.10 Impedance spectra recorded at HRP modified a-HOPG surface in 10 mM PBS. (A): Substrate potential changing pattern according to which the impedance spectra were recorded. (B): Nyquist plot. (C): Bode plot.....	77
Figure 4.11 Equivalent circuit models for HRP modified a-HOPG surface (Sagara et al., 1990). For details see text.....	78
Figure 4.12 Potential dependency of C_{EDL} at HRP modified a-HOPG/PBS interface. C_{EDL} values calculated using model A in figure 4.11.....	80
Figure 4.13 Potential dependency of (A) HRP capacitance and (B) HRP capacitance variation rate.....	81
Figure 4.14 (A) Capacitance-potential curve for CHRP measured at HRP modified a-HOPG surface. (B) Typical capacitance-potential curve for a p-type MOS capacitor ('MOSFETs', 2006). (a) Low frequency, (b) Intermediate frequency, (c) High frequency, (d) High frequency and fast sweep rate (going into deep depletion).....	85
Figure 4.15 Metal-Oxide-Semiconductor (MOS) capacitor approximation. 3D plot of HRP structure was plotted with PyMOL(DeLano, 2002), with the accession code 1w4w from PDB(Carlsson et al., 2005).....	86
Figure 4.16 Mechanism of HRP-catalysed oxygen reduction reaction(Bergel & Lai, 2001).....	87
Figure 5.1 Series of SECPM images of HRP modified a-HOPG in 10 mM PBS (pH 7.4). Images were captured alphabetically as marked on the top left corner on each image at potentials as marked on the top right corner.....	92
Figure 5.2 Potential dependency of HRP molecular apparent height from images of HRP modified a-HOPG surface by SECPM in 10 mM PBS (pH 7.4). HRP 1, 2 and 3 corresponding to the number in figure 5.1 A.....	93
Figure 5.3 Software measurement of HRP molecular area and diameter. (A): the original image; (B): area and diameter measurement using the particle analysis	

function with the elongated part included; (C): measurement refining to exclude the elongated part.	94
Figure 5.4 Potential dependency of HRP molecular apparent area measured from images of HRP modified a-HOPG surface by SECPM in 10 mM PBS (pH 7.4). HRP 1, 2 and 3 corresponds to the number in figure 5.1 A, with elongated part included in (a1), (b1) and (c1), excluded in (a2), (b2) and (c2). The red curves show a qualitative potential dependency of HRP apparent area.	96
Figure 5.5 Potential dependency of HRP molecular apparent diameter measured from images of HRP modified a-HOPG surface by SECPM in 10 mM PBS (pH 7.4). HRP 1, 2 and 3 correspond to the number in figure 5.1 A, with elongated part included in (a1), (b1) and (c1), excluded in (a2), (b2) and (c2). The red curves show a qualitative potential dependency of HRP apparent diameter.	98
Figure 5.6 Potential dependency of HRP molecular apparent volume measured from images of HRP modified a-HOPG surface by SECPM in 10 mM PBS (pH 7.4). HRP 1, 2 and 3 correspond to the number in figure 5.1 A, with elongated part included in (a1), (b1) and (c1), excluded in (a2), (b2) and (c2). The red curves show a qualitative potential dependency of HRP apparent volume.	100
Figure 5.7 Illustration of potential dependent tip-substrate separation in SECPM. (A) A general illustration of charge distribution and tip-substrate separation (green dotted line) when $U = -300$ mV; (B) SECPM tip moving trace (black dotted line) when $U = -300$ mV; (B) SECPM tip moving trace (black dotted line) when U shifting to the positive side of -300 mV; (C) SECPM tip moving trace (black dotted line) when U shifting to the negative side of -300 mV.	104
Figure 5.8 Molecular structure of (A) arginine, (B) histidine, (C) lysine (with the proton binding atom marked red), (D) aspartic acid and (E) glutamic acid.	105
Figure 5.9 Series of EC-STM images of HRP modified a-HOPG in 10 mM PBS (pH 7.4). Images were captured subsequently according to the letter marked on the top left corner on each image at potentials as marked on the bottom right corner.	107
Figure 5.10 Magnified version of image A and E in figure 5.9.	108
Figure 5.11 Potential dependency of HRP apparent height measured from images of HRP modified a-HOPG surface by EC-STM in 10 mM PBS (pH 7.4). 1 and 2 correspond to the number marked in figure 5.9 A, representing the two particles observed.	109
Figure 5.12 Potential dependency of HRP apparent area measured from images of HRP modified a-HOPG surface by EC-STM in 10 mM PBS (pH 7.4). 1 and 2	

correspond to the number marked in figure 5.9 A, representing the two particles observed. The red lines show a qualitative potential dependency of HRP apparent area.

..... 110

Figure 5.13 Potential dependency of HRP apparent diameter measured from images of HRP modified a-HOPG surface by EC-STM in 10 mM PBS (pH 7.4). 1 and 2 correspond to the number marked in figure 5.9 A, representing the two particles observed. The red lines show a qualitative potential dependency of HRP apparent diameter..... 111

Figure 5.14 Potential dependency of HRP apparent volume calculated using data measured from images of HRP modified a-HOPG surface by EC-STM in 10 mM PBS (pH 7.4). 1 and 2 correspond to the number marked in figure 5.9 A, representing the two particles observed. The red lines show a qualitative potential dependency of HRP apparent volume. 112

Figure 5.15 Illustration of EC-STM imaging HRP modified HOPG..... 115

Figure 6.1 Potential variation pattern according to which the SECPM potential profiling spectra were recorded. 120

Figure 6.2 Potential dependency of the potential difference between the detected potentials at the beginning and end of each potential profiling curves recorded at f-HOPG and (A) 10 mM PBS, (B) 1mM PBS and (C) 0.1 mM PBS interfaces 121

Figure 6.3 Direct comparison within potential profiling curves recorded at f-HOPG and (A) 10 mM PBS, (B) 1mM PBS and (C) 0.1 mM PBS interfaces at -200 mV (down as marked in Figure 4.29). The colour colours stand for experiment 1 (red), 2 (yellow) and 3 (blue) performed one after another. 123

Figure 6.4 Comparison between SECPM potential profiling curves recorded at -400 mV down (red) and up (blue) (as in Figure 6.1) at HOPG and (A) 10 mM, (B) 1 mM and (C) 0.1 mM PBS interfaces at -400 mV..... 125

Figure 6.5 Comparison between SECPM potential profiling curves recorded at HOPG surface in 10 mM PBS at (A) -400 mV, (B) -200 mV and (C) 0 mV. Colours of spectra recorded at potential in down (red) and up (blue) frame in figure 6.1. 127

Figure 6.6 SECPM potential profiling of the EDL at highly oriented pyrolytic graphite (HOPG) and 10 mM (A, B and C), 1 mM (D, E and F) and 0.1 mM (G, H and I) PBS interfaces at potentials: (A, D and G) 0 mV, (B, E and H) -200 mV, and (C, F and I) -400 mV. 129

Figure 6.7 Theoretical and experimental potential distribution along the EDL. 130

Figure 6.8 SECPM potential profiling curve recorded at HOPG surface in 10 mM PBS (pH 7.4) at 150 mV vs SHE. 131

Figure 6.9 SECPM potential profiling curves of HOPG in 1 mM PBS (pH 7.4) with substrate potential as -400 mV. Red curve: experimentally acquired data, same as the curve in figure 6.6 F. Blue curve: regression fitting curve using equation 6.4, 6.5, 6.6 and 6.7. The parameters used for calculation were: inverse Debye length $\kappa = 6.62 \text{ nm}^{-1}$; inverse tunnelling length $\beta - 1 = 1.983 \text{ nm}^{-1}$; contact potential $E_c = 513.3 \text{ mV}$; tunnelling resistance $R_t = 8.18 \text{ M}\Omega$; Faradaic resistance $R_F = 18 \text{ G}\Omega$; and Amplifier input impedance $R_{\text{inp}} = 1 \text{ P}\Omega$ 134

List of Tables

Table 2.1 Comparison between EC-STM and SECPM.	37
Table 3.1 Chemicals used for experiments.	42
Table 3.2 Some examples of wire reference electrodes.	55
Table 4.1 Charge accumulation calculated from CV of HRP modified a-HOPG in 10 mM PBS (pH 7.4).	66
Table 4.2 Fitting results calculated from the impedance spectra for f-HOPG.	70
Table 4.3 Fitting results calculated from the impedance spectra for a-HOPG.	71
Table 4.4 Fitting results calculated from the impedance spectra for HRP modified a-HOPG, based on model A in figure 4.11.	79
Table 4.5 Fitting results calculated from the impedance spectra for HRP modified a-HOPG, based on Model B in figure 4.11.	82
Table 4.6 Fitting results calculated from the impedance spectra for HRP modified a-HOPG, based on Model B, with C_{HRP} substituted by Q in figure 4.11.	83
Table 5.1 Parameter setup for SECPM imaging HRP modified a-HOPG in 10 mM PBS.	90
Table 5.2 Parameter setup for SECPM imaging HRP modified a-HOPG in 10 mM PBS.	106
Table 6.1 Debye length of electrolytes and corresponding experimental parameters.	119

Chapter 1. Introduction

1.1 A Brief History of STM and AFM

In 1982, Rohrer and Binnig (Binnig & Rohrer, 1983; Scheel et al., 1982) developed scanning tunnelling microscopy (STM), which for the first-time enabled imaging at atomic level, and were awarded a Nobel Prize four years later. STM relies on the quantum tunnelling effect that at a small tip-sample separation distance, with a bias potential imposed between the tip and sample, electrons will tunnel through the tip-sample gap, resulting in a tunnelling current from the tip to the sample, or vice versa, depending on the applied potential polarity. Using tunnelling current as the feedback signal, STM maps the local density of states of the sample material and converts the signal into images reflecting the topological structures of the sample surface. In 1986, STM was improved to be functional in aqueous and electrochemical conditions (SONNENFELD & HANSMA, 1986; Sonnenfeld et al., 1987; Lustenberger et al., 1988), which expanded the application of this technique to electrochemical environments and interfaces.

Also in 1986, Binnig, Quate and Gerber (Binnig et al., 1986) introduced atomic force microscopy (AFM), which measured the force between the sample surface and the tip being attached to a cantilever that can vibrate due to the tip-sample interaction. It was furtherly developed into being functional in aqueous environment, allowing sample characterisation under electrochemical conditions. AFM provides mechanical and morphological information of the surface and has no requirement for sample conductivity unless specifically demanded.

Both STM and AFM belong to the category termed as scanning probe microscopy (SPM) because of the imaging work performed by STM and AFM is achieved by having the probe scanning above the surface. With the further development and proliferation use of SPM techniques, other than surface morphology imaging, the original purpose for which SPM techniques are invented, it comes to people's notice that depending on different imaging mechanisms, different SPM techniques could record different signals corresponding to different properties of the sample materials. SPM techniques are non-invasive and capable of operating under physiological conditions with resolution at

nanometre scale. These features make SPM techniques powerful tools for the investigation of biomolecules adsorbed at electrode-electrolyte interfaces.

1.2 Application of SPM Technology in the Investigation of Biomolecules

Biomolecules, especially redox enzymes due to their intrinsic functional properties (Jenner & Butt, 2018), has drawn great attention as them being inspirations for the design of new electrochemical systems of innovative applications and key components of biochemical electronic devices. A critical step for the development and fabrication of these bioelectronic devices is the immobilisation of enzyme molecules on electrode surfaces with activity, stability and specificity well retained (Mazurenko et al., 2017). Efforts have been made to evaluate the immobilisation, characterise the prepared bio-electrodes, and test the performance of the bioelectronic devices, from point of views of electrochemical, physical etc. With the help of electrochemical scanning probe microscopy (EC-SPM), the characterisation can be performed both qualitatively and quantitatively, at a relatively broad range or down to single molecular level.

One difficulty in enzyme electrochemistry is the quantification of enzyme coverage on the electrode. The coverage is not simply limited to the number of molecules immobilised on the surface, but also number of active molecules, of electroactive molecule etc, the data of which cannot be acquired by integral electrochemical measurements, such as cyclic voltammetry (CV). Using SPM techniques, the coverage could be approximated by counting the number of distinguished individual molecules per unit of area of the electrode surface. In 1998, AFM and STM were successfully used to monitor the level of protein catalase immobilised to Au electrode surface with modification by self-assembled monolayers through physical and chemical bonds (Patel et al., 1998). Other than single molecular coverage, protein molecules immobilised on electrode surface as aggregates or even monolayer could be monitored by SPM techniques. *Trametes versicolor* laccase was observed to be immobilised on Au electrode surface as monomers, aggregates, and compact monolayers through different immobilisation strategies by AFM in aqueous acetate buffer (Pankratov et al., 2014).

Other than surface coverage, the electrochemical activities, especially electron transfer reactions, could also be monitored by SPM techniques under electrochemical

conditions. Glucose oxidase (GOD) immobilised on anodized highly oriented pyrolytic graphite (HOPG) surface has been observed by electrochemical scanning tunnelling microscopy (EC-STM) to have direct electron transfer reactions with the electrode material at single molecular level (Wang et al., 2008b). The electron transfer reaction was visualized as apparent height decrease with an increase of overpotential with respect to the redox potential of GOD.

The development and application of SPM techniques contributes to the electrochemical investigation of many enzyme molecules, among which, horseradish peroxidase (HRP) is one of the popular ones (Krainer & Glieder, 2015). HRP is a heme-containing enzyme consists of 308 amino acid residues with a molecular weight of 40.9 kDa (Welinder et al., 1972). HRP has drawn great attention in electrochemical (Ruzgas et al., 1996), biochemical (Pandey et al., 2017) and biomedical (Shivakumar et al., 2017) applications due to its relatively low molecular weight, high stability, and low cost since it can be easily extracted from horseradish roots. Both native and genetically engineered HRP molecules have been extensively studied on their electrocatalytic activities on different substrate materials, such as gold (Ahirwal & Mitra, 2009), silver (Liu et al., 2008), platinum (Yuan et al., 2005), and especially carbon-based materials (Tertis et al., 2013).

AFM was also applied to study the HRP immobilisation on Au (111) surface with lipid bilayer modification (Fritzen-Garcia et al., 2013), providing surface coverage information for further HRP based biosensor investigations. Scanning electrochemical microscopy (SECM) is another powerful tool for HRP catalytic activity investigation with HRP molecules adsorbed on insulating substrate materials as micropatterns (Zhou et al., 2002; Roberts et al., 2011).

1.3 Mechanism of Immobilised Heme Proteins as Bioelectrocatalysis

HRP belongs to the heme protein family, in which heme group (Figure 1.1) can be bound to the proteins through covalent bond (Aicart-Ramos et al., 2012), weak hydrophobic (Liong et al., 2001) or hydrophilic interactions (Baker et al., 2003). The heme protein family consists of redox enzymes (Thomas L Poulos, 2014), electron transferases (Michel et al., 1998), and species for dioxygen transport and storage (KENDREW et al., 1960; PERUTZ et al., 1960), and these proteins play essential roles

in metabolic processes. Therefore, the heme proteins can be perfect candidates for bioelectronic devices when being immobilised on the surfaces of conductive materials, and in some cases, these protein-modified electrodes show better performance than the conventional electrodes in fields like yield efficiency and selective bioelectrocatalysis (Milton & Minteer, 2017; Wang et al., 2014; Masa & Schuhmann, 2016). Some commonly used heme proteins for bioelectrocatalysis are shown in figure 1.2.

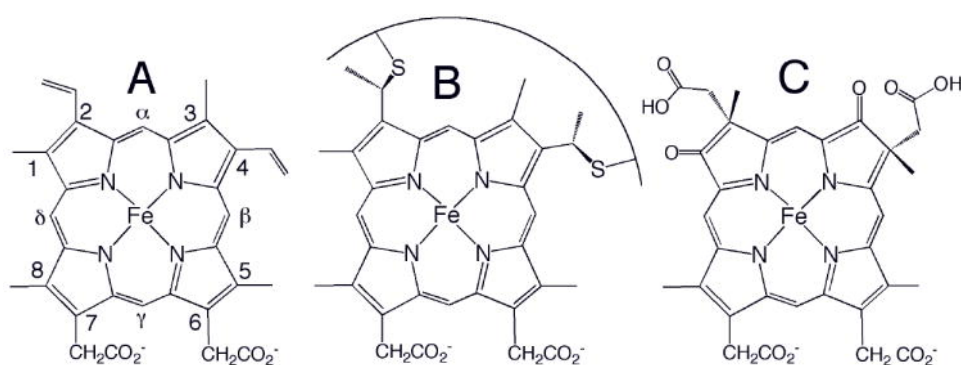


Figure 1.1 Chemical structures of heme groups: (A) heme *b*, (B) heme *c*, and (C) heme *d*₁. The Fisher numbering system for heme substituents is shown in (A). The curve in (B) represents a peptide segment; usually two residues separate the two Cys, and the His axial ligand follows the Cys attached to position 4. Heme *o* has a hydroxyfarnesyl group in place of vinyl 2 in (A), and heme *a* has a hydroxyfarnesyl group in place of vinyl 2 and a formyl group in place of methyl 8 (Bowman & Bren, 2008).

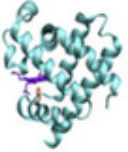

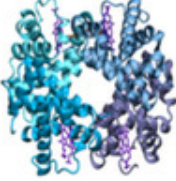

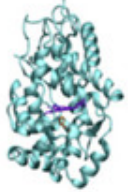

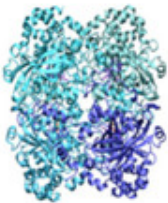

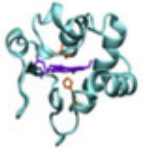
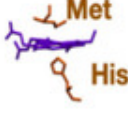
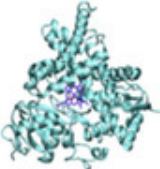



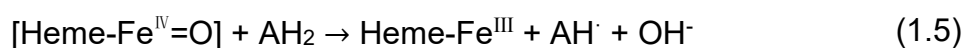
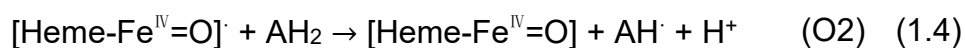
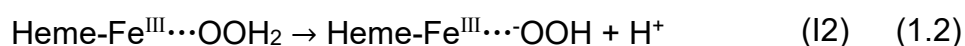
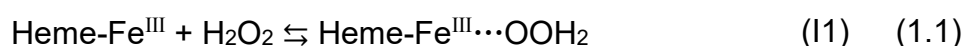
Protein	3D structure	Active site	Molecular Weight	Isoelectric Point	Projected area	Volume
Myoglobin (Human)		 His	17 KDa	7.3	15 nm ²	24 nm ³
Haemoglobin (Human)		 His	62 KDa	8.1	35 nm ²	72 nm ³
Peroxidase (Horseradish)		 His	34 KDa	6.3	20 nm ²	43 nm ³
Catalase (Bovine liver)		 Tyr	230 KDa	6.4	65 nm ²	312 nm ³
Cytochrome c (Yeast)		 Met His	12 KDa	9.5	10 nm ²	14 nm ³
Cyt P450 (Human aromatase)		 Cys	58 KDa	7.2	30 nm ²	65 nm ³
Microperoxidase (MP9 from bovine cyt c)		 His	1 KDa	8.0	1 nm ²	1 nm ³

Figure 1.2 Structural and physicochemical features of the heme proteins reviewed in the present work. The projected area at a surface and the molecular volume were estimated from the three-dimensional structure of a representative species of the family (Ranieri et al., 2019).

Despite the popularity of heme proteins in the field of bioelectrochemical devices drawing attention to study the mechanism of immobilised heme protein electrocatalytic activity (Heering et al., 1998; Huang et al., 2002; Limoges & Savéant, 2004; Wu et al., 2006; Léger & Bertrand, 2008; George & Lee, 2009; Sheng et al., 2010; Shi et al., 2015), the molecular details of bioelectrocatalytic process involving the heme proteins still remains partially understood. A mechanism for a bioelectrocatalytic reaction that HRP isoenzyme C participates has been proposed as the following reactions (Dunford, 2002; Jones & Dunford, 2005; Thomas L. Poulos, 2014):



where heme-Fe^{III} stands for the active centre of HRP molecule that reacts with hydrogen peroxide, resulting in the intermediate (I1) shown in reaction 1.1. The intermediate I1 will furtherly transform into another intermediate (I2) by releasing a proton as in reaction 1.2. In reaction 1.3, Fe^{III} in I2 is oxidised, giving the Fe^{IV}-containing radical O1, which can be reduced by an electron-rich substrate AH₂, generating Fe^{IV}-containing oxide O2 (Reaction 1.4). In the final step, another AH₂ gets involved to react with O2 to regenerate the heme group to its initial state (Reaction 1.5).

As described above, the redox centre of heme proteins, HRP included, is the heme group, which is usually deeply buried within the protein tertiary structure. To achieve direct electron transfer between heme proteins and the electrode on the surface of which the proteins are immobilised, the proteins should be in some specific orientations for enough active centre exposure and short distance between the active centre and the electrode surface. A successful immobilisation strategy should be able to have control of protein orientation and the packing density, and in the meantime avoid protein denaturation (de Groot et al., 2005; Brusova et al., 2006; Todorovic et al.,

2006). Sometimes mediators with suitable nano-structures are used as wiring material between the active centre and the electrode surface to enhance the electrochemical link between adsorbed proteins and the electrode materials (Armstrong & Wilson, 2000; Léger & Bertrand, 2008; Mano & de Poulpiquet, 2018).

However, in some cases, improper immobilisation technique could induce protein unfolding to a certain extent. The proteins losing of tertiary structures will lose their properties, in which cases, the redox reactions may be due to the denatured proteins or even the fully exposed free heme groups in the electrolyte (Todorovic et al., 2006; Brusova et al., 2006; de Groot et al., 2005).

1.4 SECPM in the Investigation of Electrochemical Properties of Immobilised HRP

In 1996, HRP molecules adsorbed on anodized HOPG surface were investigated by ex situ STM and had its individual dimension determined (Zhang et al., 1996). This result came ten years earlier than the one delivered by X-ray crystallographic analysis (Carlsson et al., 2005), the most commonly used technique to determine the protein tertiary structures. Additionally, through proper immobilisation technique, the redox activity could be well retained, enabling the adsorbed HRP molecules to directly catalyse the reduction of hydrogen peroxide.

As mentioned above, SPM techniques could provide topological and electrochemical information of electrochemically active enzyme molecules at single molecular level. However, for HRP, the SPM investigations have rarely been done to such extent. One of the limitations is the poor conductivity of HRP molecules. STM detects tunnelling current as feedback signal, which requires the target molecules to be conductive enough for the tunnelling current to flow through. Another issue is the difficulty to achieve direct electron transfer between HRP adsorbed on the electrode surface and the electrode materials with surface roughness being low enough for SPM techniques. The electrodes being reported to have direct electron transfer with HRP were all prepared with HRP being mixed with the materials used for electrode preparation, including sol-gel films (Di et al., 2005; Yu & Ju, 2002), polyelectrolyte films (Huang & Hu, 2003; Sun et al., 2007), carbon nanotubes (Zhao et al., 2002) and semiconductors (Zhang et al., 2004). Gold nanotriangles covered carbon ionic liquid electrode has been

reported to have direct electron transfer with HRP molecules adsorbed on the electrode surface (Niu et al., 2018). This direct electron transfer can be only achieved by loading a huge amount of HRP molecules on the surface (done by drop casting with 15 mg/mL HRP solution on the electrode surface). Due to the intermolecular interaction, HRP molecules will not exist on the electrode surface as single molecules.

The first limitation has been overcome by the development of scanning electrochemical potential microscopy (SECPM) (Baier & Stimming, 2009). SECPM maps the potential distribution along the electrochemical double layer (EDL) at the electrode-electrolyte interface. During SECPM scanning, there is no current flowing between the probe and the sample. This feature enables SECPM to have no requirement for sample conductivity and makes SECPM a perfect tool to investigate samples being vulnerable to high current, which is the case for a large number of biomolecules.

Another advantage of using SECPM is it shares the similar hardware with EC-STM, only with the current amplifier (for EC-STM) being substituted by a potentiometer (for SECPM). It is easy to switch between EC-STM and SECPM, making it possible to compare directly between images captured by the two techniques at the same location of the same sample surface.

SECPM Images with resolution at atomic level has been acquired on OH adsorbed Cu (111) surface in alkaline solution (Traunsteiner et al., 2015). Under physiological conditions, HRP molecules were imaged at single molecular level with resolution high enough to directly identify the active site (Baier & Stimming, 2009). From the direct comparison between the images of HRP modified anodized HOPG captured by both EC-STM and SECPM, one can see that SECPM could resolve HRP molecules to a higher extent than EC-STM.

Since it is difficult to have direct electron transfer between an electrode and the HRP molecules individually adsorbed on its surface, it is maybe the time to expand the focus from only the HRP active centre to the whole HRP molecule. In 1945, J. E. B. Randles proposed a circuit, which was known as Randles circuit, to describe the processes at an electrochemical interface (Randles, 1947). Randles circuit consists of a resistor representing the electrolyte resistance, a capacitor for the EDL and an impedance for a Faradaic reaction. The latter two components are connected in parallel, then in series with the electrolyte resistance. Randles circuit was then furtherly improved to describe the electrochemical process at the electrode-electrolyte interface with redox active

species adsorbed on the electrode surface (Sluyters-Rhbach & Sluyters, 1970; Senda & Delahay, 1961), by approximating the redox active adsorbent as a capacitor. To take the charge transfer process into consideration, an impedance of Faradaic reaction representing the electron transfer and a Warburg impedance for mass transfer were also included in these circuits. These circuits, also known as equivalent circuits, are commonly used for the interpretation of impedance spectra recorded by electrochemical impedance spectroscopy (EIS).

Inspired by the approximation of a redox active species to a combination of a capacitor and an impedance, and capacitance is directly related to the potential on the capacitor, the combination of EIS, which could monitor capacitance on a collective level, and SECPM, the technique that maps potential distribution in the EDL at nanometre/atomic scale, could make great contribution to the investigation of enzyme molecular capacitance.

1.5 SECPM for the Direct Probing of EDL Structure

SECPM would be underestimated if only being applied as an imaging technique. In 2004, Woo et al (Woo et al., 2004). published the first real space investigation of the potential distribution in the EDL at Au (111) and NaBF₄ interface using a homemade apparatus, which was improved and named as SECPM in 2007 (Hurth et al., 2007). The detailed structure of EDL has become the focus for decades since Hermann von Helmholtz published his theory that charged electrodes at electrode-electrolyte interface attract counterions and repelled co-ions that exist in the electrolyte phase in 1853 (Helmholtz, 1853). Theoretical efforts have been made to describe the EDL structure by Gouy (Gouy, 1910), Chapman (Chapman, 1913), Stern (Stern, 1924), Graham (Grahame, 1947) etc. Experimentally, AFM was applied to investigate the EDL with a probe modified with micrometre sized silica spheres (Hillier et al., 1996; Hu et al., 1999). The AFM investigation was limited by losing control of the silica modified probe, the charge on which could be only indirectly controlled by the ionic strength or pH of the electrolyte. The attempt to use scanning Kelvin probe microscopy to study the EDL succeeded only in gas phase (Nonnenmacher et al., 1991). Electric force microscopy (EFM) is another attempt, working in the way similar to AFM by measuring the electric force between the tip and sample (Viswanathan & Heaney, 1995). EFM

shares the same limitation with AFM that the attractive van der Waals force between probe and the sample interferes the detecting accuracy. Yoon et al. applied a potential gradient measurement using a nanometre potential probe to study the potential distribution in the EDL and demonstrated the potential in EDL as a function of probe-surface gap distance (Yoon et al., 2011). The measurement was performed with electrolyte with different concentrations to explore the influence of ionic strength on the potential distribution. But the influence of electrode potential was not shown.

1.6 Research Objectives

This work focused on the charge distribution at solid-liquid interface, including the charge distribution on the electrode surface and within the EDL. Potential dependent impedance spectra were recorded using EIS to monitor the capacitance of HRP molecules adsorbed on annealed HOPG surface in phosphate buffer solution (PBS). SECPM and EC-STM were used to perform potential dependent imaging of HRP molecules adsorbed on annealed HOPG surface at single molecular level. A metal oxide semiconductor (MOS) capacitor approximation has been proposed to describe the potential dependent electrochemical behaviour of HRP molecules at HOPG/PBS interface. Additionally, SECPM was applied to perform potential profiling in the EDL at HOPG/PBS interface, to explore the influence of electrode potential and ionic strength of electrolyte on the potential distribution in the EDL.

This thesis is structured into 7 chapters. Chapter 1 includes a discussion on the inspiration to this thesis, a brief summarisation of the SPM application in the field of imaging enzyme molecules at solid-liquid interface and probing the structure of EDL.

Chapter 2 gives a fundamental background of the EDL, EIS and SPM. In section 2.1, three models for EDL structure are briefly explained. Section 2.2 is about some principles about EIS, to help with the understanding of the relationship between electrochemical reactions and corresponding equivalent circuits. Section 2.3 and 2.4 give information on STM and SECPM, including the theoretical principles, hardware setups and operation modes.

Chapter 3 focuses on the experimental details, including the chemicals and instrumentation setup. Chapter 4 is on the investigation of the potential dependent

HRP capacitance behaviour. An MOS approximation is given as a description to understand the HRP capacitance behaviour. Based on the approximation proposed in chapter 4, SECPM and EC-STM were applied to monitor the potential drop within HRP molecular structure under electrochemical conditions and the results are given in detail in Chapter 5. Chapter 6 focuses on the potential profiling of EDL at HOPG/PBS interface using SECPM, including the reliability of SECPM as a potential profiling technique, the influence of the local electrical field and ionic strength on the potential distribution within the EDL, and a quantitative approach to explain the late response of potential decay at close tip-substrate separation. Summarisation and conclusion are given in Chapter 7, with an outlook for investigations to be performed in the future.

Chapter 2. Fundamentals

2.1 Electrochemical Double Layer

Electrochemical double layer (EDL) (Bard & Faulkner, 2001) exists at the boundary where two phases being separated by an interface that possesses properties differentiating it from the matters freely extended in either of the two phases. One commonly discussed case is the solid-liquid interface, where charge accumulates on the solid side at the interfaces and counter ions in the liquid side to balance. To study the distribution of charges and matters at the interfaces, several models have been proposed to describe the EDL structure and consequential potential arising.

2.1.1 Helmholtz Model

The first model to describe the EDL structure was proposed by Helmholtz (Helmholtz, 1853) in 1853 based on the concept that same amount of positive and negative charges being separated by the interface. In Helmholtz model, the positive and negative charges separated by the interface are assumed to be equivalent to two charged parallel plates forming a capacitor (Figure 2.1). Charge density of each plate (σ) could be expressed as the following equation:

$$\sigma = \frac{\epsilon_r \epsilon_0}{d} U \quad (2.1)$$

where ϵ_r is the dielectric constant, ϵ_0 is the free space permittivity, d is the distance between centres of positive and negative charges and U is the potential difference between the two virtual plates. The differential capacitance of the capacitor modelled by the Helmholtz approximation (C_H) can be calculated as:

$$\frac{\partial \sigma}{\partial U} = C_H = \frac{\epsilon_r \epsilon_0}{d} \quad (2.2)$$

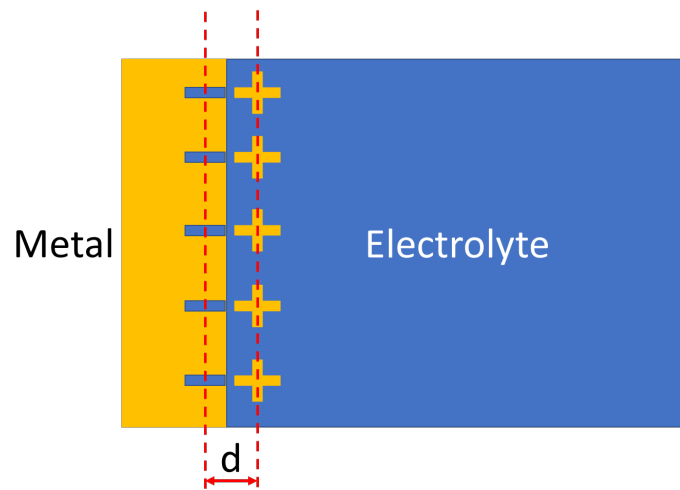


Figure 2.1 Helmholtz model for EDL at solid-liquid interface, where the metal electrode is negatively charged and the charged is balanced by counter positive ions placed at an increment of d away from the solid surface.

Helmholtz model is the simplest approximation to describe the EDL structure that explains a general electrochemical situation with two equations. However, for a certain system with explicit electrode material and electrolyte composition, C_H is a constant value, which is not in agreement with the experimental data. EDL capacitance is observed to be dependent on the applied potential and the concentration of the electrolyte. The opposite charges forming the EDL do not behave like rigid plates as hypothesized in Helmholtz model, which means there are other factors having influence on either ϵ or d , or both.

2.1.2 Gouy-Chapman Model

In early 1920s, Helmholtz model was improved by Gouy (Gouy, 1910) and Chapman (Chapman, 1913), respectively, through the introduction of a new concept: the diffuse layer (Figure 2.2).

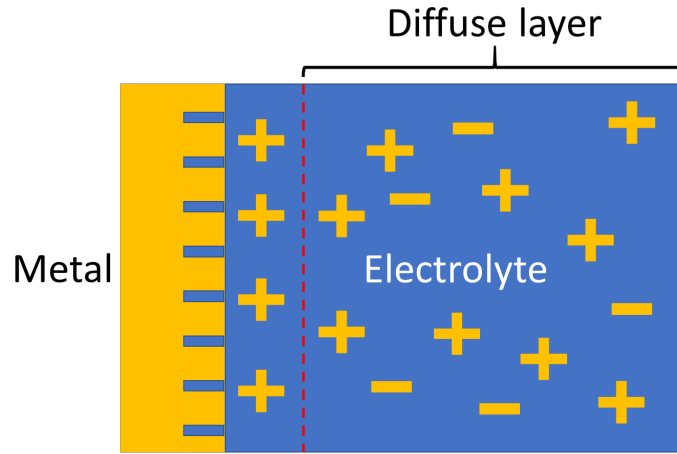


Figure 2.2 Illustration of Gouy-Chapman model for EDL.

In the electrode side of the interface, charge resides at the surface. But in the electrolyte side, due to the interaction between ions, these charged particles will diffuse away from the interface into the bulk solution, forming the diffuse layer. Gouy and Chapman proposed a statistical approach to describe the distribution of the charged particles in the diffuse layer by approximating the diffuse layer as a series of laminae being parallel mutually and to the electrode surface. Since the electrostatic potential is inversely proportional to the distance from the electrode surface, although the laminae are all in equilibrium with each other, ions existing in different laminae are not at the same energy due to the varying electrostatic field. In diffuse layer, the change in concentration of the charged particles follows a Boltzmann distribution:

$$n_i = n_i^0 \exp\left(\frac{-z_i e \varphi(x)}{k_B T}\right) \quad (2.3)$$

where n_i is the concentration of species i with ionic charge z_i and bulk concentration n_i^0 , e is the elementary charge, k_B is the Boltzmann constant, T is the temperature in Kelvin and $\varphi(x)$ is the electrostatic potential at distance x from the electrode surface.

Since the rigid layer of ions in Helmholtz model is replaced by laminae diffusing into the bulk solution, the volume charged density $\rho(x)$ rather than the surface charge density should be used for the further capacitance calculation. The volume charge density can be calculated by integrating equation 2.3 as

$$\rho(x) = \sum_i n_i^0 z_i e \cdot \exp\left(\frac{-z_i e \varphi(x)}{k_B T}\right) \quad (2.4)$$

Using the volume charge density, the coulombic interactions can be expressed by the Poisson equation as:

$$\frac{d^2\varphi(x)}{dx^2} = -\frac{\rho(x)}{\varepsilon\varepsilon_0} \quad (2.5)$$

Assuming the potential at infinite distance from the electrode surface in the bulk solution is zero and no potential change in that region, meaning $\varphi(x = \infty) = 0$ and $\frac{d\varphi}{dx} = 0$, then the combination of equation 2.4 and 2.5 gives Poisson-Boltzmann equation:

$$\left(\frac{d\varphi}{dx}\right)^2 = \frac{2k_B T}{\varepsilon_r \varepsilon_0} \sum_i n_i^0 \left[\exp\left(\frac{-z_i e \varphi(x)}{k_B T}\right) - 1 \right] \quad (2.6)$$

The diffuse layer thickness (κ), also known as Debye-Hückel length, could be calculated using the following equation:

$$\kappa = \left(\frac{2n^0 z^2 e^2}{\varepsilon_r \varepsilon_0 k_B T}\right)^{-1/2} \quad (2.7)$$

The Gouy-Chapman model describes the EDL as a rigid charged layer close to the interface and a diffuse layer next to the rigid layer, and the concentration of charged particles in the diffuse layer as a function of the distance from the surface. In this model, d (Figure 2.1) is not constant, and the influence of electrolyte concentration is taken into consideration. However, it is still not the perfect model for assuming the charged particles as point charge.

2.1.3 Gouy-Chapman-Stern Model

As mentioned above, if the charged particles are approximated as point charges, then when a large potential is applied, the point charges will be attracted infinitely close to the electrode surface, resulting in an infinitely large differential capacitance of the EDL.

Stern improved the Gouy-Chapman theory by considering the ions having finite size. These ions cannot approach to the electrode surface closer than a certain distance, which is usually taken as the radius of these ions (Figure 2.3).

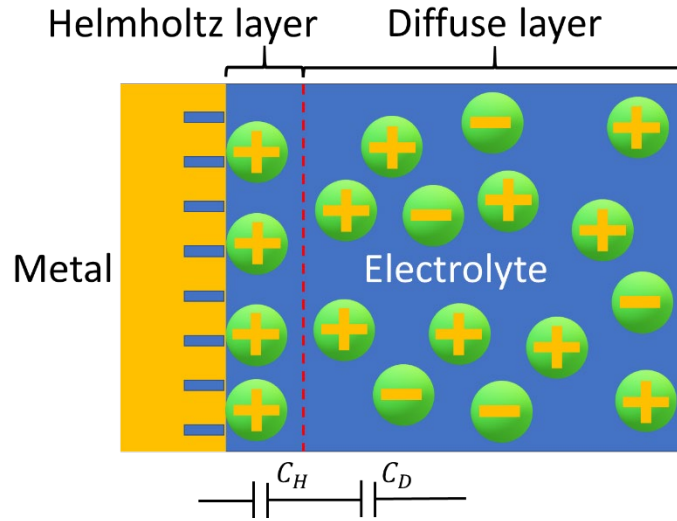


Figure 2.3 Illustration of Gouy-Chapman-Stern model for EDL structure. C_H is the Helmholtz layer capacitance and C_D is the diffuse layer capacitance.

In Gouy-Chapman-Stern model, EDL consists of two layers: the Helmholtz layer formed by ions with finite size compacted closely to the electrode surface, and the diffuse layer described by the Gouy-Chapman model. The combined double layer capacitance (C_{EDL}) is represented by C_H and C_D connected in series:

$$\frac{1}{C_{EDL}} = \frac{1}{C_H} + \frac{1}{C_D} \quad (2.8)$$

According to equation 2.8, C_{EDL} is always smaller than the smaller one between C_H and C_D . Under low potential, C_D contributes more to C_{EDL} , resulting in a V-shape capacitance potential curve. Under high potential, C_D will be too large to influence the EDL capacitance and C_{EDL} will be close to C_H .

More complicated cases, including the influence of solvated ions will be discussed in the following sections.

2.1.4 Specific Adsorption

As mentioned above, ions could be solvated (surrounded by solvent molecules or ions) and the closest approach distance of the solvated ions to the electrode surface will be larger than the ion radius. In the meantime, although the Gouy-Chapman-Stern model could approximate the EDL structure quite well, there are still aspects that can be

improved. For example, solvent polarization, ion-ion interactions and strong non-specific interactions between ions and the electrode surface are neglected. Electrolyte permittivity ϵ_r is still assumed to be independent of distance from electrode surface and potential.

In figure 2.3, positive ions are attracted closely to the negatively charged surface. However, anions could enter the double layer without the solvation shell and bond to the electrode surface chemically, and this phenomenon is termed as specific adsorption. These chemical interactions linking the ions and the electrode surface effect only within short range, giving smaller ion-surface distance comparing to the other charged particles in the double layer. The centre of these specifically adsorbed ions is termed as Inner Helmholtz Plane (IHP). Comparing to the specific adsorption, nonspecific adsorption is due to the long-range electrostatic interactions between the charged electrode surface and solvated counter ions in the electrolyte. The distance of the closest approach by non-specifically adsorbed ions defines the Outer Helmholtz Plane (OHP).

Figure 2.4 shows the illustration of the modified Gouy-Chapman-Stern model with Helmholtz plane being replaced by IHP and OHP proposed by Graham (Grahame, 1947). This is currently the well accepted EDL model that consists of three layers: IHP formed by specific adsorption of ions on electrode surface, OHP formed by non-specific long range electrostatic interactions between ions and electrodes and the diffuse layer.

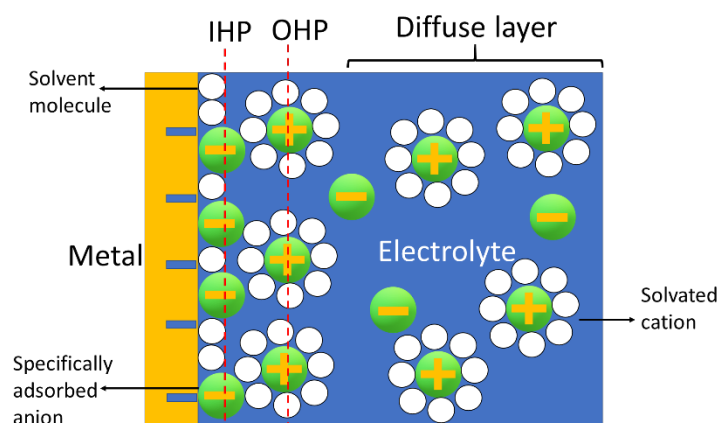


Figure 2.4 Illustration of Gouy-Chapman-Stern model modified by Graham with specific and non-specific ion-electrode interactions.

2.2 Electrochemical Impedance Spectroscopy

An electrochemical reaction and an electrical circuit share a feature that with an external applied input potential signal, an output current signal will be generated correspondingly. Due to the input-output behaviour, an electrical circuit approach could be applied to describe an electrochemical process. Electrochemical impedance spectroscopy (EIS) (Volkov & Prokhorov, 2003; von Hippel & Morgan, 1955; Kremer & Schonhals, 2003) is a technique to characterise the electrochemical process by measuring the output current signal generated by the applied perturbative input potential.

2.2.1 Concepts and Principles

In an electrical circuit, the ability to resist the current flow is termed as electrical resistance (R), which is determined by Ohm's law:

$$R = \frac{U}{I} \quad (2.9)$$

where U is the applied potential, and I is the current flowing through the circuit.

When Ohm's law is applied in the field of alternating current, the resistance will be replaced by a more general concept, impedance (Z), which can be expressed as

$$\dot{U} = \dot{I}Z \quad (2.10)$$

Unlike the resistance, impedance is frequency dependent and the voltage and current signal through an impedance will not be in phase with each other.

An electrochemical reaction could be considered as an impedance. The electrochemical impedance is usually measured by applying an AC potential to the electrochemical system and then measuring the output current signal. Assuming a small sinusoidal AC excitation potential (U_0) to an electrochemical cell, the response will be an AC current signal (I_0), which can be analysed as a Fourier series. The sinusoidal potential and current signal could be expressed using the following equations:

$$U_t = U_0 \sin(\omega t) \quad (2.11)$$

$$I_t = I_0 \sin(\omega t + \phi) \quad (2.12)$$

where U_t and I_t are potential and current at time t , respectively, ϕ is the current phase shifting, ω is the radial frequency and its relationship with the AC voltage signal frequency f is

$$\omega = 2\pi f \quad (2.13)$$

According to Ohm's law, the impedance Z_t at time t can be calculated as

$$Z_t = \frac{U_t}{I_t} = \frac{U_0 \sin(\omega t)}{I_0 \sin(\omega t + \phi)} = Z_0 \frac{\sin(\omega t)}{\sin(\omega t + \phi)} \quad (2.14)$$

From Equation 2.14, it could be seen that the impedance is represented in terms of the magnitude Z_0 and a phase shift ϕ , and they both are frequency dependent. The plot in which Z_0 and ϕ are plotted versus the signal frequency f is termed as Bode plot (Yarlagadda, 2010).

Using Euler's formula, the sinusoidal potential and current could also be expressed as

$$U_t = U_0 \exp(j\omega t) \quad (2.15)$$

$$I_t = I_0 \exp(j\omega t - \phi) \quad (2.16)$$

where j is the imaginary unit.

In this case, impedance Z_t will be expressed as a complex number

$$Z(\omega) = \frac{U}{I} = Z_0 \exp(j\phi) = Z_0 \cos\phi + Z_0 j \sin\phi \quad (2.17)$$

where $Z_0 \cos\phi$ and $Z_0 j \sin\phi$ are termed as the real part (Z_{Re}) and the imaginary part (Z_{Im}), respectively. Nyquist plot (Lee, 2003), the data presenting method other Bode plot, is graphed by plotting $-Z_{Im}$ (as Y-axis) versus Z_{Re} (as X-axis).

2.2.2 Classic Electrochemical Reaction Models and the Corresponding Equivalent Circuits

As discussed above, EIS is performed by considering electrochemical reactions analogous to electric circuits. For impedance spectra analysis, the measured electrochemical system is represented by an equivalent circuit with one or multiple components, such as resistor, capacitor, and inductor.

For an equivalent circuit consists of a single capacitor, the Nyquist plot will be a straight line overlapping the Y-axis, in another word, the real part Z_{Re} equals to zero (Figure 2.5).

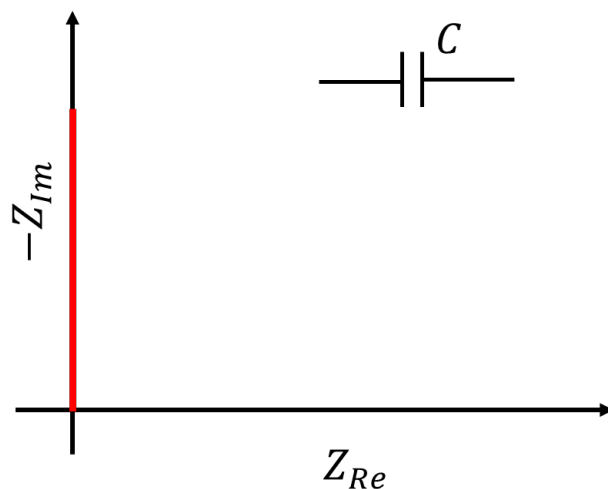


Figure 2.5 Nyquist plot for the equivalent circuit with a single capacitor.

By adding a resistor connected in series to the capacitor, Z_{Re} is assigned with a non-zero value, giving a straight line parallel to the Y-axis and intersect at R on X-axis (Figure 2.6).

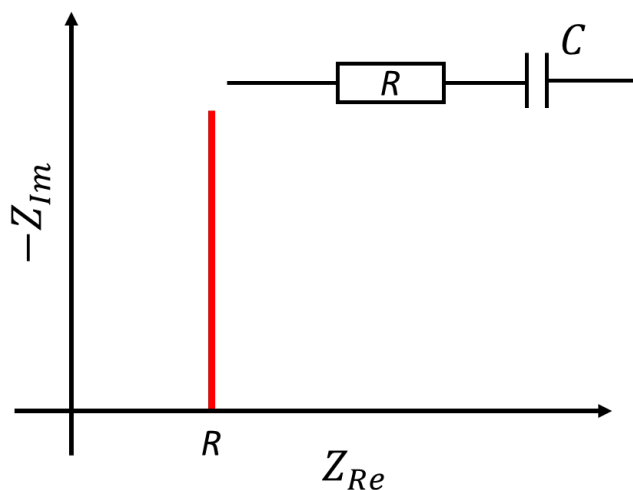


Figure 2.6 Nyquist plot for the equivalent circuit of a resistor and a capacitor connected in series.

The two equivalent circuits mentioned above are ideal cases that one rarely encounters in experimental work. A classic electrochemical system which is usually investigated by EIS is the EDL. The theoretical models to describe an EDL has been

discussed in section 2.1. A typical EDL at an electrode-electrolyte interface could be approximated by the equivalent circuit consists of three components: a capacitor (C_{EDL}) representing the double layer capacitance, a resistor (R_s) stands for the ability of electrolyte resisting current flow and an impedance (Z_f) representing the possible Faradaic process at the electrode-electrolyte interface (Figure 2.7). This equivalent circuit is also known as a simplified Randles cell (Randles, 1947).

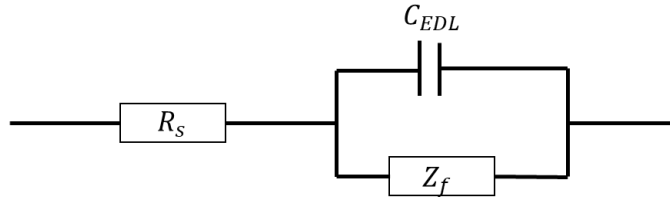


Figure 2.7 Diagram for a simplified Randles cell.

A Faradaic process is usually regarded as two processes: a charge transfer process such as a redox reaction, and a mass transfer process such as charged particle adsorption to or desorption from the electrode surface. The former could be approximated as a charge transfer resistance (R_{ct}) and the latter a Warburg impedance (Z_w). In the simplified Randles cell, the Faradaic impedance could be replaced by a charge transfer resistance and a Warburg impedance connected in series.

For a simplified Randles cell, the real and imaginary parts of the impedance could be expressed as the following equations:

$$Z_{Re} = R_s + \frac{R_{ct} + \sigma \omega^{-1/2}}{(C_{EDL} \sigma \omega^{1/2} + 1)^2 + \omega^2 C_{EDL}^2 (R_{ct} + \sigma \omega^{-1/2})^2} \quad (2.18)$$

$$Z_{Im} = \frac{\omega C_{EDL} (R_{ct} + \sigma \omega^{-1/2})^2 + \sigma \omega^{-1/2} (C_{EDL} \sigma \omega^{1/2} + 1)}{(C_{EDL} \sigma \omega^{1/2} + 1)^2 + \omega^2 C_{EDL}^2 (R_{ct} + \sigma \omega^{-1/2})^2} \quad (2.19)$$

where σ is a coefficient related to mass transfer.

According to equation 2.14, it can be seen that the impedance is frequency dependent. When the input signal frequency (ω) is close to zero (low frequency), the relationship between Z_{Re} and Z_{Im} could be simplified as

$$Z_{Im} = Z_{Re} - R_s - R_{ct} + 2\sigma^2 C_{EDL} \quad (2.20)$$

The graph of Z_{Im} versus Z_{Re} , according to equation 2.20, should be a straight line with the slope equals to one (Figure 2.8).

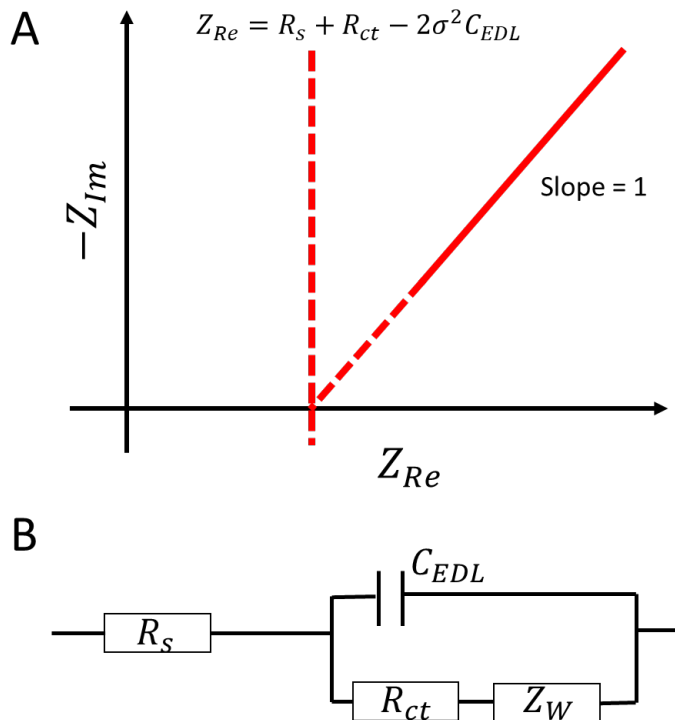


Figure 2.8 (A) Nyquist plot of a simplified Randles cell with input signal frequency close to zero; (B) The equivalent circuit represent the Randles cell corresponding to (A).

With a high input signal frequency, due to the short signal alternating period and the relatively low mass transfer kinetics, the Warburg impedance will become non-effective and the equivalent circuit could be approximated as shown in figure 2.9.

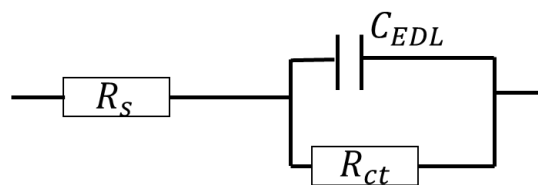


Figure 2.9 Equivalent circuit for a Randle cell under high frequency input signal.

In this case, the relationship between Z_{Re} and Z_{Im} could be expressed as

$$(Z_{Re} - R_s - \frac{R_{ct}}{2})^2 + Z_{Im}^2 = (\frac{R_{ct}}{2})^2 \quad (2.21)$$

The Nyquist plot based on Equation 2.21 is a semicircle centred at $R_s + \frac{R_{ct}}{2}$ on X-axis with radius as $\frac{R_{ct}}{2}$ (Figure 2.10).

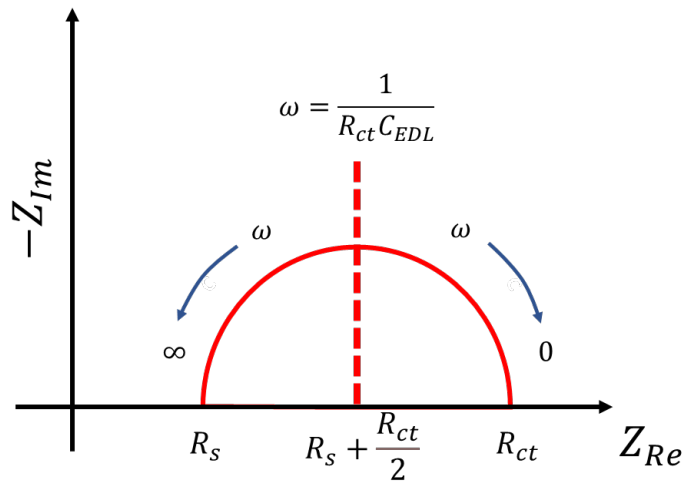


Figure 2.10 Nyquist plot for the equivalent circuit in figure 2.9.(Bard & Faulkner, 2000)

Based on the discussion of the two cases with extreme conditions, a normal Nyquist plot measured at the electrode-electrolyte interface by EIS could be analysed as two regions: the high frequency region dominated by the charge transfer process and the low frequency region dominated by the mass transfer process (Figure 2.11).

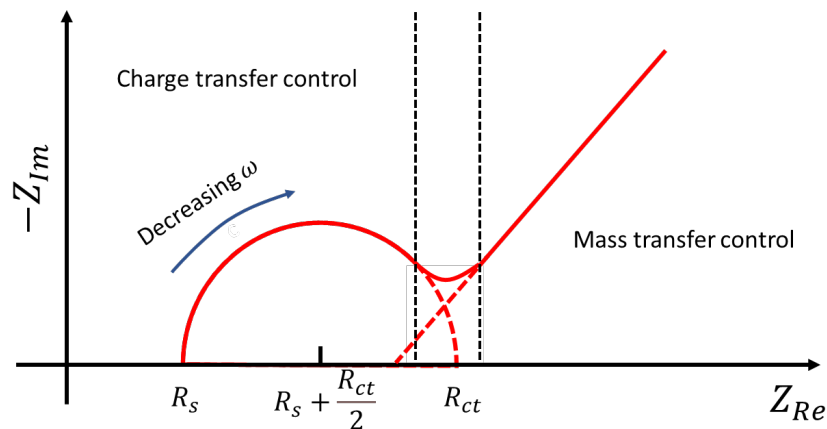


Figure 2.11 A general illustration of a Nyquist plot for a simplified Randles cell.(Bard & Faulkner, 2000)

For EIS analysis, Nyquist plot is more often used since it provides the convenience to analysis the electrochemical reaction mechanism through equivalent circuits. However, one important factor being left out in the Nyquist plot is the phase difference ϕ between

the input AC voltage and the output current (Equation 2.12). To solve this problem, a Bode plot can be used to represent the impedance spectrum to show the phase shift and magnitude change in the applied frequency range (Figure 2.12).

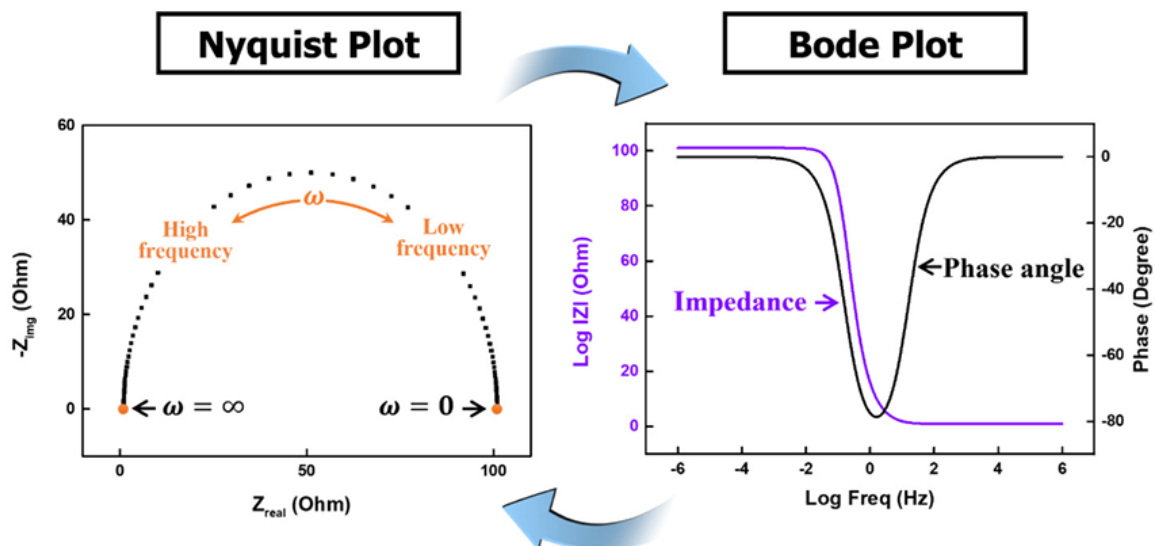


Figure 2.12 Impedance spectrum represented by Nyquist plot and Bode plot.(Choi et al., 2020)

Usually, the experimentally acquired EIS plots are more complicated than the cases mentioned above and there could be more than one equivalent circuit that fits the experimental data perfectly. So practically speaking, the equivalent circuits used for EIS data analysis should be chosen carefully based on specific conditions.

2.2.3 EIS Application on Lithium-ion Batteries: Determining the State of Health

In 2019, John B. Goodenough, M. Stanley Whittingham, and Akira Yoshino won the Nobel Prize in chemistry for their contribution in the development of lithium-ion batteries. Here a simple application of using EIS to evaluate the state of health (SOH) of a lithium-ion battery is presented for the better understanding of the EIS theories mentioned above.

SOH is a figure of merit about the condition of a battery in comparison to the theoretical perfect conditions. 100% SOH indicates the battery being in the ideal condition, and it will decrease as the battery being used, leading to battery aging and performance degradation. Battery aging could be caused by several reasons, such as corrosion of current collector, electrolyte depletion etc. To determine or even estimate the SOH of a lithium battery in a quantitative method, EIS has been applied based on the equivalent circuit in figure 2.13.

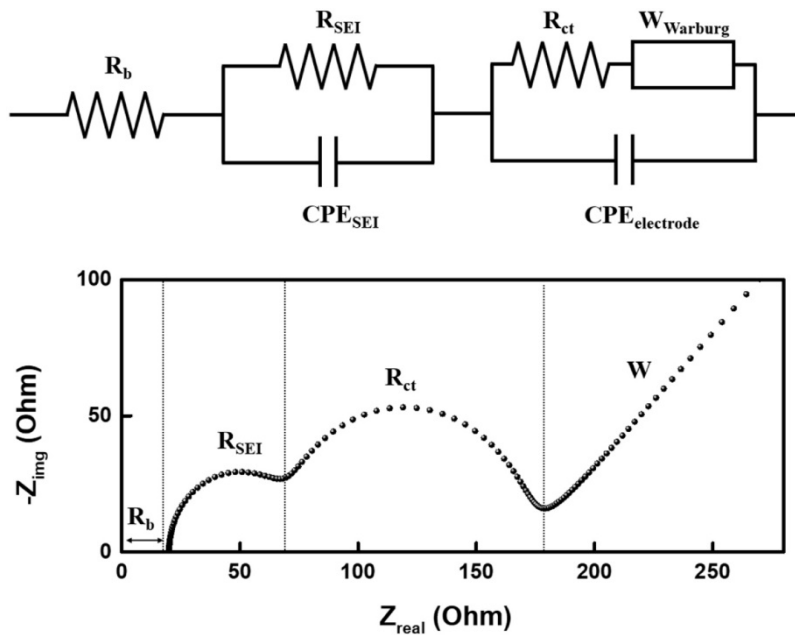


Figure 2.13 A simplified equivalent circuit for a lithium-ion battery half-cell system and the corresponding Nyquist plot. R_b is the bulk resistance of the cell; R_{SEI} and CPE_{SEI} stand for the resistance and capacitance (constant phase element) of the interfacial layer, respectively; R_{ct} and $CPE_{electrode}$ are charge-transfer resistance and double layer capacitance; $W_{Warburg}$ represents the diffusional effects of lithium ion on the host material. (Choi et al., 2020)

Investigations have been performed to monitor the internal resistance (also known as the bulk resistance) of a lithium-ion battery with changing SOH (Figure 2.14 A), state of charge (SOC) (Figure 2.14 B) and temperature (Figure 2.14 C) (Westerhoff et al., 2016). As can be seen from figure 2.14, EIS spectra of the same battery show dependency on all the three factors mentioned above.

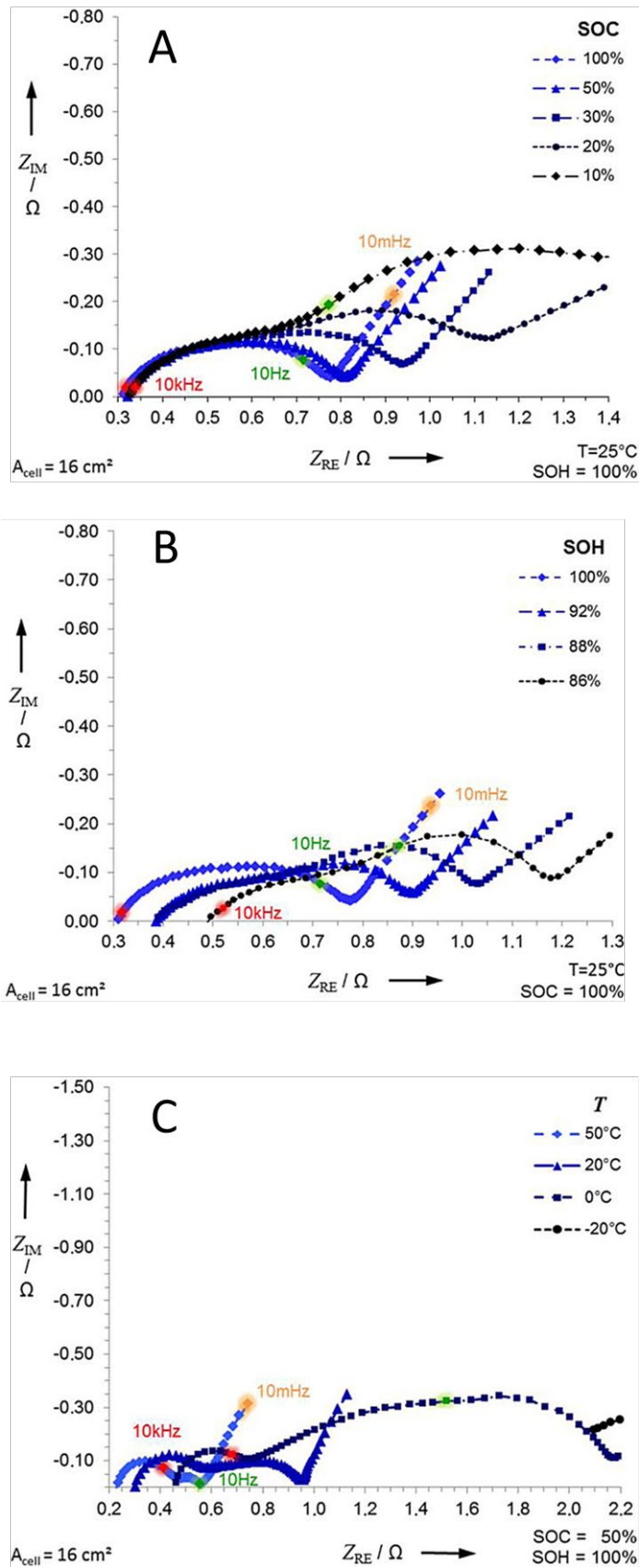


Figure 2.14 Nyquist plot for lithium-ion battery with decreasing (A) SOC; (B) SOH; (C) temperature. (Westerhoff et al., 2016)

Figure 2.15 give more detailed analysis of the impedance spectra. In figure 2.15 a, three key points of frequency are marked on the Nyquist plot. The very beginning of the Nyquist plot, the frequency at which point is noted as $f_{ZIM,0}$, is directly determined by the internal resistance (R_b in figure 2.13) of the system (R_s in figure 2.11). At the maximum of the semicircle of the spectrum, $f_{ZIM,max}$ is marked to represent the charge transfer process. And the last noted frequency, $f_{ZIM,min}$ indicates the frequency at which the diffusion of lithium ions starts.

From figure 2.15 b, c and d, with the variation of SOC (Figure 2.15b), SOH (Figure 2.15 c) and temperature (Figure 2.15 d), there are obvious shifts of the process frequencies for $f_{ZIM,min}$ and $f_{ZIM,max}$, that with decreasing SOC, SOH and temperature, both the frequencies shift to the lower region in the frequency range. These shifts in process frequencies clearly show that the charge transfer process and ion diffusion process are dependent on SOC, SOH and temperature.

On the contrary, $f_{ZIM,0}$ is nearly independent on the SOC, and also independent on temperature unless the temperature is lower than 0°C . Only SOH has strong influence on $f_{ZIM,0}$ that with the decreasing SOH, $f_{ZIM,0}$ shifts to the high region in the frequency range, meaning that R_b is in inversely proportional to the SOH. The dependence on SOC and independence on SOC and temperature make R_b a valuable indicator to examine and even estimate the battery aging conditions.

One point worth noticing is the equivalent circuit in figure 2.13 is a quite simplified version that only works for the most fundamental lithium-ion battery half-cell. For every single electrochemical system, there should be a customised equivalent circuit to fit it to the largest extent. A more detailed equivalent circuit customisation procedure is given in section 4.3.2.

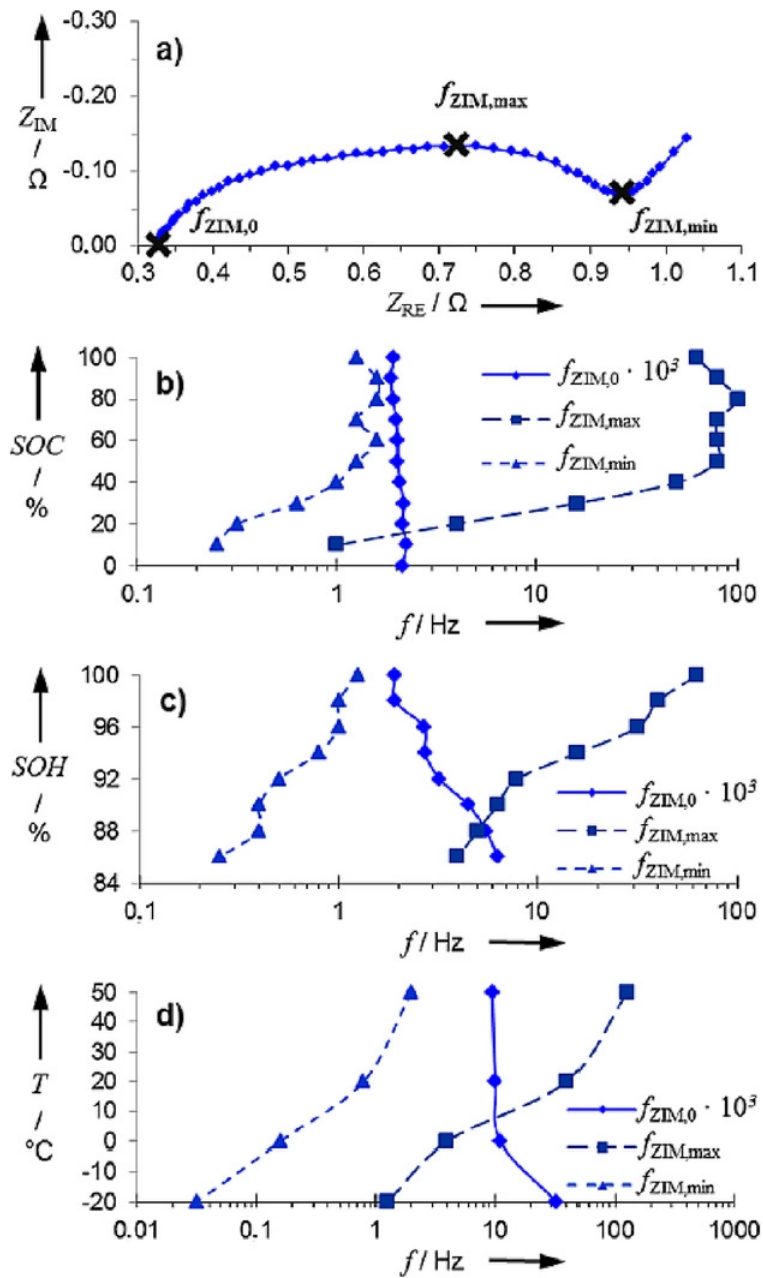


Figure 2.15 Shifts in the process frequencies depending on various factors of an impedance spectrum: a) impedance spectra, b) state of charge, c) state of health, d) temperature. (Westerhoff et al., 2016)

2.3 Scanning Tunnelling Microscopy

The scanning probe microscopy (SPM) technique dated back to 1982 when Binnig et al. introduced the scanning tunnelling microscopy (STM) technique to investigate CaIrSn_4 and Au surfaces on atomic scale in vacuum (Binnig et al., 1982). In 1987, Sonnenfeld et al. demonstrated the application of STM in aqueous conditions (Sonnenfeld et al., 1987). Later in 1988, Lustenberger et al. managed to perform electrolytic STM imaging under potentiostatic control with a four-electrode configuration (Lustenberger et al., 1988). Based on the theoretical foundation of STM, other SPM techniques were developed to meet the requirements of more complicated experimental conditions. Some were developed to expand the application of SPM techniques to study surfaces with various properties, like atomic force microscopy (AFM), which was also introduced by Binnig et al. (Scheel et al., 1982) to investigate insulator surfaces. Some were developed to study the solid-liquid interfaces on different perspectives, like scanning electrochemical potential microscopy (SECPM), a relatively new SPM technique named by Allen J. Bard et al. in 2007 (Hurth et al., 2007), with the capability to study the potential distribution of the electrochemical double layer (EDL) at solid-liquid interfaces. Both the STM and SECPM techniques will be briefly introduced in the following section.

2.3.1 Quantum Tunnelling Effect

The development of the STM technique is based the fact that between a metal tip and conducting substrate surface separated by a short distance (usually nanometre scale or smaller) in vacuum, electrons could penetrate the energy barrier created by the tip-substrate separation and tunnel from the tip to the substrate, or vice versa, even if their kinetic energy is lower than that of the barrier. This phenomenon is termed as quantum tunnelling effect and can be briefly explained by the overlapping of the wave functions of the tip and the substrate atoms.

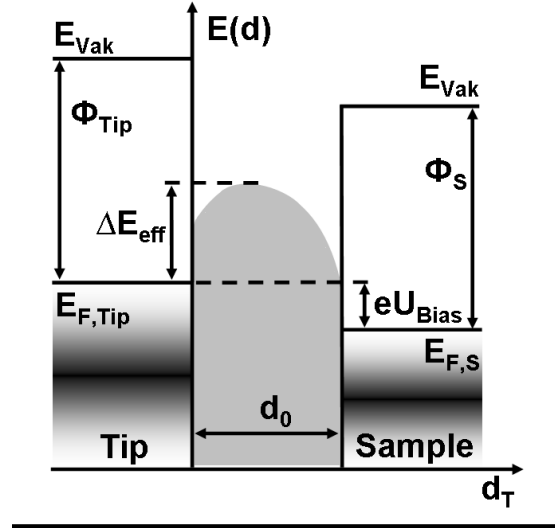


Figure 2.16 Diagram of the energy levels in an STM setup. (Baier, 2010)

In figure 2.16, the tip and the sample surface are separated by a distance d_0 with a potential U_{Bias} applied in between. E_{Vak} stands for the energy level of vacuum. The energy difference between the Fermi level of the tip ($E_{F,Tip}$) and the sample ($E_{F,S}$) is compensated by the energy introduced by the applied bias (eU_{Bias}). As mentioned earlier, due to the overlapping of the wavefunction of the tip (Φ_{Tip}) and that of the sample (Φ_S), the energy barrier between the tip and the sample surface (ΔE_{eff}) could be overcome and resulting in the electrons tunnelling from the tip to the sample. The tunnelling current (I_t) is dependent on the applied bias voltage (U_{Bias}) and the energy barrier due to the tip-sample separation (d_0 and ΔE_{eff}), and their relationship can be expressed by the well-known equation (Scheel et al., 1982):

$$I_t \propto U_{bias} \exp [-A\sqrt{\Delta E_{eff}}d_0] \quad (2.22)$$

where A is a constant and its value in vacuum is $10.12 \text{ eV}^{-1/2} \text{ nm}^{-1}$.

From equation 2.22, it can be seen that the tunnelling current is exponentially proportional to the tip-sample separation. This feature guarantees the STM technique with high sensitivity since a slight change in tip-sample separation distance will lead to a relatively large variation in the tunnelling current. Detailed operation mechanism of STM technique will be explained in the following sections.

2.3.2 STM Setup

The STM consists of a sharp metallic tip, a conductive/semiconductive sample (flat and clean) and a piezoelectric scanner attached to either the tip or the sample controlling relative position between the tip and sample in three dimensions with sub nanometre precision (Figure 2.13). During the STM scanning procedure, a bias voltage is applied to encourage the current flowing between the tip and the sample. The current flowing direction is depending on the polarity of the applied bias voltage. In figure 2.13, the piezoelectric scanner is connected to the tip, functioning as both the controller of tip movement and the collector of feedback signal, which is the tunnelling current.

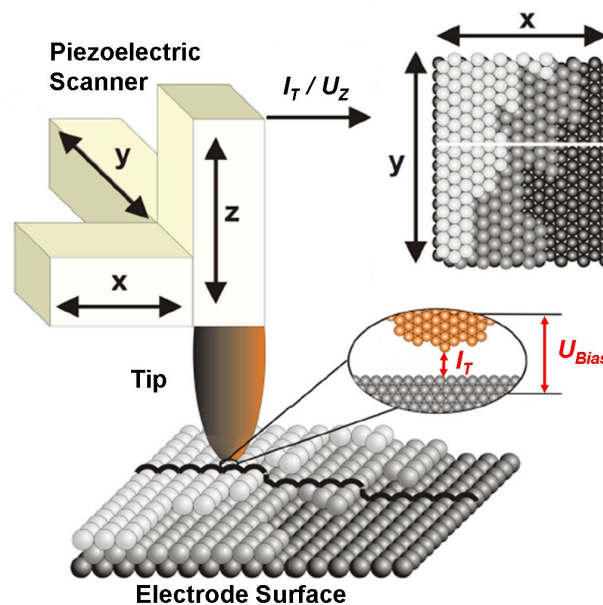


Figure 2.17 Scanning tunnelling microscopy setup.(Hugelmann, 2004)

2.3.3 STM Operation Modes

The tip-sample relative position is controlled by the piezoelectric scanner according to the feedback tunnelling current signal. Using equation 2.22, the feedback tunnelling current could be converted into tip-sample separation distance and then reflect in the captured images as the surface topological structure. Since tunnelling current and the tip-sample separation distance are the two major variables in equation 2.22, STM could be operated in two modes by keeping either of these two as constant. For the sake of

simplicity, in the following sections, the piezoelectric will be described as the controller of tip movement as shown in figure 2.17.

In constant current mode (Figure 2.18 A), I_t is held as a constant value (termed as current setpoint) according to which the tip-sample separation distance is constantly adjusted. While the STM tip scanning line by line in lateral directions, in the vertical direction, tip is controlled by the piezoelectric scanner, approaching to or retracting away from the surface when the detected tunnelling current is smaller or larger than the pre-set current setpoint value accordingly. Since STM detects the local density of states (LDOS), so not only the change of sample surface geometry, but also the change of LDOS, such as atomic substitution within the surface layer, will result in the tip-sample separation adjustment.

Since the tip-sample separation is constantly adjusted, the possibility of tip crashing on the sample surface could be minimised, especially in the cases with high sample surface roughness or a large lateral dimension scanning being required. The limitations in both lateral and vertical directions is depending on the properties of the scanners, and larger scanning range is usually achieved with the sacrifice of imaging resolution.

In constant height mode (Figure 2.18 B), the STM tip scans above the sample surface without any piezoelectric adjusting on the vertical direction. This feature enables fast scanning procedure due to no time being spent on the feedback loop control of the tunnelling current. However, without tip adjusting on the vertical direction, there is increasing risk of tip crushing on the sample surface during scanning. So constant height mode is usually applied when the sample surface is atomically flat and scan range is limited to a small dimension.

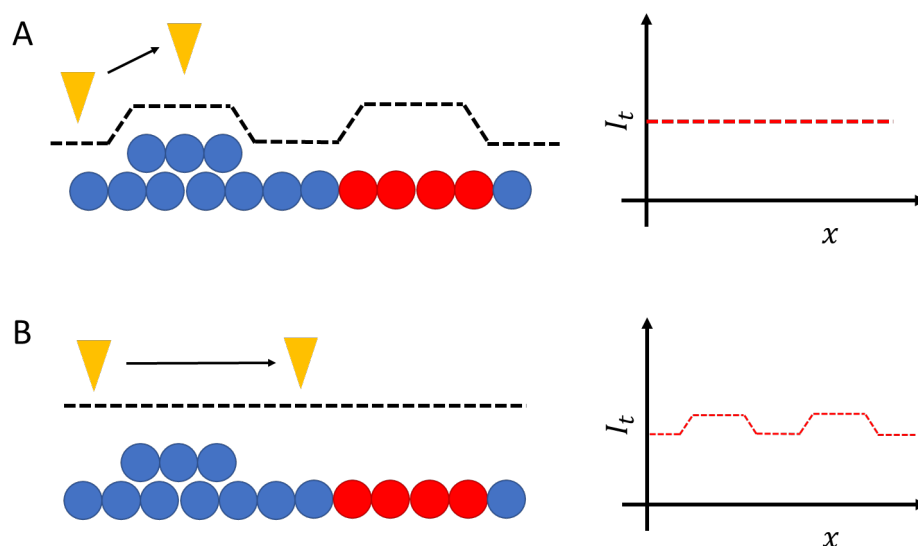


Figure 2.18 Operation of STM technique. (A) Constant current mode; (B) Constant height mode. Both modes with scheme of detected tunnelling current. The red part represents atoms with LDOS different from the blue part.

2.3.4 Electrochemical Scanning Tunnelling Microscopy

STM has been proved to be capable of operating in ultra-high vacuum (Müller et al., 2005), ambient conditions (Magonov, 1993), and liquid/electrolyte conditions (Lustenberger et al., 1988). Electrochemical scanning tunnelling microscopy (EC-STM) enables real space imaging of both the electronic properties and topological structures of electrode surfaces under in situ conditions with atomic resolution. This could be achieved by the introduction of a dual tri-electrode configuration in the electrochemical cell controlled by a bipotentiostat (Figure 2.19).

In figure 2.19, both the tip and the sample are regarded as working electrode (WE), the potential of which is controlled by the bipotentiostat with reference to a reference electrode (RE) to maintain a bias voltage. A counter electrode (CE) is applied as a part of the electrical circuit. Due to the limited space in the electrochemical cell for EC-STM, both the CE and RE are prepared from metal wires. Tips used in EC-STM measurement should be insulated, with only the apex exposed in the ideal case, to minimise the influence of Faradaic current at the tip on the accurate detection of tunnelling current. Using the bipotentiostat, potentials of the tip and the sample could be controlled, enabling the potential dependent imaging of the sample surface.

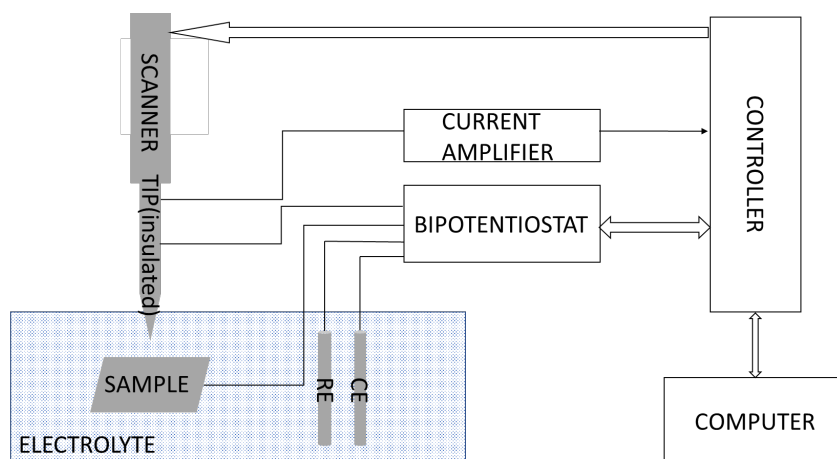


Figure 2.19 Schematic drawing of an electrochemical scanning tunnelling microscope setup.

2.4 Scanning Electrochemical Potential Microscopy

EC-STM has been proved to be capable of imaging sample surface at atomic level. However, using tunnelling current as feedback signal limits its application on only samples with good conductivity. Other scanning probe microscopy (SPM) techniques, such as atomic force microscopy (AFM), have been developed to expand the application of SPM on samples with relatively poor or zero conductivity. Scanning electrochemical potential microscopy (SECPM) has been developed since 2004 and already exhibits capability of imaging Cu (111) surface at atomic level (Traunsteiner et al., 2015) and biomolecules with poor conductivity at single molecular level. SECPM shares the similar hardware with EC-STM, making it easy and convenient to switch between these two techniques without interfering the setup. Direct comparison between images captured by EC-STM and SECPM at the same location has been made. The reported results suggest that SECPM could image biomolecules that being invisible to EC-STM and resolve the molecules could be imaged by EC-STM at a higher extent (Baier & Stimming, 2009).

2.4.1 SECPM Setup and Principles

SECPM shares the similar hardware setup with EC-STM, except the current amplifier for I_t detected is substituted by a potential amplifier (Figure 2.20). Usually both the current amplifier and the potentiometer are embedded within the hardware system, switching between these two techniques could be easily done using the controlling software, and this feature enables direct comparison of images of the same area captured by these two techniques.

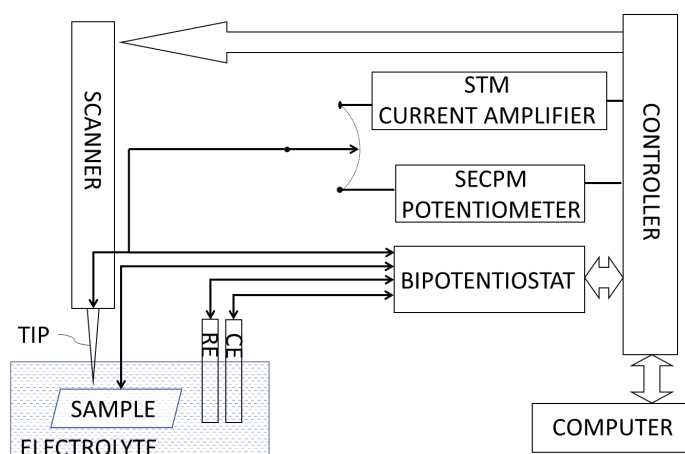


Figure 2.20 Schematic drawing of an SPM setup with both electrochemical scanning tunnelling microscopy and scanning electrochemical potential microscopy integrated.

Unlike EC-STM, SECPM detects the potential distribution within the EDL at the solid-liquid interface and records the potential difference between the tip and the sample as the feedback signal. Limited by the instrumental setup, the potential difference (ΔU) is always calculated as

$$\Delta U = |U_{tip} - U_{sample}| \quad (2.23)$$

where U_{tip} is the potential applied between the tip and RE, and U_{sample} is the potential between the sample and RE.

As can be seen from equation 2.23, a small ΔU leads to closer tip-sample distance and then furtherly higher imaging resolution. Theoretically, ΔU could be infinitely small, as long as still being positive, to achieve maximum imaging resolution. But practically, ΔU is suggested to not be smaller 5 mV to avoid tip crashing into the sample surface.

Since SECPM detects the potential distribution instead of tunnelling current, there is no requirement for sample conductivity. Without the current flowing through the sample surface, potential damage caused by the possibly high tunnelling current to samples with fragile structure could be minimised. These features make SECPM an ideal technique to investigate biomolecules, such as enzymes, DNA, RNA or even cells under physiological conditions.

2.4.2 SECPM Operation Modes

SECPM operation is based on the relationship between ΔU and the tip-sample separation distance. Like EC-STM, SECPM also operates in two modes, with each of the variables held constant, respectively.

In constant potential mode (Corbella et al., 2005), the tip-sample separation distance is constantly adjusted by the piezoelectric scanner to maintain ΔU constant as a pre-set value known as potential setpoint. As discussed in section 2.4.1, smaller potential setpoint leads to closer tip-sample separation distance, resulting in better imaging resolution and higher risk of tip crushing on the sample surface. Experimentally, the potential setpoint is suggested to be set between 5 mV and 20 mV as a compromise between imaging resolution and the tip sustainability.

In constant height mode, imaging procedure will be performed with no piezoelectric movement in vertical direction just like the constant height mode for EC-STM. Due to the similarity between EC-STM and SECPM, their corresponding operation modes share the same advantages and disadvantages.

A brief comparison between EC-STM and SECPM has been made and listed in Table 2.1.

	(EC-)STM	SECPM
Setup	Similar hardware setup	
Resolution	Sub-nanometre Spatial Resolution	
Image	Local Density of States	Potential Distribution
Feedback signal	Current	Potential
Sample electroconductivity	Yes	Not necessary
Damage to the sample	Possible	No
Probe insulation	Yes	No
In vacuum/Air	Yes	No
In liquid (electrochemical conditions)	Yes	Yes

Table 2.1 Comparison between EC-STM and SECPM.

2.4.3 SECPM Potential Profiling

In 2004, Woo et al. reported a technique, which was named as SECPM later in 2007, as a tool to conduct real-space probing of the EDL at Au(111)/NaBF₄ (1.0 mM) interface by approaching a nanoscale gold disk tip perpendicular to the Au(111) surface (Woo et al., 2004). Local potential at the tip location was measured and recorded as a function of the tip-sample distance. The potential profiling was performed within 30nm distance from the sample surface into the electrolyte and potential-distance curves were recorded with sample potential varying between -0.2 V and 0.4 V vs Au (gold wire as RE directly inserted into the 1.0 mM NaBF₄ solution). Since the homemade instrument they used is the first SECPM prototype in the world, there is no such a parameter as potential point that can limit the minimum tip-sample separation distance. In this experiment, the curve recording will not end until the tip being in direct mechanical contact with the sample surface. The potential profiling curves are shown in figure 2.21, from which one can observe the potential distribution within EDL being dependent on the potential applied on WE.

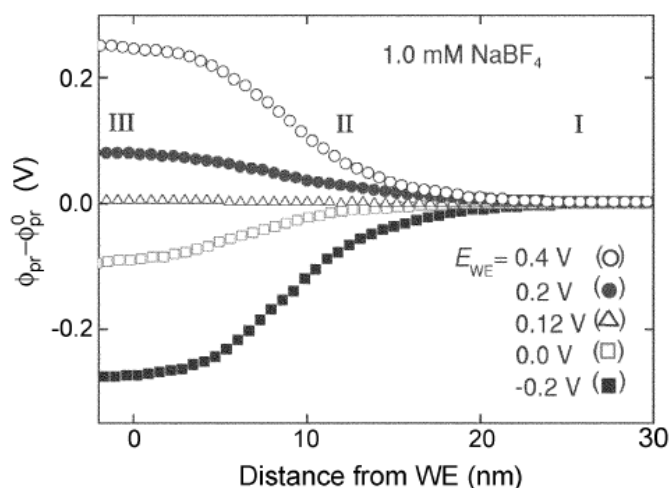


Figure 2.21 Potential measured at the probe ϕ_{pr} as it approaches the Au(111) surface; where ϕ_{pr}^0 is the OCP of the tip far away from the electrode surface. (Woo et al., 2004)

In 2007, Hurth et al. performed similar potential profiling experiments using an improved SECPM instrument at Pt/KCl interface with well fabricated Pt-Ir probes (Hurth et al., 2007). In this experiment, investigations have been done on the influence of electrode potential and electrolyte concentration on the local potential distribution in the EDL. Reproducibility of SECPM potential profiling was also studied. To study the potential dependency of EDL potential distribution, potential-distance curves were recorded with WE potential varied between 0.2 V and 0.4 V vs a platinum polypyrrol (PtPPy) reference electrode (Ghilane et al., 2006) at Pt/KCl (10 μ M) interface over a distance of 60 nm (Figure 2.22 a). Potential decay was observed within 0 nm and 30 nm away from the surface. But no obvious potential dependency could be observed from the potential-distance curves, and this is in conflict with the prediction based on the Gouy-Chapman-Stern model. Figure 2.22 b shows potential profiling curves recorded in KCl electrolytes with concentration varying between 10 μ M and 1 mM at +400 mV vs PtPPy. Comparing the curves recorded in 10 μ M and 100 μ M KCl, a change in the potential decay length from 60 nm (10 μ M KCl, Debye length 96 nm) to approximately 30 nm (100 μ M KCl, Debye length 30 nm) was observed. This result is qualitatively in agreement with the theoretical prediction of Gouy-Chapman-Stern model. But between the potential-distance curves recorded in 100 μ M and 1 mM KCl (Debye length 9.6 nm) electrolytes, no significant difference in potential decay length could be observed. An explanation was proposed that the size of the apex protruding

out from the insulation exceeding the expected double layer size, that the EDL in electrolyte with higher concentration could not be resolved.

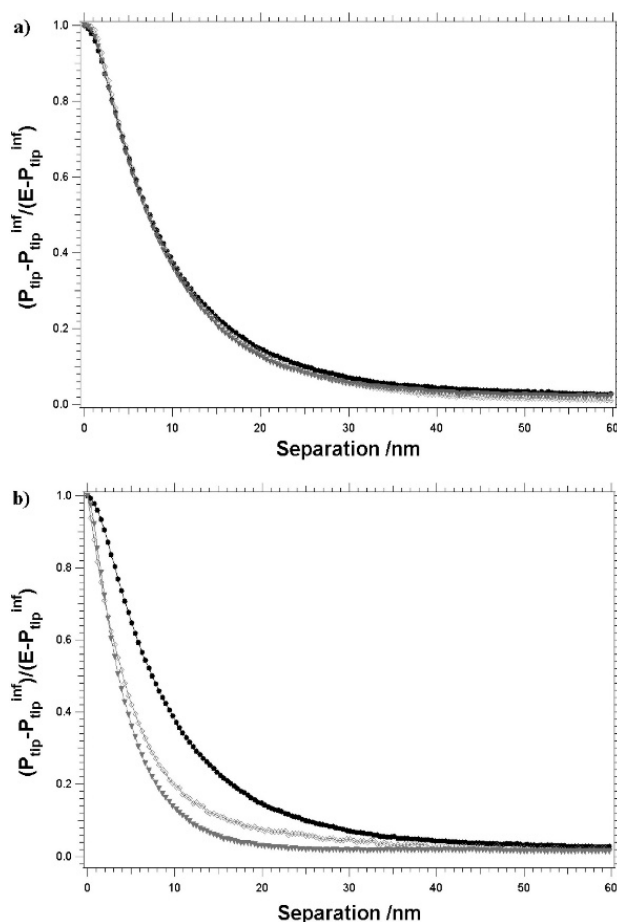


Figure 2.22 (a) Potentiometric approach curves on the Pt foil surface held respectively at +400 mV (filled black circles), +300 mV (filled grey triangles), and +200 mV vs PtPPy (empty grey boxes); (b) Influence of the electrolyte concentration on the double-layer profile obtained by approaching the Pt foil surface held at +400 mV vs PtPPy at 20 nm/s in 10 μ M (filled black circles), 100 μ M (filled grey triangles), and 1 mM (empty grey boxes) KCl.

There was no theory about the mechanism of SECPM potential detection published until 2018, when J. Friedl et al. proposed that at close tip-sample distance, SECPM may behave like EC-STM (Friedl et al., 2018). Despite the mechanism of SECPM suggesting no current flow within the SECPM cell, this model took the contribution of current, including tunnelling current due to close tip-sample separation, leakage current and the Faradaic current, into consideration. The regression fitted curve calculated using this model fits the experimental acquired data (Au surface in 10^{-4} mol dm^{-3} H_2SO_4 electrolyte at -0.8 V vs gold-gold oxide RE) quite well. However, the source

of Faradaic current remains unidentified since there should be no redox reactions in the electrochemical cell under the given experimental conditions. Another issue is that whether there is tunnelling current between the SECPM tip and the sample at close tip-sample separation is still controversial. Nevertheless, this model is currently the only option that can model the SECPM potential profiling profile curves and it will be discussed in detail in section 5.3.

Up to now there is still no generally accepted theory to interpret the potential-distance curves acquired by Woo et al.(Woo et al., 2004) and Hurth et al.(Hurth et al., 2007) in a quantitative way. More investigation is needed to be performed to understand the perturbation to the EDL from probe presenting close to the electrode surface.

Theories with non-constant electrolyte relative permittivity or further improvements on the EDL structure have to be developed in the future. Experimental works on the influence of tip apex geometry on the imaging and potential profiling could be helpful to test the numerical simulation results on this topic.

2.4.4 SECPM Tip Geometry

It has been proved experimentally that a sharp tip apex with minimum metallic part exposure from the insulation is the ideal choice for both EC-STM and SECPM imaging work (Hamou et al., 2010a). Considering the perfect probe fabrication done by Hurth et al. for their SECPM potential profiling experimental, the tip good enough for imaging may not be the first choice for local potential detection in EDL along the vertical direction.

Numerical simulation has been done by Hamou et al.(Hamou et al., 2010a, 2010b) on the geometry of SECPM probes. Depending on the sharpness and the protrusion length of apex from the insulation, three geometries were proposed (Figure 2.23) and simulated to investigate their performance in SECPM imaging and potential profiling experiments. Through the numerical analysis of surface charge density distribution along the protrusion apexes, it was suggested that the non-uniformly distributed charge density along the surface of the apex with long protrusion (Figure 2.23 a) will cause distortion of the EDL, resulting in inaccurate local potential distribution detection. A flat apex with minimum protrusion length from the insulation (Figure 2.23 c) would be ideal for SECPM potential profiling experiments.

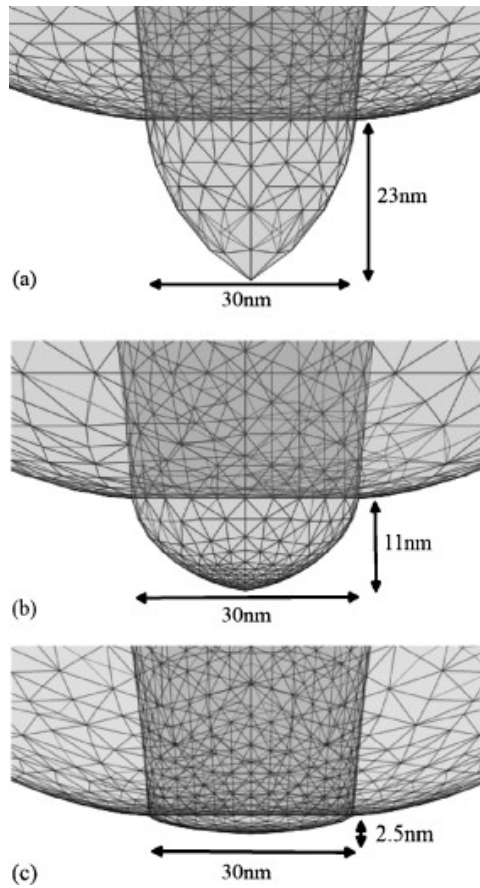


Figure 2.23 The metallic protrusion apices used in the simulation: (a) Geometry 1, (b) Geometry 2, and (c) Geometry 3.(Hamou et al., 2010b)

Chapter 3. Experimental

3.1 Chemical and Materials

3.1.1 Chemicals

The chemicals used in this work are listed in Table 3.1.

Chemicals	Formula	Provider	Purity
Sodium hydroxide	NaOH	EMSURE	99% - 100%
Sodium phosphate dibasic	Na ₂ HPO ₄	Sigma Aldrich	≥ 99.0%
Sodium phosphate monobasic	NaH ₂ PO ₄	Sigma Aldrich	≥ 99.0%
Sulfuric acid	H ₂ SO ₄	Sigma Aldrich	99.999%
Perchloric acid	HClO ₄	Sigma Aldrich	70%

Table 3.1 Chemicals used for experiments.

Metal wires used to prepare electrochemical scanning tunnelling microscopy (EC-STM) and scanning electrochemical potential microscopy (SECPM) probes and electrodes, including gold (Au) and platinum-iridium (Pt-Ir), were purchased from Goodfellow Cambridge Limited (UK). All wires were 0.25 mm in diameter. The gold wire had purity higher than 99.99%, while the Pt-Ir wire was with Pt:Ir ratio as 80:20.

Horseradish peroxidase (HRP) was purchased from Sigma Aldrich as high stabilized, essentially salt-free, lyophilized powder. It was kept in refrigerator at 4°C before using for experiments.

3.1.2 Preparation of Solutions and Electrolytes

The water used to prepare all the electrolytes and solutions was obtained from a PURELAB Option-Q water purification unit (VWR International, USA), with resistivity up to 18.2 M Ω -cm and total organic carbon lower than 10 ppb.

Phosphate buffer solutions (PBS) with different concentrations were prepared by mixing sodium phosphate dibasic and sodium phosphate monobasic in ultrapure water. To make the pH of PBS close to 7.4, concentration ration of NaH₂PO₄ and Na₂HPO₄ should be maintained as

$$[\text{HPO}_4^{2-}] / [\text{H}_2\text{PO}_4^-] = 1.5488.$$

The pH value of prepared PBS was monitored by a FiveEasy Standard pH meter (Mettler Toledo, UK), which was regularly calibrated using commercially purchased buffer solutions having pH 4 and 7 (Sigma Aldrich, Germany). NaOH or HCl was applied to adjust the pH of PBS to 7.4.

3.2 Scanning Probe Microscopy Instruments

All the scanning probe microscopy (SPM) related experiments for this thesis were done using a Multimode 8 SPM base (Bruker, USA) controlled by a Nanoscope V controller (Bruker, USA). A universal bipotentiostat (Bruker, USA) was used to perform electrochemical SPM experiments (Figure 3.1). Computer software Nanoscope 9.1 (Bruker, USA) was used for SPM data acquisition. Computer software NanoScope Analysis 1.5 (Bruker, USA) was used for SPM image analysis and generation.

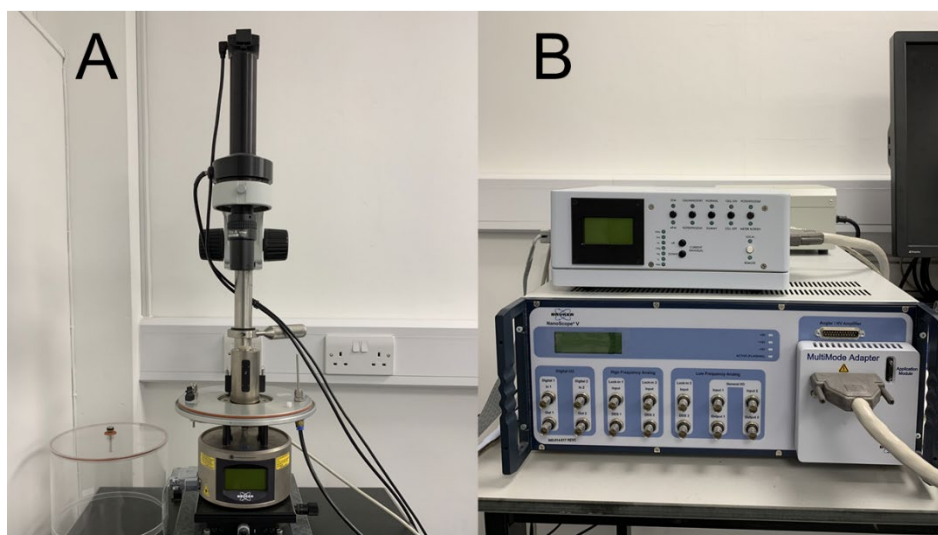


Figure 3.1 Bruker STM setup. (A) Bruker multimode 8 SPM base; (B) Bruker Nanoscope V controller and universal bipotentiostat.

3.2.1 Atomic Force Microscopy

Atomic force microscopy (AFM) in air, in liquid and electrochemical AFM (EC-AFM) share the similar hardware setup (Figure 3.2 A). Different tip holders are required for different AFM working conditions. An MFMA stainless steel tip holder (Bruker, USA) is used for AFM in air conditions (Figure 3.2 B). It enables low-frequency, high amplitude force imaging. An MTFML glass tip holder (Bruker, USA) is designed for AFM in liquid conditions (Figure 3.2 C). For EC-AFM, an MMTMEC glass tip holder (Bruker, USA) is usually applied (Figure 3.2 D). The main differences for these two glass tip holders are an extra port and a small hole prepared for reference electrode and counter electrode, respectively.

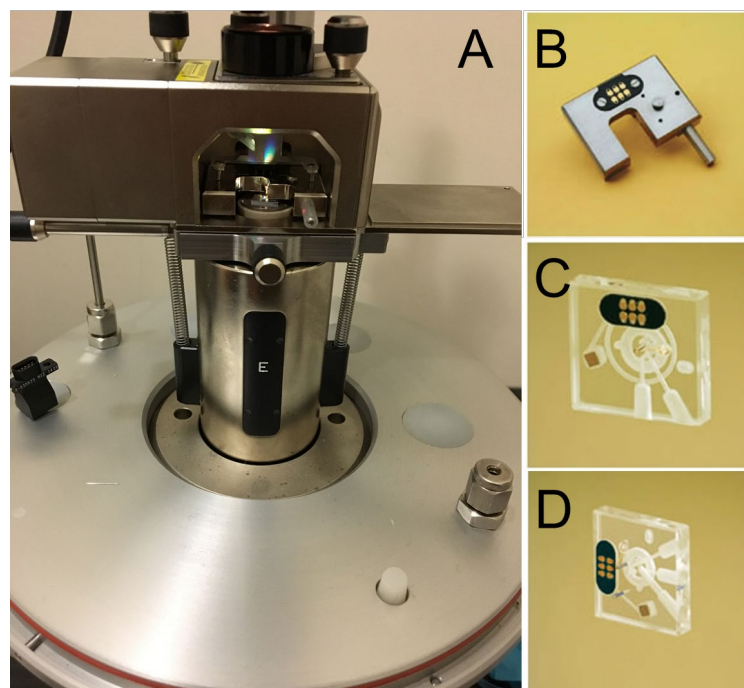


Figure 3.2 AFM setup and tip holders. (A): AFM head installed on the scanner; (B): MFMA stainless steel tip holder for AFM in air; (C): MTFML glass tip holder for AFM in liquid; (D): MMTMEC glass tip holder for EC-AFM.

For different AFM working conditions, different probes are required. For the experiments in the thesis, SCANASYST-AIR probes (Bruker, USA) were used for AFM in ambient condition. SCANASYST-FLUID+ probes (Bruker, USA) were used for both AFM in liquid conditions and EC-AFM.

The AFM mode in Bruker Multimode 8 base requires a flat sample attached to a stainless-steel sample mounting disk (Bruker, USA). For AFM in air and liquid, there is no requirement for the sample conductivity so the connection between sample and the mounting disk can be insulating double side adhesive tape. While for EC-AFM, where conductivity is indispensable, silver two-part conductive adhesive, Resin and Hardener (Fisher Scientific, UK) should be used to join the sample and the sample mounting disk together.

3.2.2 Scanning Tunnelling Microscopy

The Bruker Multimode 8 SPM base is designed to perform AFM, STM and SECPM using the same instrument. A different type of tip holder (Figure 3.3) is required to do STM in air, in liquid and under electrochemical conditions.

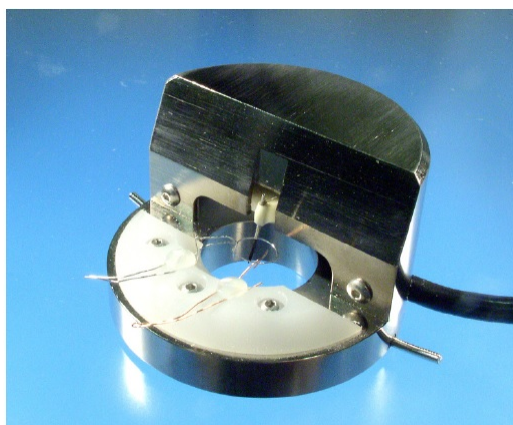


Figure 3.3 STM converter head and tip holder.

STM in air mode requires a sharp probe (without insulation coating) and a conductive sample. Usually, STM in air shares the same sample preparation method with EC-AFM. Probe preparation will be introduced in section 3.3.

Unlike the tip holders used for AFM in liquid and EC-AFM, STM tip holder does not have the liquid holding chamber to provide the liquid or electrochemical environment. Instead, a fluid cell (Figure 3.4) is often used as a liquid or electrolyte container. A Teflon top and a stainless-steel bottom are joint together by four screws, with sample (HOPG in the work) tightly clamped in between, forming a sandwich-like structure.

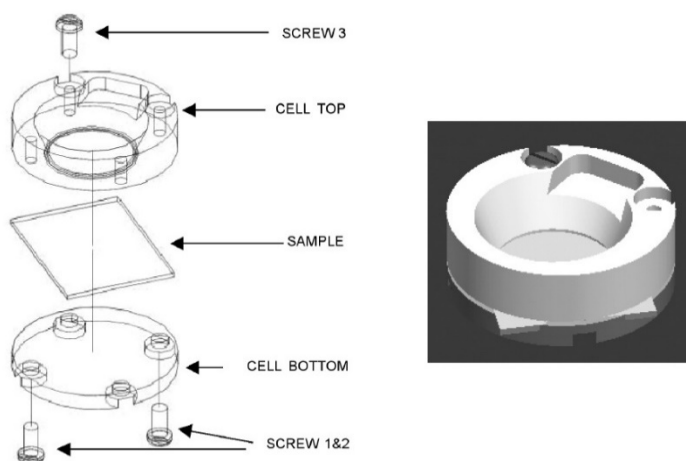


Figure 3.4 EC-STM fluid cell, exploded (left) and assembled (right).

It is of great importance to scan the same sample surface using all the EC-SPM techniques, and this can be achieved only if the sample preparation procedures are the same for EC-AFM and EC-STM. Because of the size difference, the Teflon made EC-STM cell cannot fit with the tip holders designed for AFM in liquid condition and EC-AFM. In the experimental work for this thesis, an alternative method was taken that using the ring-shape counter electrode (CE) on the EC-STM tip holder to hold the electrolyte (Figure 3.5). Due to the existence of liquid surface tension, electrolyte can be held by the counter electrode and stay as a hemisphere structure on the sample surface.

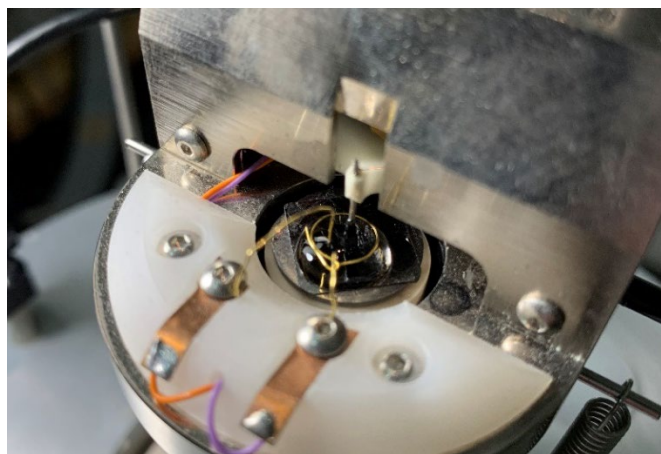


Figure 3.5 Ring-shape counter electrode holding the electrolyte for EC-STM and SECPM.

And environmental control hood is usually used to maintain a noble gas atmosphere (Figure 3.6), with nitrogen or argon. To maintain a relatively humid environment in the hood to minimise the electrolyte evaporation, noble gas can be introduced into the environmental hood through a water filled gas washing bottle.

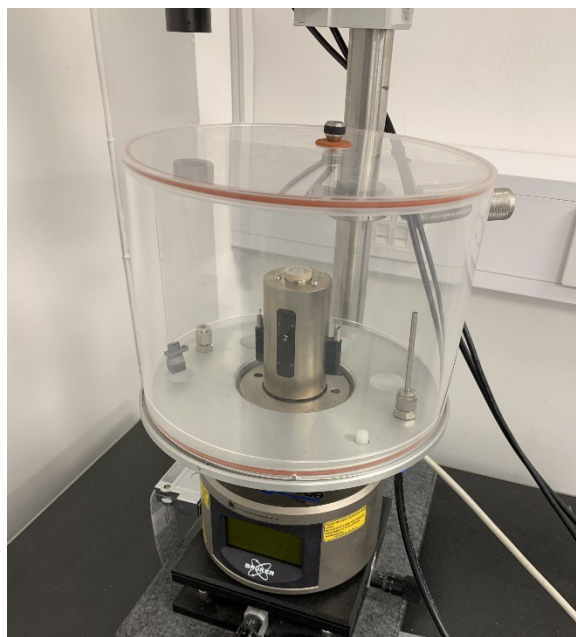


Figure 3.6 Environmental control hood to maintain the noble gas atmosphere and humidity

3.2.3 Scanning Electrochemical Potential Microscopy

SECPM shares the same setup with EC-STM. For SECPM imaging experiments, the requirements for sample preparation, electrodes, electrolytes, and probes are also the same as EC-STM.

However, an SECPM tip holder (Figure 3.7) is slightly different from a conventional STM tip holder. An SECPM head has an SECPM switch gain, and it should be set in accordance with the SECPM sensitivity parameter (determines the SECPM potentiometer sensitivity) which can be changed in Nanoscope 9.1 software. On the STM head, reference and counter electrodes are connected to the potentiostat through a clip-leads cable, while on the SECPM head, the electrode connection cable is integrated in the head. The SECPM tip holder can also be used in (EC-)STM experiments, so it is easy to switch between EC-STM and SECPM for direct comparison between the images of the same location taken by these two techniques. In thesis, all the (EC-)STM and SECPM experiments were done using the SECPM tip holder.

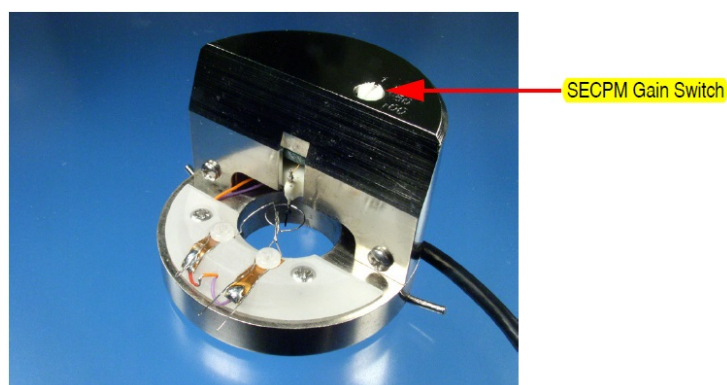


Figure 3.7 SECPM head and tip holder.

3.3 Probe Fabrication

Probes for all the AFM techniques were commercially purchased from Bruker, USA. (EC-)STM and SECPM probes were prepared in the lab.

3.3.1 Probes for Imaging

All the (EC-)STM and SECPM probes mentioned in the thesis were prepared by mechanical cutting using scissors or a wire cutter.

For STM and EC-STM imaging, the probes were cut to be as sharp as possible. Before cutting, probe wires were annealed by butane flame to remove possible contaminations. After annealing, scissors or wire cutter are used to cut from a steep angle to generate a sharp apex.

The sharp probes can be used directly for STM in ambient condition. But in order to do EC-STM, probes are required to be coated by insulating materials, such as Apiezon wax, nail polish or any insulating polymer materials, leaving only the very top apex exposed, to minimise the influence from Faradaic current.

A homemade setup was applied for probe insulating (Figure 3.8). Plastic melted from Eppendorf tips was used for all the probes, since it was inert in aqueous electrolytes, easier to control than Apiezon wax during coating because of being transparent and took much less time to harden than nail polish.

To coat the probe, the sharp cut wire used as probe was hold tightly by pliers, with the sharp end pointing up. Plastic was melted and fulfilling in the 2 mm wide gap in the copper melting pad connecting to soldering iron or sitting on a ceramic hotplate (ThermoFisher Scientific, USA). Carefully holding the pliers, the sharp apex was positioned perpendicular to the melted plastic from below. Slowly, the probe was elevated, penetrating the melted plastic, with plastic covering the probe, leaving only the sharp apex exposed. Then the tip was removed from the gap to leave the plastic for hardening. Pt-Ir wire with a sharp apex is stiff enough to penetrate the melted plastic, having the exposed apex large enough to perform EC-STM imaging experiments, and in the meantime small enough to control the faradaic leakage current lower than 50 pA.

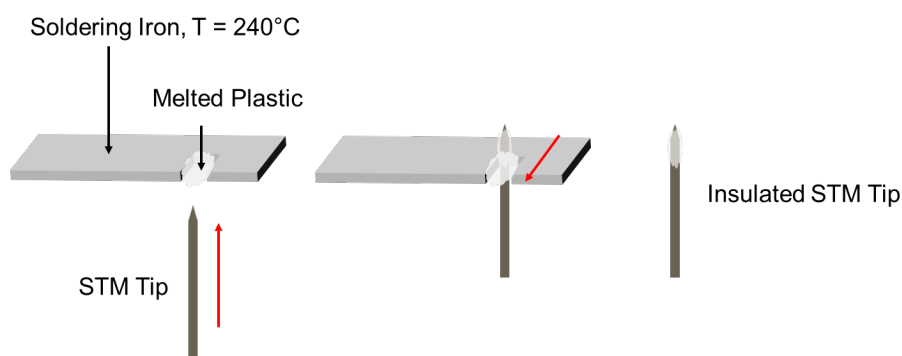


Figure 3.8 Schematic drawing of the tip insulating using melted plastic on top of a temperature-controlled soldering iron.

While soft metals, like gold, are not strong enough to penetrate the melted plastic. The gold apex will be covered completely, leading to the failure of generation and detection of tunnelling current. So gold probes were usually coated by Apiezon wax, which was softer than melted plastic, using the same method mentioned above.

3.3.2 Probes for SECPM Potential Profiling

R.F. Hamou et al. published their research on how the tip apex geometry will influence the potential mapping by SECPM using numerical simulation method (Hamou et al., 2010b). A metallic probe with flattened protrusion is preferred in SECPM potential profiling work. Here in this thesis, flat cut coated Pt-Ir (80-20) probes were used to acquire the potential approach curves. These probes were prepared by cutting regularly coated probes prepared for imaging using scissors from direction perpendicular to the probe (Figure 3.9) to create a flat cross section exposed from the insulation coating. The prepared probes were imaged by scanning electron microscopy to check the conditions of the cut surface (Figure 3.10).

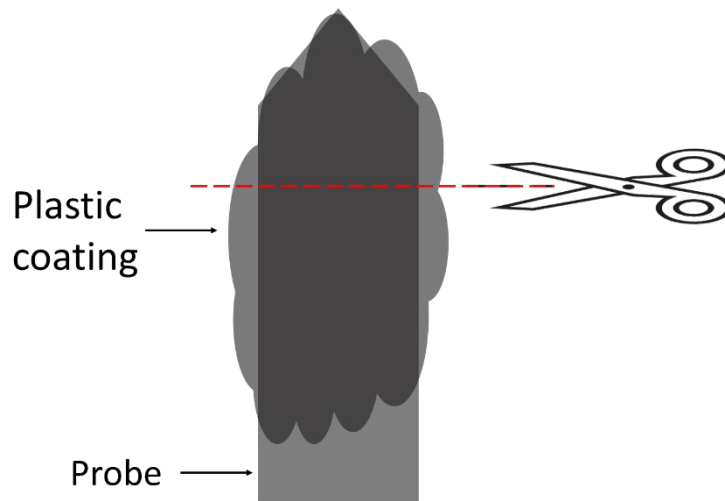


Figure 3.9 Preparation of SECPM potential profiling probes.

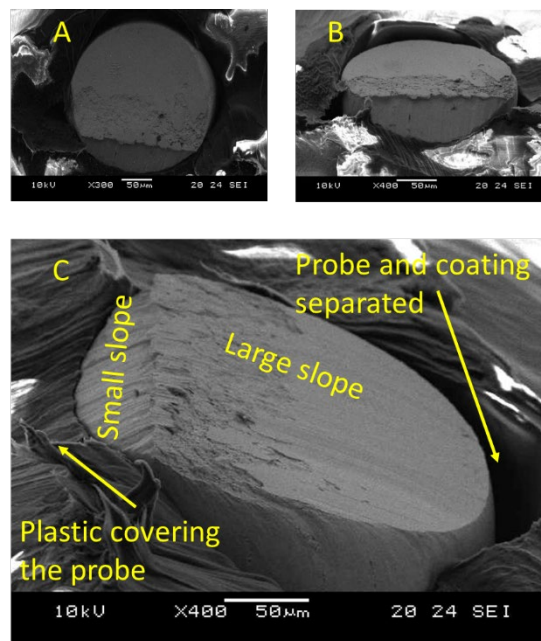


Figure 3.10 SECPM potential profiling probe imaged by SEM from different angles.

The protrusion part of scissors cut probe consists of two slopes. The larger one was made by the active movement of one of the two blades of the scissors driven by the thumb, while the smaller slope was made by the counter movement of the other blade. In order to avoid the influence of tip apex geometry to SECPM potential detection, the ideal case is to have the large slope being parallel to the substrate surface. The

curvature of the tip holding tube and the wire to prepare probes were used combinedly to keep the larger slope of the tip apex as parallel as possible to the substrate surface (Figure 3.11).

Except for the probe apex geometry, the other hardware setup for SECPM imaging and potential profiling are all the same.

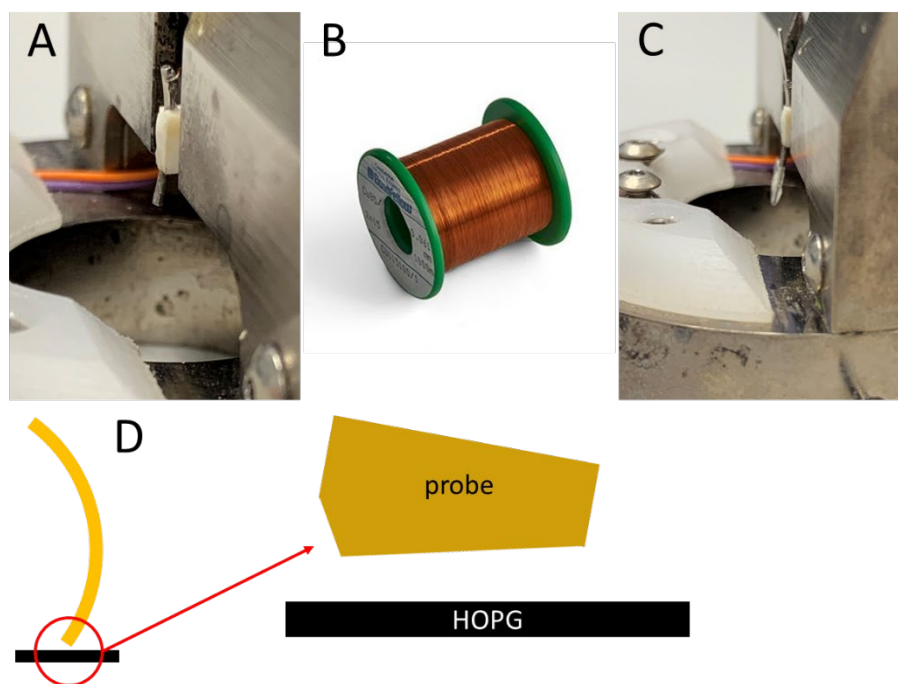


Figure 3.11 SECPM potential profiling probe installation. (A) The probe holding tube with curvature; (B) Curvature of metal wire used to prepare the probes; (C) Probe installation; (D) illustration of relative position between the probe and the substrate.

3.4 Working Electrode

For all the EC-SPM experiments mentioned in this thesis, a four-electrode configuration, composed of two working electrodes (WE): the probe and the substrate, a counter electrode (CE) and a reference electrode (RE).

As the electron donor or acceptor of the analyte existing at the interface or in the electrolyte, WE should have a wide potential window for electroanalysis. As the substrate for SPM techniques, the WE surface should be uniform, flat, clean and sometimes conductive for certain techniques like EC-STM. Among all the substrate

materials, highly oriented pyrolytic graphite (HOPG) is a particularly promising candidate.

HOPG is a high purity carbon material with mechanical and physical properties close to natural graphite monocrystal (Lapshin, 1998). It is categorized as a lamellar material and consists of stacked planes. Within each single plane, every sp^2 hybridized carbon atom interacts with three nearest carbon atoms through covalent bond, forming a honeycomb-like 2-dimensional structure. Single carbon layers are joint together by Van der Waals force between adjacent planes.

HOPG can be easily renewed by adhesive tape to generate atomic level flat surface structure. It provides a background with only carbon in the elemental signature, which makes the background featureless where elemental analysis is required. As a conductive material, HOPG is an ideal substrate for SPM investigation on redox active proteins.

ZYB grade HOPG samples (Bruker, USA), with dimensions 12 mm * 12 mm * 2 mm (length * width * thickness), were used as WE for all the EC-SPM experiments in this thesis.

3.5 Counter and Reference Electrode

3.5.1 Counter Electrode

CE should not participate in the electrochemical reactions except to balance the current observed at the WE. It should be highly stable in the electrochemical environment and be highly conductive to accomplish the current path. Gold wire (0.25 mm in diameter, GoodFellow Cambridge Ltd, UK) was used as counter electrode for all the EC-SPM experiments in this thesis.

3.5.2 Reference Electrode

RE is the electrode that has a stable electrochemical potential, according to which the potential on WE can be controlled and measured precisely. A redox system with every participator in the redox reaction kept at constant concentration is usually employed to achieve high electrochemical potential. Commercially purchased reference electrodes are well built to meet various requirements, but they cannot be used for EC-SPM experiments due to the limited space in the EC-SPM setups.

For EC-STM experiments, wire reference electrodes are commonly used as alternatives. Compared to conventional reference electrodes, wire reference electrodes have several advantages. As metal wires immersed directly in the electrolyte, they have small ohmic resistance effect, no liquid junction potential and no contamination coming from the ion transfer through the membrane where a conventional reference electrode gets in contact with the electrolyte.

Wire reference electrodes should be chosen carefully according to the experimental conditions, and constantly calibrated before and after every experiment. A silver wire covered by a thin silver chloride layer is a common choice for EC-SPM experiments using electrolyte with chloride ions, while other wires could also be applied depending on different experimental requirements (Table 3.2).

RE	WE	CE	Electrolyte
Pt (Liang et al., 2019)	Pt (111)	Pt	0.1M KOH/LiOH/CsOH
Ag (Wang et al., 2008a)	HOPG with GOx	Au	PBS (pH = 7.2)
Pb (McCann, 2004)	Au (111)	Pt	1.0 mM Pb (ClO ₄) ₂ + 0.1 M HClO ₄
Ag/AgCl (Matsumoto et al., 2009)	HOPG	Pt	0.1M HClO ₄
Gold-gold oxide (Wolfschmidt et al., 2010)	Au (111)	Au	0.1M HClO ₄

Table 3.2 Some examples of wire reference electrodes.

For all the EC-SPM experiments mentioned in this thesis, gold-gold oxide wire was applied as the reference electrode. It was prepared by electrochemical oxidation (Figure 3.12). Two gold wires (diameter 0.25mm, length 5 cm) were used as working and counter electrode respectively and immersed in 1M sulfuric acid solution. The two electrode wires were connected to a direct current (DC) power supplier. A 12-volt potential was applied to this system for 3 minutes, after which the working electrode (connected to the positive pole of the power supply) was taken out, rinsed carefully by distilled water, and then used as the reference electrode.

All the potentials mentioned in this thesis are with reference to standard hydrogen electrode (SHE) unless there are specific explanations.

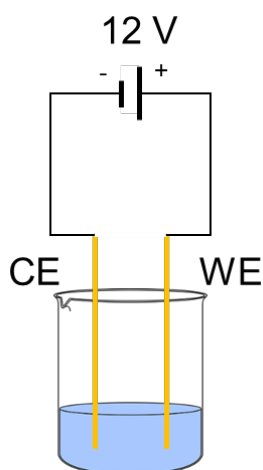


Figure 3.12 Schematic drawing for gold-gold oxide RE preparation.

Calibration was required before and after the reference electrode being used in EC-SPM experiments. The gold-gold oxide wire was immersed in 10 mM PBS as working electrode. By measuring its open circuit potential with reference to a mercury-mercurous sulphate electrode stored in 1 M Na_2SO_4 solution, the potential of the wire electrode can be calculated.

3.6 Electrochemical Setups and Instruments

3.6.1 Electrochemical Cell

In order to have consistency in the experimental results, it is ideal to perform both the electrochemical characterisations, such as cyclic voltammetry (CV) and electrochemical impedance spectroscopy (EIS), and EC-SPM imaging with the same sample. The sample used for EC-SPM imaging was a commercially purchased HOPG attached to a stainless-steel sample mounting disk by silver two-part conductive adhesive, Resin and Hardener. However, in a conventional electrochemical glass cell with standard three electrodes configuration, the working electrode, in this case the EC-SPM sample, was required to be immersed completely in the electrolyte. The existence of the sample mounting disk and silver containing adhesive will influence the accuracy of the electrochemical experimental results. Additionally, aqueous electrolyte will dissolve the adhesive, leading to the separation of HOPG and sample mounting disk. Therefore, all the electrochemical characterisations were performed using the similar setup as EC-STM and SECPM, with some minor modifications for potentiostat connection (Figure 3.13).

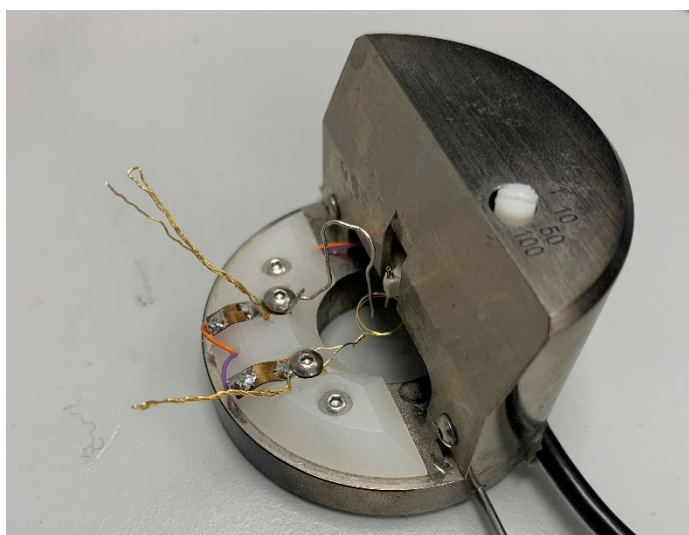


Figure 3.13 Modified SECPM head for electrochemical characterisation.

Two pieces of gold wire were soldered to the metal plates for CE and RE connection on the SECPM to provide connections for potentiostat. Another piece of gold wire was

planted in the silver two-part conductive adhesive, Resin and Hardener, with extra part sticking out for potentiostat WE connection. As in the case for EC-SPM experiments, the ring-shape counter electrode could hold the electrolyte to maintain the electrochemical environment and the environmental hood was used to maintain the noble gas atmosphere.

3.6.2 Potentiostat

A potentiostat is the electronic hardware to control the potential in a three-electrode electrochemical cell, and then to investigate the redox reaction mechanisms. A potentiostat can apply potential to the WE with reference to the RE, leading to a current flow between WE and CE.

The potentiostatic control during EC-SPM experiments were achieved by a universal bipotentiostat (Bruker, USA). CV and EIS experiments were performed with a commercially purchased BioLogic SP-300 potentiostat and corresponding EC-Lab software (BioLogic Science Instruments, France) for data acquisition and potentiostat control.

3.7 Sample Preparation

3.7.1 HOPG Functionalization

HOPG surface can be easily cleaned by removing the top layers using Scotch tape. Freshly cleaved HOPG has a hydrophobic surface, on which most water-soluble global proteins cannot adsorb due to lack of active sites for binding. A conventional method to create active sites on HOPG surface is electrochemical oxidation. By applying potential sweeps to a freshly cleaved HOPG surface immersed in electrolyte, surface defects and oxygen containing hydrophilic functional groups, including carboxyl, hydroxyl and carbonyl groups could be formed(Otake & Jenkins, 1993) and they can promote protein adsorption on the surface through dipole-dipole and ion-dipole interactions (Rabe et al., 2011).

In this thesis, HOPG surface was thermally oxidized in air to create active sites for protein binding. HOPG with a freshly cleaved surface was placed in a muffle furnace with temperature controlling system (Naberthermal GmbH, Germany). The whole annealing procedure consisted of three stages. The first stage, temperature raising from room temperature (20 °C) to 650 °C, took 1 hour. The second stage was holding the temperature at 650 °C for 3 minutes. In the third stage, heating was terminated and the HOPG was kept in the oven until the temperature gradually decreased back to room temperature.

Although freshly cleaved HOPG surface is atomically flat, there are still some defects, such as step edges and grain boundaries existing on the surface. With temperature lower than 700 °C, oxygen in air reacts with the carbon atom at these defects on HOPG surface because of having unsaturated sp^2 orbitals (Chang & Bard, 1991). These reactions roughen the surface, create more defects, and generate oxygen-containing functional groups, which helps proteins to adsorb on the annealed surface.

3.7.2 HRP Immobilisation

Protein immobilisation was done by drop casting method. Commercially purchased HRP powder was dissolved into 10 mM PBS to prepare 0.04 mg/ml HRP solution. The prepared HRP solution (150 μ L) was dropped on the annealed HOPG surface, being left for 2 to 3 hours, then rinsed by PBS solution to remove the weakly bonded HRP molecules. To minimise the influence of solvent evaporation, a glass hood was used to cover the HOPG with HRP solution drop on it during the immobilisation procedure.

Chapter 4. Potential Dependent Capacitance Behaviour of Horseradish Peroxidase

4.1 Electrode Surface Morphology: SPM Characterisation

AFM in aqueous, EC-STM and SECPM were applied to investigate the freshly cleaved HOPG (f-HOPG) and annealed HOPG (a-HOPG) surfaces (Figure 4.1). Using the method mentioned in the previous chapter, the three SPM techniques could scan the same surface for better comparison and avoid causing any possible damage to the sample. As can be seen from figure 4.1, from the images captured by all the three SPM techniques, f-HOPG surface is characterised as atomically flat, with only a few sharp steps, while the a-HOPG surface shows more defects, including large round pits (Figure 4.1 B), small irregular holes and hackly step edges (Figure 4.1 D and F). This result is in agreement with the study published in 1991 by Alan J. Bard and Hsiangpin Chang (Chang & Bard, 1991) in which they investigated the oxidation of HOPG in air at elevated temperature.

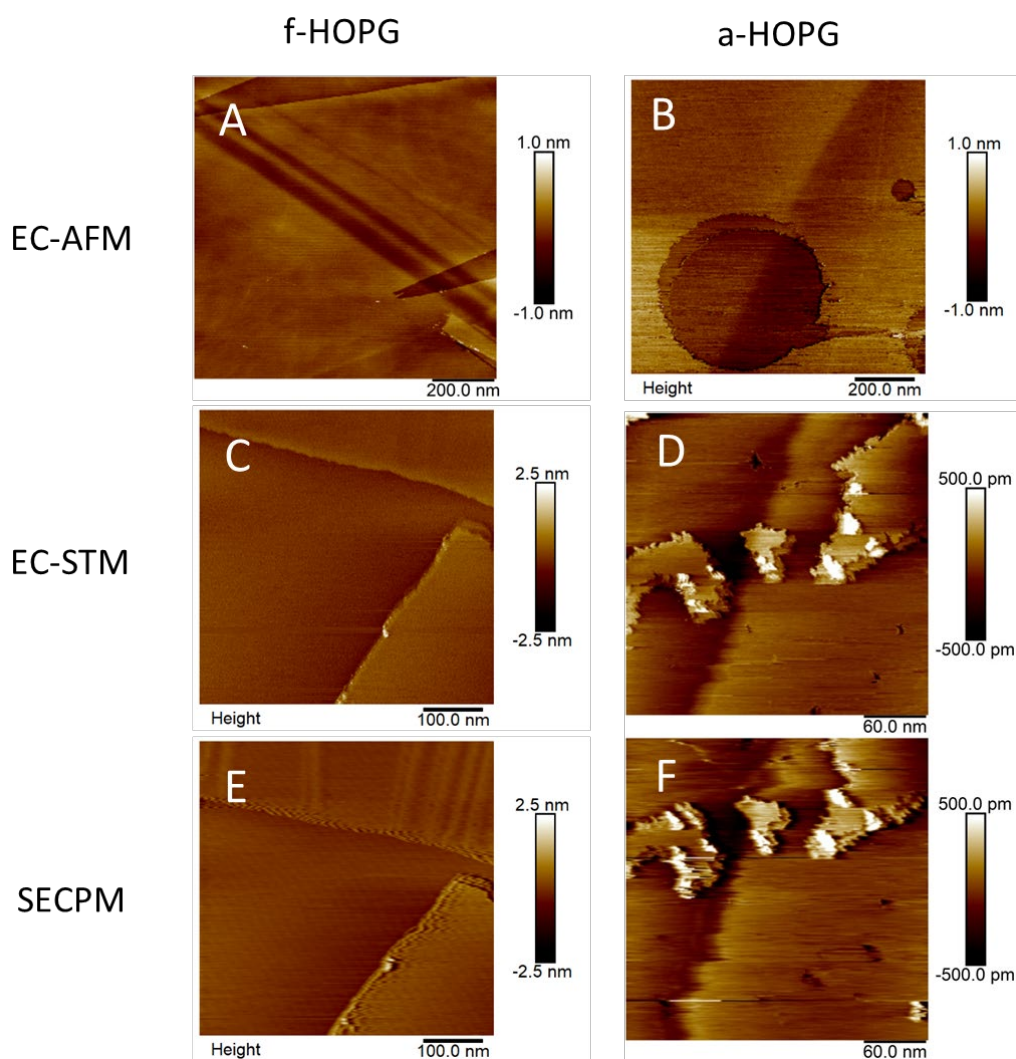


Figure 4.1 Images of f-HOPG and a-HOPG in 10 mM PBS (pH 7.4) captured by AFM in liquid (A and B), EC-STM (C and D) and SECPM (E and F).

Also, since EC-STM and SECPM share the similar hardware, it is easy to switch between these two techniques without doing any change to the experimental setup, leading to direct comparison of images of the same area captured by two different imaging techniques. From figure 4.1 C, D, E and F, the images of the same area captured by EC-STM (constant current mode, current setpoint = 300 pA, bias voltage = 400 mV) and SECPM (constant potential mode, potential setpoint = 20 mV) respectively, similar topological structure of the surface (both freshly cleaved and annealed) are observed, with little distortion and broader edges observed from the SECPM images.

Considering the characteristic of having no requirement for sample conductivity and the convenience in operation, AFM was applied to check the outcome of HRP

immobilisation procedure and estimate the coverage of HRP on a-HOPG surface. Figure 4.2 shows images of a-HOPG surfaces after HRP adsorption done by drop casting HRP solutions with varying concentrations (A: 1 mg/mL; B: 0.1 mg/mL; C and D: 0.04 mg/mL). In figure 4.2 A, mainly large clusters, the average size of which is around 100 nm (length) * 50 nm (width) * 5 nm (height), are observed. Considering the size of a single HRP molecule (54 * 54 * 3.2 Å) (Baier & Stimming, 2009), one cluster like these could be formed by around 300 HRP molecules. The formation of large clusters suggests that the relatively high HRP solution concentration (1 mg/mL) leads to strong intermolecular interaction. To minimise the intermolecular interaction, HRP solutions with lower concentrations were applied in the HRP immobilisation procedure. Figure 4.2 B shows the image of a-HOPG surface after drop casting with 0.1 mg/mL HRP solution. Compared to figure 4.2 A, there are fewer large clusters and more smaller clusters (average size 50 * 50 * 5 nm³). Other than the clusters, oligomers with average size 20 * 20 * 3 nm³ could also be observed. After furtherly decreasing the concentration of HRP solution used in drop casting to 0.04 mg/mL, only oligomers and single molecules are observed from the AFM images (Figure 4.2 C and D).

Based on this result, all the HRP modified a-HOPG electrodes mentioned in the following sections were prepared using 0.04 mg/mL HRP solution.

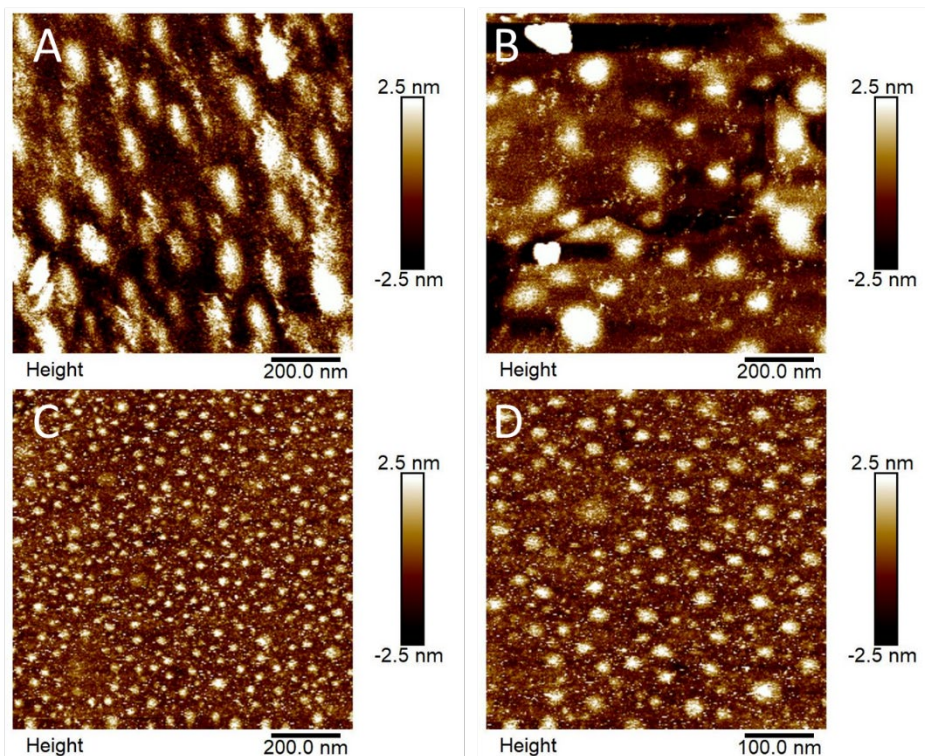


Figure 4.2 AFM images of a-HOPG surfaces with HRP modification done by drop casting technique using (A) 1mg/mL, (B) 0.1 mg/mL and (C and D) 0.04 mg/mL HRP solutions.

4.2 Electrochemical Characterisation: Cyclic Voltammetry

HRP is well investigated by cyclic voltammetry (CV) as the catalyst of hydrogen peroxide decomposition. The redox reaction of HRP itself on HOPG surface is not thoroughly studied. S. Li *et al.* (Zhao *et al.*, 2002) reported their work about HRP modified glassy carbon electrode (HRP-GC) and carbon nanotube powder microelectrode (HRP-CNTPME). No well-defined redox peaks were observed from the CV of HRP-GC. But redox reactions of $\text{Fe}^{3+}/\text{Fe}^{2+}$ couple in HRP active centre were identified from the CV of HRP-CNTPME. Compared with glassy carbon, carbon nanotube powders contain large number of defects, leading to high surface activation, and nano-sized powder particles could act as molecule wires that benefit the direct electron transfer to HRP redox active centre.

In this work, HRP molecules were adsorbed on annealed HOPG (a-HOPG), the surface of which was rougher than that of freshly cleaved HOPG (f-HOPG) but had much smaller number of defects than carbon nanotube powders.

CV was recorded in 10 mM PBS solution on f-HOPG, a-HOPG and a-HOPG surface with HRP adsorption (HRP-HOPG) and the curves are shown in figure 4.3.

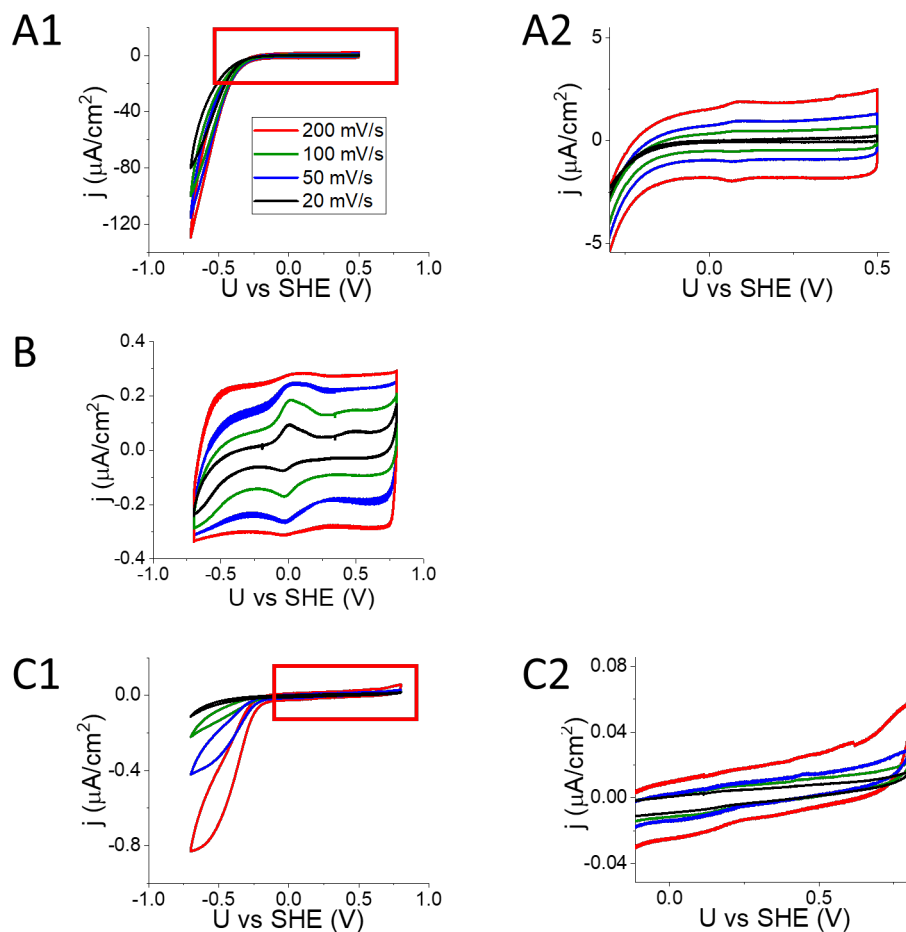


Figure 4.3 CV of (A1) f-HOPG, (B) a-HOPG and (C1) HRP-HOPG recorded in 10 mM PBS (pH 7.4) in argon atmosphere at various scan rates (black: 20 mV/s, green 50 mV/s, blue: 100 mV/s, red: 200 mV/s). (A2) and (C2) are amplification of the corresponding parts (in the red square) in (A1) and (C1), respectively.

From the CV curves of f-HOPG (Figure 4.3 A1 and A2), redox peaks are observed at around 0.05 V. Steep current density (j) increases are observed when the potential being more negative than -0.25 V.

From the CV of a-HOPG (Figure 4.3 B), oxidation peaks are observed at around 0.05 V and corresponding reduction peaks are observed at around -0.02 V. This reversible reaction could be attribute to the oxygen containing functional groups formed during the annealing procedure.

It can be seen from the CV curves that after annealing, current density decreased dramatically to be 10^{-3} of the values of f-HOPG. After annealing, the carbon atoms forming the honeycomb-like 2-dimensional structure are oxidized into functional groups, resulting in the destruction of regularized in-plane structure, through which electrons could move freely.

In figure 4.3, C1 and C2 depict the CV curves of HRP-HOPG system. Compared with the CV of f-HOPG and a-HOPG, no obvious redox peaks are observed from the CV curves of the HRP-HOPG system. One possible explanation is the oxygen containing functional groups on the annealed HOPG surface are hindered physically and chemically as a result of HRP immobilisation. HRP molecules are bonded to the a-HOPG surface through Van der Waals force, hydrogen bond and covalent bond. The coverage of HRP molecules physically linked onto a-HOPG surface diminishes the exposure of functional groups on the electrode surface to the electrolyte. Chemically speaking, the outpointing sidechains of the amino acid residues located on the surface of the globular HRP tertiary structure could covalently linked to the oxygen containing functional group. Both factors contribute to the reducing the amount of oxygen containing functional groups on a-HOPG surface that can participate in the redox reactions.

Table 4.1 lists the charge accumulation during the scanning procedure calculated from the CV curves of HRP-HOPG system. As can be seen from table 4.1, the amount of accumulated charge is not significantly dependent on the sweep rate, which indicates the current observed from the CV in figure 4.3 C1 and C2 is charging current, further suggests HRP molecules on a-HOPG/PBS interface could behave like capacitors.

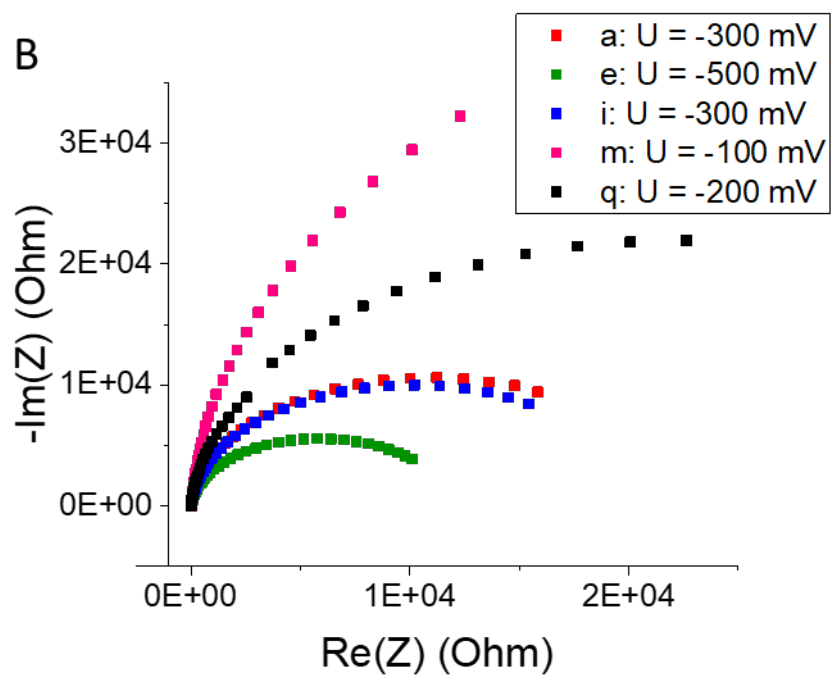
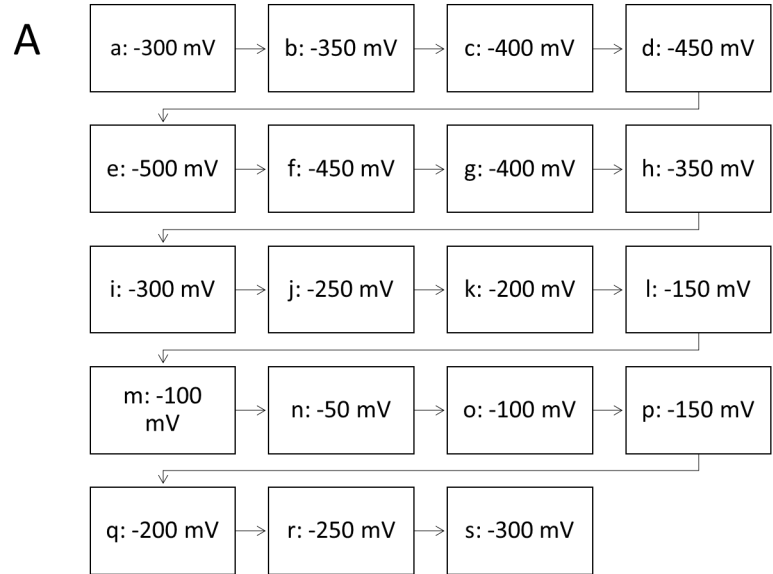
Sweep rate (mV/s)	Charge ($10^{-6}C/cm^2$)
20	1.8364
50	1.7907
100	1.5828
200	1.6176

Table 4.1 Charge accumulation calculated from CV of HRP modified a-HOPG in 10 mM PBS (pH 7.4).

4.3 Potential Dependent Capacitance Measurement: Electrochemical Impedance Spectroscopy

4.3.1 Freshly Cleaved HOPG and Annealed HOPG

Electrochemical impedance spectroscopy (EIS) was performed on f-HOPG and a-HOPG to learn more about how the thermal treatment will influence the electrochemical behaviour. Impedance spectra for f-HOPG were recorded between the potential range -0.5 V and -0.05 V (Figure 4.4) while those for a-HOPG were recorded between -0.5 V to 0.45 V (Figure 4.5) to determine the point of zero charge. The capacitance of the electrochemical double layer (C_{EDL}) at each potential was calculated from the spectra using the equivalent circuits in figure 4.6, where R_s is the solution ohmic resistance, C_{EDL} is the capacitance of the electrochemical double layer at solid-liquid interface and R_{ct} is the charge transfer resistance. The best fitting values for the spectra in figure 4.4 and figure 4.5 are listed in table 4.2 and 4.3, respectively.



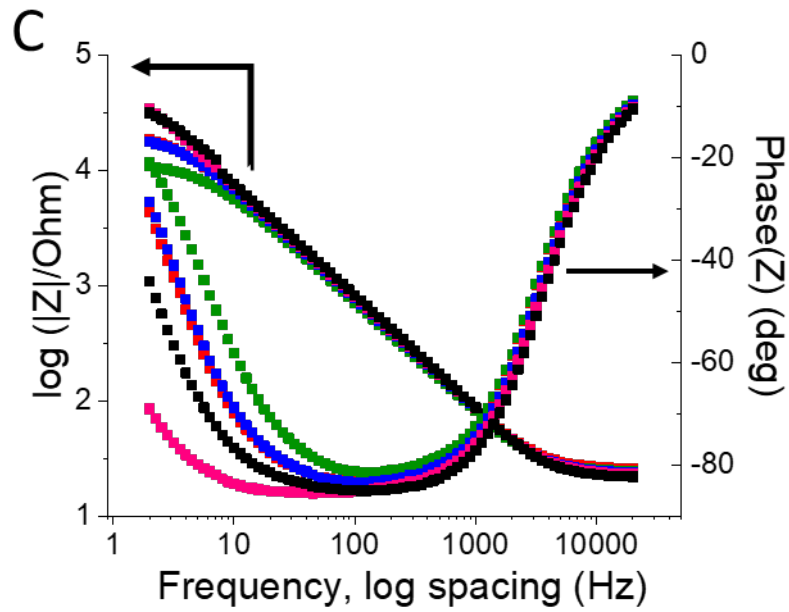
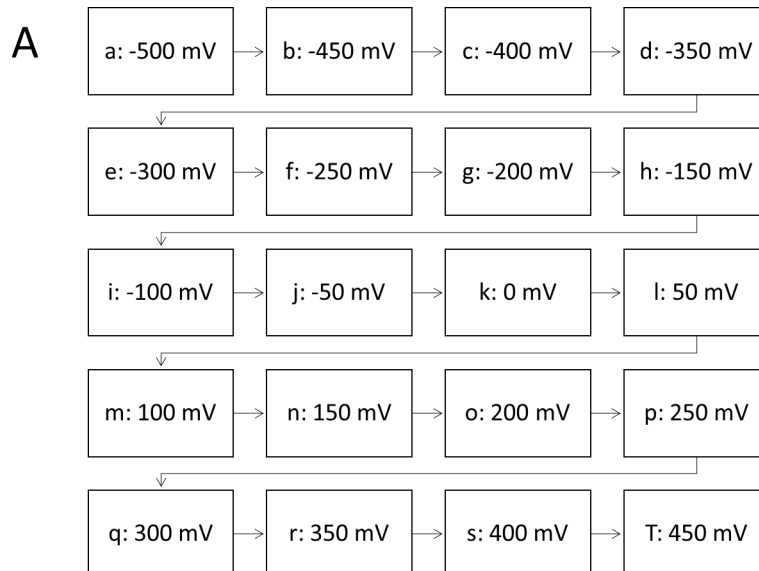


Figure 4.4 Impedance spectra recorded on f-HOPG surface in 10 mM PBS. (A): Substrate potential changing pattern according to which the impedance spectra were recorded. (B): Nyquist plot. (C): Bode plot.



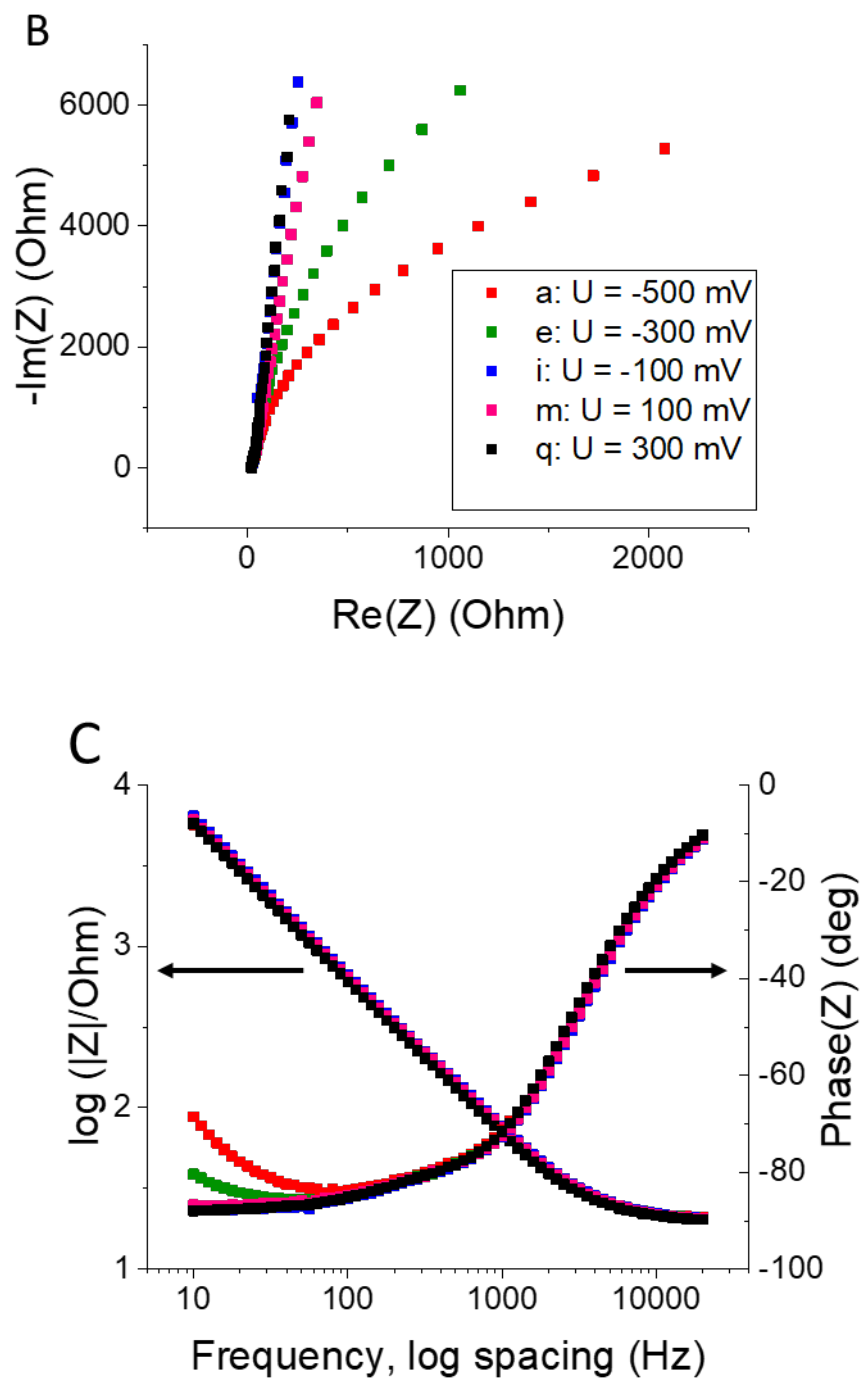


Figure 4.5 Impedance spectra recorded on a-HOPG surface in 10 mM PBS. (A): Substrate potential changing pattern according to which the impedance spectra were recorded. (B): Nyquist plot. (C): Bode plot.

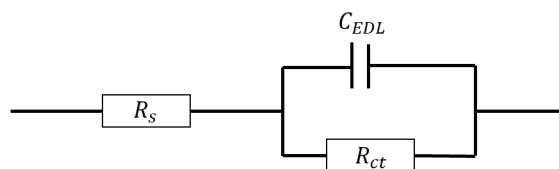


Figure 4.6 Equivalent circuit model to analysis the impedance spectra of f-HOPG and a-HOPG in PBS. R_s is the solution ohmic resistance, C_{EDL} is the electrochemical double layer capacitance and R_{ct} is the charge transfer resistance of the electrode surface.

U (mV)	R_s (Ohm)	R_{ct} (Ohm)	C_{EDL} ($\mu\text{F}/\text{cm}^2$)
-300	24.66	61380	4.525
-350	24.34	45020	4.562
-400	23.99	24120	4.644
-450	23.49	20130	4.348
-500	23.26	17000	4.837
-450	23.06	20810	4.751
-400	22.99	22770	4.254
-350	22.92	31320	4.478
-300	22.74	48560	4.388
-250	22.56	64230	4.307
-200	22.33	107500	3.878
-150	22.11	202100	4.305
-100	21.87	453500	4.387
-50	21.64	1.69E+06	4.460
-100	21.31	441500	4.308
-150	21.11	204900	4.136
-200	21.08	102500	3.824
-250	20.47	60590	4.066
-300	20.05	45190	4.099

Table 4.2 Fitting results calculated from the impedance spectra for f-HOPG

U (mV)	R_s (Ohm)	R_{ct} (Ohm)	C_{EDL} (μF/cm²)
-500	19.24	12080	5.12
-450	19.16	13980	5.024
-400	19.15	16190	4.932
-350	19.15	19180	4.862
-300	19.12	24070	4.792
-250	19.11	32030	4.722
-200	19.11	42530	4.69
-150	19.09	53050	4.704
-100	19.07	59360	4.75
-50	19.1	59190	4.812
0	19.08	49440	4.884
50	19.06	36590	4.96
100	18.98	32720	4.996
150	18.88	47070	5.006
200	18.76	56700	5.084
250	18.67	63730	5.192
300	18.63	66930	5.324
350	18.6	60360	5.514
400	18.53	57770	5.696
450	18.48	53020	5.924

Table 4.3 Fitting results calculated from the impedance spectra for a-HOPG.

Same experiments were performed to record impedance spectra on both f-HOPG and a-HOPG with U changing in a reverse direction. For f-HOPG, impedance spectra were recorded while U increasing from -300 mV to -50 mV, then decreasing to -500 mV and increased back to -300 mV. For a-HOPG, impedance spectra were recorded with U decreasing from 450 mV to -500 mV. Same analysis was also done and then presented with the results mentioned above in the following section.

It is clear from table 4.2 and 4.3 that R_s is potential independent. Due to the limited space in the experimental setup, only about 100 μL electrolyte could be introduced to maintain the electrochemical condition. Although a wash bottle was applied to increase the humidity in the environmental hood (to keep the system in argon atmosphere),

solvent evaporation cannot be completely prevented, resulting in increasing electrolyte concentration with time passing by.

For f-HOPG, R_{ct} values are potential dependent (Figure 4.7). Within potential window between -500 mV and -200 mV, the relationship between R_{ct} and U is nearly linear, but between -200 mV and -50 mV, R_{ct} increases exponentially with increasing U . This result is in agreement with the CV curves (Figure 4.3 A1 and A2) that no significant current being observed between -200 mV and -50 mV and current density increase when potential being more negative than -250 mV.

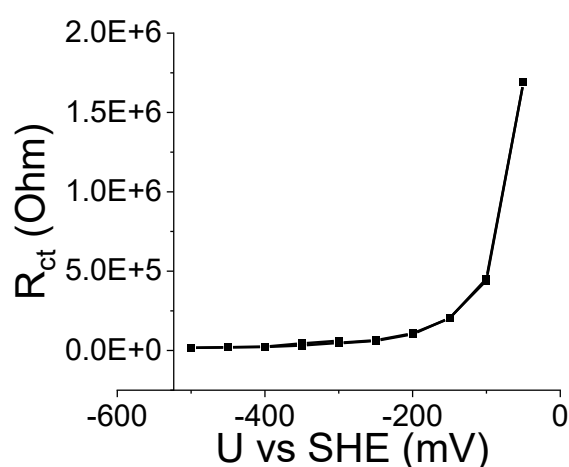


Figure 4.7 Potential Dependency of R_{ct} for f-HOPG electrode.

Compared to f-HOPG, the R_{ct} values for a-HPG are much smaller. The R_{ct} versus U curve (Figure 4.8) shows a distinctive peak around the redox potential (around 50 mV) observed from the CV of a-HOPG in 10 mM PBS (Figure 4.3 B).

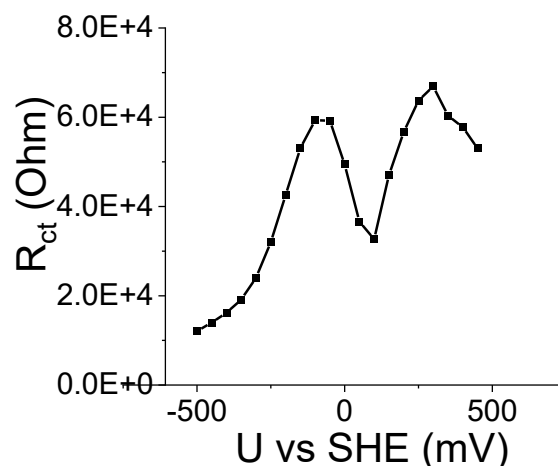


Figure 4.8 Potential Dependency of R_{ct} for a-HOPG electrode.

Figure 4.9 presents the best fitting C_{EDL} estimated from the impedance spectra in figure 4.4 and 4.5. As shown in the figure, the C_{EDL} vs U curves for both f-HOPG and a-HOPG show V-like shape, with similar minimum capacitance: $4.71 \mu\text{F}/\text{cm}^2$ for f-HOPG and $4.69 \mu\text{F}/\text{cm}^2$ for a-HOPG. While after annealing, the potential for the minimum C_{EDL} shifted from -0.3 V to -0.05 V . Considering the wings of the hyperbolic C_{EDL} vs U curves, although they are not strictly linear, the slopes for the wings were also calculated to have a rough idea of the dependence of C_{EDL} on substrate potential. For both samples, the absolute C_{EDL} changing rates on the positive side of the potential of minimum capacitance ($3.6 \mu\text{F cm}^{-2} \text{ V}^{-1}$ for f-HOPG and $1.27 \mu\text{F cm}^{-2} \text{ V}^{-1}$ for a-HOPG) are larger than that on the negative side ($-1.5 \mu\text{F cm}^{-2} \text{ V}^{-1}$ for f-HOPG and $-0.88 \mu\text{F cm}^{-2} \text{ V}^{-1}$ for a-HOPG). Comparing between the curves, the curves for f-HOPG are steeper than that of a-HOPG, meaning the substrate potential has stronger influence on the capacitance of EDL on the f-HOPG surface.

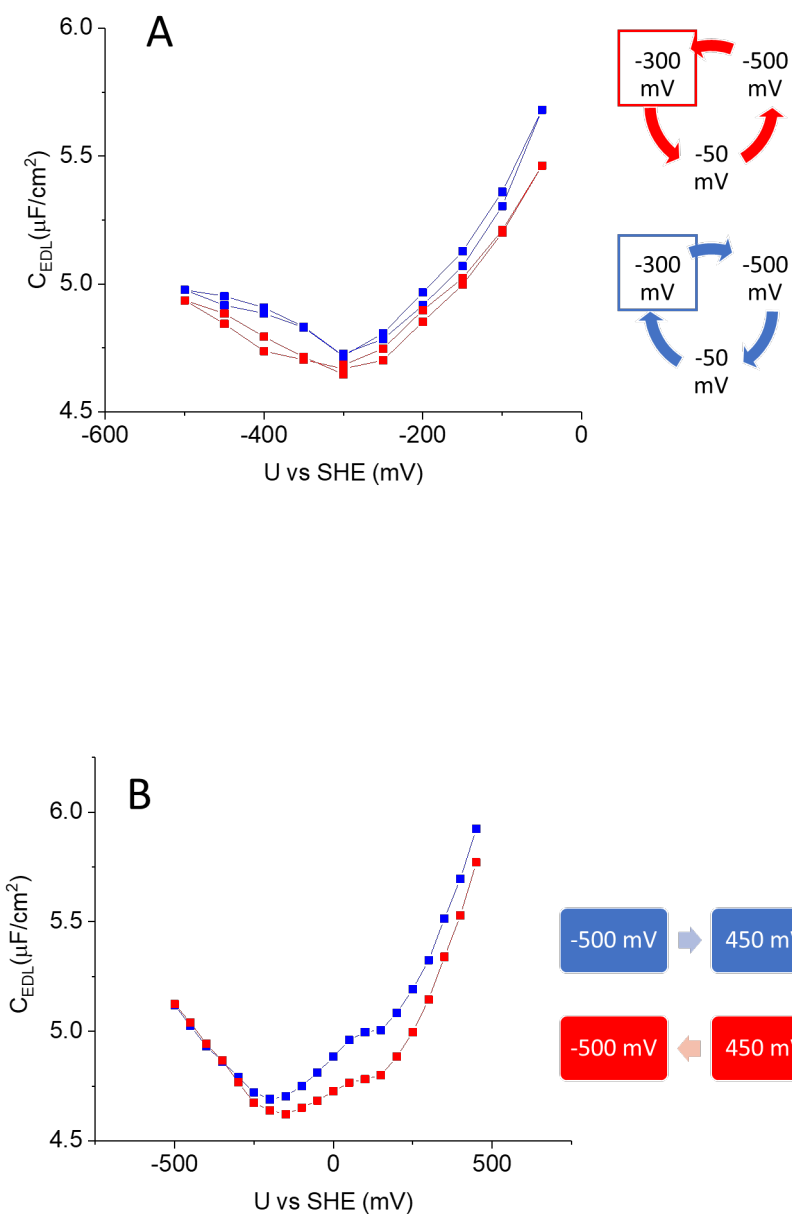


Figure 4.9 Potential dependency of C_{EDL} at (A): f-HOPG/PBS and (B): a-HOPG/PBS interfaces.

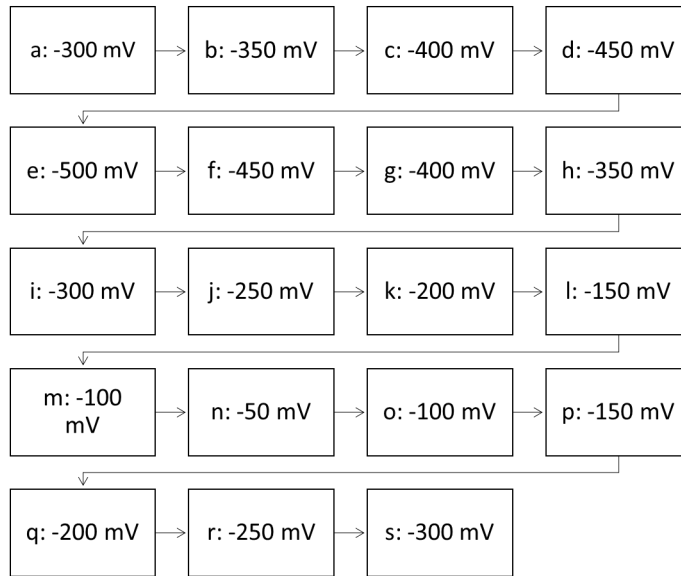
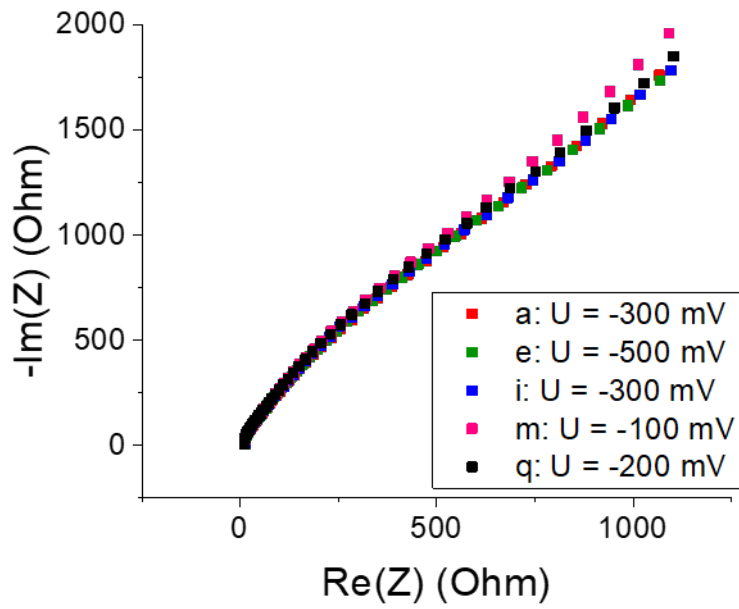
The potential dependent capacitance behaviour of carbon-based materials, including glassy carbon (Randin & Yeager, 1971), graphene (Pope et al., 2011) and carbon nanotubes (Wiggins-Camacho & Stevenson, 2009) has been widely investigated. Capacitance-potential curves have also been made for HOPG samples with different surface modification conditions: freshly cleaved, aged in air and in argon atmosphere, respectively (Zou et al., 2016). V-shape, nearly symmetrical capacitance-potential curves are observed for these HOPG samples, along with the positive direction shifting of potential for minimum capacitance after HOPG being aged in air and argon. This

result supports the research on capacitance potential dependency of HOPG samples before and after thermal treatment in this thesis.

The potential shifting of minimum capacitance indicates that after thermal treatment, the HOPG surface is n-doped, resulting in its flat band potential being shifted to a more positive value than that of the undoped f-HOPG (Ji et al., 2014). From the comparison between the CV curves of f-HOPG and a-HOPG in 10 mM PBS (pH 7.4), redox active components, probably oxygen containing functional groups, was introduced on to the HOPG surface and that could be one factor leading to the n-doping of the graphite material. Another possible factor could be the adsorption of oxygen and moisture adsorption on the HOPG surface. As mentioned in Chapter 3, HOPG sample was left in the oven to cool down for around 8h to around 50°C after being annealed at 650°C. It has been reported that a 0.5 V shift of potential for minimum capacitance was observed from the comparison within capacitance-potential curves of fresh HOPG, HOPG aged in air and in argon atmosphere (Zou et al., 2016). So the potential shifting could be caused by either the oxygen containing functional groups or the adsorbed oxygen and moisture, or both.

4.3.2 Annealed HOPG with HRP Adsorption: EIS Analysis

The HRP modified a-HOPG electrode was also studied by EIS to investigate the capacitance of HRP molecules. The experimental conditions were exactly the same as the EIS test on f-HOPG surface due to the similar electrochemical behaviour observed from the CV curves of f-HOPG and a-HOPG. The recorded impedance spectra are shown in figure 4.10. From the Nyquist diagrams (Figure 4.10 B), it is obvious that in comparison to the curves for f-HOPG and a-HOPG after HRP adsorption, the curves have significant lower $\text{Re}(Z)$ and $-\text{Im}(Z)$ values.

A**B**

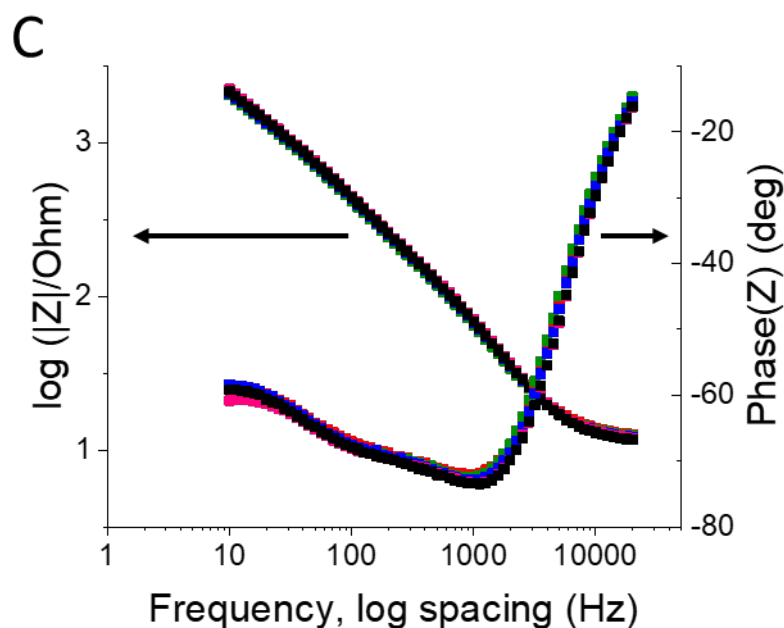


Figure 4.10 Impedance spectra recorded at HRP modified a-HOPG surface in 10 mM PBS. (A): Substrate potential changing pattern according to which the impedance spectra were recorded. (B): Nyquist plot. (C): Bode plot.

From these spectra, capacitance of the EDL at interface and of HRP molecules were calculated based on the equivalent circuits in figure 4.11. Three equivalent circuits were applied for capacity calculation, where R_s is the solution resistance, C_{EDL} is the EDL capacitance, R_{ct1} is the charge transfer resistance of the solid-liquid interface, C_{HRP} is the HRP molecular capacitance, R_{ct2} is the charge transfer resistance of adsorbed HRP molecules and W is the Warburg impedance. For Model B and C, a constant phase element Q_{HRP} could be introduced to replace C_{HRP} for possible better fitting values.

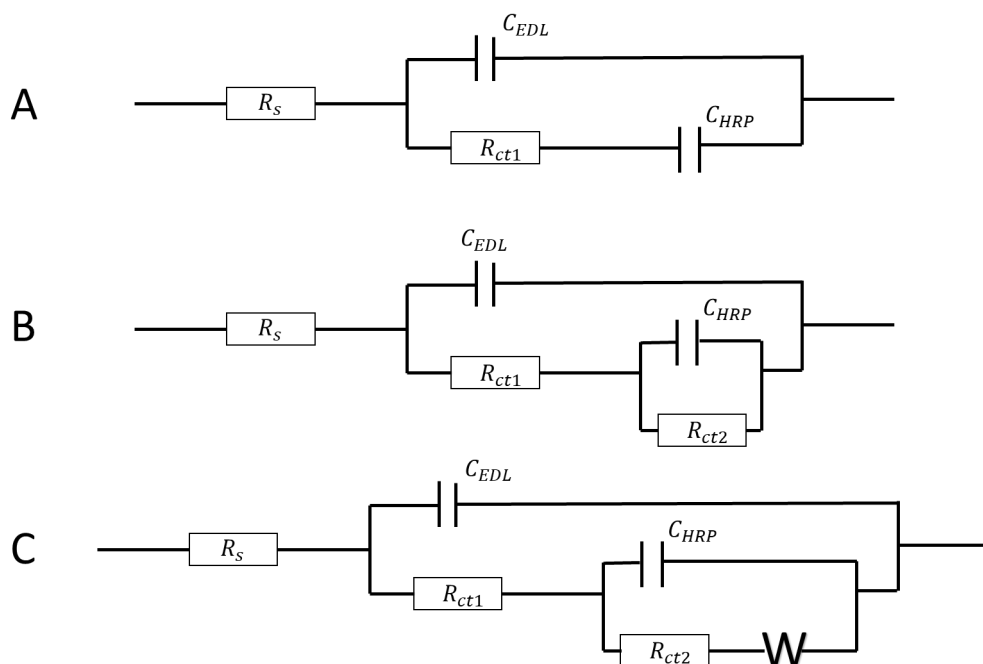


Figure 4.11 Equivalent circuit models for HRP modified a-HOPG surface (Sagara et al., 1990). For details see text.

The best fitting values for model A in figure 4.10 are listed in table 4.4. As can be seen from the data, R_s values show the same time dependency as those listed in table 4.2 and 4.3. Significant decrease in R_{ct1} is observed after HRP adsorption. For f-HOPG and a-HOPG, R_{ct1} could be as high as $10^6 \Omega$, while for HRP-HOPG system, R_{ct1} increased from 868.9Ω to 885.2Ω with U increasing from -500 mV to -50 mV .

The C_{EDL} values listed in table 4.4 were graphed versus the substrate potential (Figure 4.12). It is obvious that C_{EDL} of the HOPG-HRP system is also potential dependent. C_{EDL} decreased from $4.088 \mu\text{F}/\text{cm}^2$ to $3.716 \mu\text{F}/\text{cm}^2$ with substrate potential increasing from -500 mV to -50 mV . This potential dependency is in agreement with the previous EIS results of a-HOPG (Figure 4.5). Compared with the corresponding points in table 4.2, numerically speaking, C_{EDL} of the HOPG-HRP system shows an average decrease of $0.8 \mu\text{F}/\text{cm}^2$.

For an electrode immersed in aqueous solution, C_{EDL} can be calculated using the following equation:

$$C_{EDL} = \frac{\epsilon A}{d} \quad (4.1)$$

where ε is the relative permittivity, A is the electrode surface area and d is the double layer thickness. Thermal treatment to f-HOPG surface introduces surface defects, including pits on the basal plane and roughness at step edges (Figure 4.1), which are the ideal locations for HRP immobilisation. Since the roughness region provides large area for electrode surface, HRP molecules hindering these regions will lead to reduction of electrode surface area, resulting in the decrease of C_{EDL} .

Another possible explanation is, since C_{HRP} is much larger than C_{EDL} (Figure 4.4), charged ions in electrolyte would show the tendency to accumulate around the HRP molecules rather than at HOPG-PBS interface. The influence of HRP to the charge distribution within EDL may also contribute the decrease of C_{EDL} .

U (mV)	R_s (Ohm)	R_{ct1} (Ohm)	C_{EDL} ($\mu F/cm^2$)	C_{HRP} ($\mu F/cm^2$)
-300	33.37	889.8	3.89	33.6
-350	33.22	882.9	3.934	34.92
-400	33.06	877.2	3.98	35.44
-450	32.89	868.9	4.032	35.64
-500	32.75	864.1	4.088	35.88
-450	32.65	865.3	4.048	36.04
-400	32.5	864.8	3.996	35.94
-350	32.38	864.4	3.954	35.58
-300	32.29	866.3	3.908	34.32
-250	32.18	872.3	3.85	32.62
-200	32.07	876.6	3.794	31.06
-150	32	879.2	3.76	30.26
-100	31.89	881.7	3.73	29.68
-50	31.74	885.2	3.716	29.06
-100	31.61	875	3.738	29.84
-150	31.49	869	3.766	30.42
-200	31.4	862.8	3.804	31.3
-250	31.32	856.8	3.858	32.76
-300	31.16	851.5	3.92	34.22

Table 4.4 Fitting results calculated from the impedance spectra for HRP modified a-HOPG, based on model A in figure 4.11.

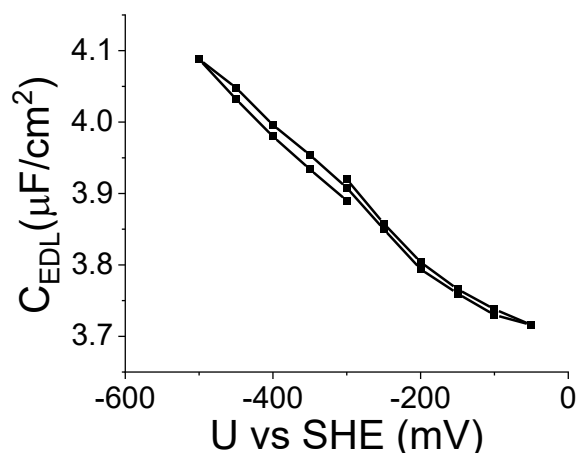


Figure 4.12 Potential dependency of C_{EDL} at HRP modified a-HOPG/PBS interface. C_{EDL} values calculated using model A in figure 4.11.

C_{HRP} was also calculated and graphed with reference to the substrate potential U (Figure 4.13 A). The values of C_{HRP} are about 9 times higher than those for C_{EDL} , ranging from $29.06 \mu\text{F}/\text{cm}^2$ ($U = -50 \text{ mV}$) to $39.06 \mu\text{F}/\text{cm}^2$ ($U = -450 \text{ mV}$). Instead of the relatively linear relationship between C_{EDL} and U , the potential dependency of C_{HRP} could be separated into three phases. In phase one, when U was between -50 mV and -200 mV , C_{HRP} increased slowly from $29.06 \mu\text{F}/\text{cm}^2$ to $31.06 \mu\text{F}/\text{cm}^2$ with decreasing potential. A sharp increase was observed in phase two (U decreasing from -200 mV to -400 mV), where C_{HRP} increased from $31.06 \mu\text{F}/\text{cm}^2$ to $35.94 \mu\text{F}/\text{cm}^2$. In phase three, where U was on the negative side of -400 mV , C_{HRP} stayed constant, even decreased a little bit when U was -500 mV . To have a more intuitionistic idea of the HRP capacitance potential dependency, the changing rate of C_{EDL} , dC_{EDL}/dU was calculated and graphed versus U (Figure 4.13 B). The dC_{EDL}/dU vs U curve shows a parabolic shape and peaks at -300 mV , which is also the potential where the sudden current density decrease is observed from the CV curves of HRP modified a-HOPG electrode.

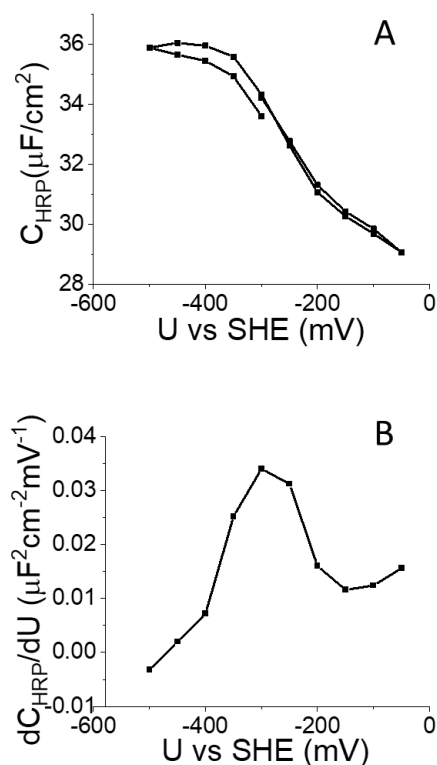


Figure 4.13 Potential dependency of (A) HRP capacitance and (B) HRP capacitance variation rate.

Although no redox peaks are observed from the CV curves of HRP modified a-HOPG, an element R_{ct2} is included in model B to evaluate the contribution of possible redox reactions of HRP. The best fitting values calculated using model B in figure 4.11 are listed in table 4.5. Comparing with the corresponding values in table 4.4, R_s and C_{EDL} show negligible difference and R_{ct1} values are averagely 18% lower. C_{HRP} values are obviously lower (the difference is also listed in table 4.5), and the decrease shows potential dependency that more negative substrate potential leads to more value decrease. Despite the difference in values, C_{HRP} calculated using Model B shows similar potential dependency as that calculated using Model A. The newly introduced element, charge transfer resistance of HRP molecules, R_{ct2} , varies from 1101 Ω ($U = -0.4$ V) to 1511 Ω ($U = -0.05$ V). Despite the differences between the values, all the elements listed in table 4.5 show similar potential dependency as their corresponding ones listed in table 4.4.

U (mV)	R _s (Ohm)	R _{ct1} (Ohm)	R _{ct2} (Ohm)	C _{EDL} (μF/ cm ²)	C _{HRP} (μF/ cm ²)
-300	32.95	727.2	1208	3.818	24
-350	32.82	718.4	1137	3.858	24.38
-400	32.68	714.8	1122	3.904	24.74
-450	32.51	708.3	1121	3.954	24.96
-500	32.36	703.2	1111	4.008	25.08
-450	32.25	704.4	1102	3.968	25.1
-400	32.1	703.7	1101	3.916	24.98
-350	32	707	1127	3.878	25.1
-300	31.9	711.3	1193	3.836	24.76
-250	31.78	720.8	1297	3.782	24.24
-200	31.66	728.6	1407	3.732	23.72
-150	31.58	732.2	1468	3.7	23.36
-100	31.47	732.2	1488	3.668	22.9
-50	31.32	732.1	1511	3.652	22.4
-100	31.2	729.2	1496	3.678	23.2
-150	31.08	726.7	1478	3.708	23.72
-200	30.99	721.7	1428	3.744	24.26
-250	30.9	714.4	1332	3.794	24.92
-300	30.76	703.1	1224	3.848	25.16

Table 4.5 Fitting results calculated from the impedance spectra for HRP modified a-HOPG, based on Model B in figure 4.11.

Another possibility that HRP may not behave like a perfect capacitor was also considered and modelled by Model B using a constant phase element (Q) to replace C_{HRP}. The best fitting values are listed in table 4.6. After the CPE substitution, there is a 40% to 50% decrease in the values of R_{ct1} and around 9.3% decrease in the values of C_{EDL}. HRP capacitance could be calculated using the following equation:

$$C^n = \frac{Q}{R^{n-1}} \quad (4.2)$$

where C is the capacitance (C_{HRP} in this case), R is the charge transfer resistance in parallel to Q (R_{ct2} in this case) and n is the constant phase (-90*n)^o, a number between

0 and 1. CPE represents an ideal capacitor when n is 1 and an ideal resistor when n is 0.

In table 4.6, n is between 0.4042 ($U = -400$ mV) and 0.4934 ($U = -100$ mV), suggesting non-ideal capacitor behaviour of the adsorbed HRP molecules. But in the meantime, R_{ct2} values are much larger than the ones of R_{ct1} , indicating almost no current flowing through this branch. In this case, this model could be replaced by model A.

U (mV)	R_s (Ohm)	R_{ct1} (Ohm)	R_{ct2} (Ohm)	C_{EDL} ($\mu F/cm^2$)	Q ($S \cdot s^n$)	n
-300	32.23	390.2	4.88E+10	3.578	1.64E-04	0.4258
-350	32.15	372.3	3.87E+10	3.61	1.77E-04	0.4109
-400	32.04	370.1	2.68E+12	3.652	1.80E-04	0.4094
-450	31.88	369.5	5.73E+12	3.7	1.80E-04	0.4121
-500	31.74	359.3	7.31E+12	3.746	1.83E-04	0.4081
-450	31.62	359.5	3.02E+12	3.708	1.85E-04	0.406
-400	31.48	356.2	1.69E+12	3.656	1.85E-04	0.4042
-350	31.38	365	2.18E+10	3.622	1.80E-04	0.4107
-300	31.27	383.3	6.08E+10	3.59	1.67E-04	0.4276
-250	31.13	411	6.42E+11	3.552	1.48E-04	0.4521
-200	30.99	435.3	2.96E+11	3.512	1.32E-04	0.4755
-150	30.9	444.8	1.55E+15	3.486	1.24E-04	0.486
-100	30.79	444.3	4.61E+11	3.456	1.21E-04	0.4883
-50	30.65	445.9	4.68E+12	3.442	1.17E-04	0.4926
-100	30.54	448.2	8.86E+19	3.466	1.20E-04	0.4934
-150	30.43	447.9	1.32E+13	3.494	1.23E-04	0.4922
-200	30.34	440.3	1.13E+12	3.526	1.29E-04	0.4845
-250	30.25	419.6	2.17E+12	3.564	1.43E-04	0.4643
-300	30.12	381.4	3.58E+13	3.594	1.63E-04	0.4344

Table 4.6 Fitting results calculated from the impedance spectra for HRP modified a-HOPG, based on Model B, with C_{HRP} substituted by Q in figure 4.11.

Model C takes the influence of mass transfer into consideration by introducing a Warburg element into the equivalent circuit. This model is usually applied when the adsorption-desorption kinetics and the rate of charge transfer of the adsorbate species are in the same order of magnitude. This will be described and discussed in chapter 5 with the images of HRP molecules on HOPG surfaces captured by EC-SPM techniques over a relatively long timespan.

4.3.3 Annealed HOPG with HRP Adsorption: MOS Approximation

From the impedance spectra, double layer capacitance and HRP capacitance at a-HOPG/PBS interface were calculated using equivalent circuits that can describe the electrode interface properties. As can be seen from figure 4.11, depending on different interactions between the adsorbate enzyme molecules and the electrode surface, different equivalent circuits could be used for EIS analysis.

From the CV curves for HRP modified a-HOPG surface in PBS, no redox peaks are observed, suggesting no electron transfer reactions at the interface. Therefore, model B, which takes the adsorbate enzyme redox reaction into account by adding a charge transfer resistance in parallel with HRP capacitance, could not describe the situation. Even if there were redox reactions in the system that being too weak to be observed from the CV curves, the HRP capacitance calculated using model B still shows the same potential dependency as that calculated using model A.

The capacitance potential dependency of HRP shown in figure 4.13 A shows the typical characteristic of a p-type metal oxide semiconductor (MOS) capacitor (Figure 4.14). As can be seen from CV curves for HRP modified a-HOPG surface (Figure 4.3 C1 and C2), when the substrate potential U is between -350 mV to -500 mV versus SHE, charge current is observed, suggesting charge accumulation on HRP molecules. This potential range, from -500 mV to -350 mV, corresponds to the accumulation region in the operation of a p-type MOS capacitor, in which holes will accumulate at the insulator-semiconductor interface, resulting in the enhanced surface conductivity. For HRP molecules on HOPG surface, when U is between -250 mV and -50 mV, no obvious charging current density could be observed from the CV curves. This U range corresponds to the depletion region, in which acceptor density will increase at the insulator-semiconductor interface, but still being smaller than the hole density. The

dC/dU vs U curve for HRP adsorbed on HOPG surface peaks at -300 mV (Figure 4.13 B). For a MOS capacitor, at this potential, which is also termed as flat band potential since at this potential there is no energy band bending, the semiconductor layer is charge neutral everywhere due to the hole density being balanced by the acceptor density. There is no potential drop in the semiconductor layer at flat band potential.

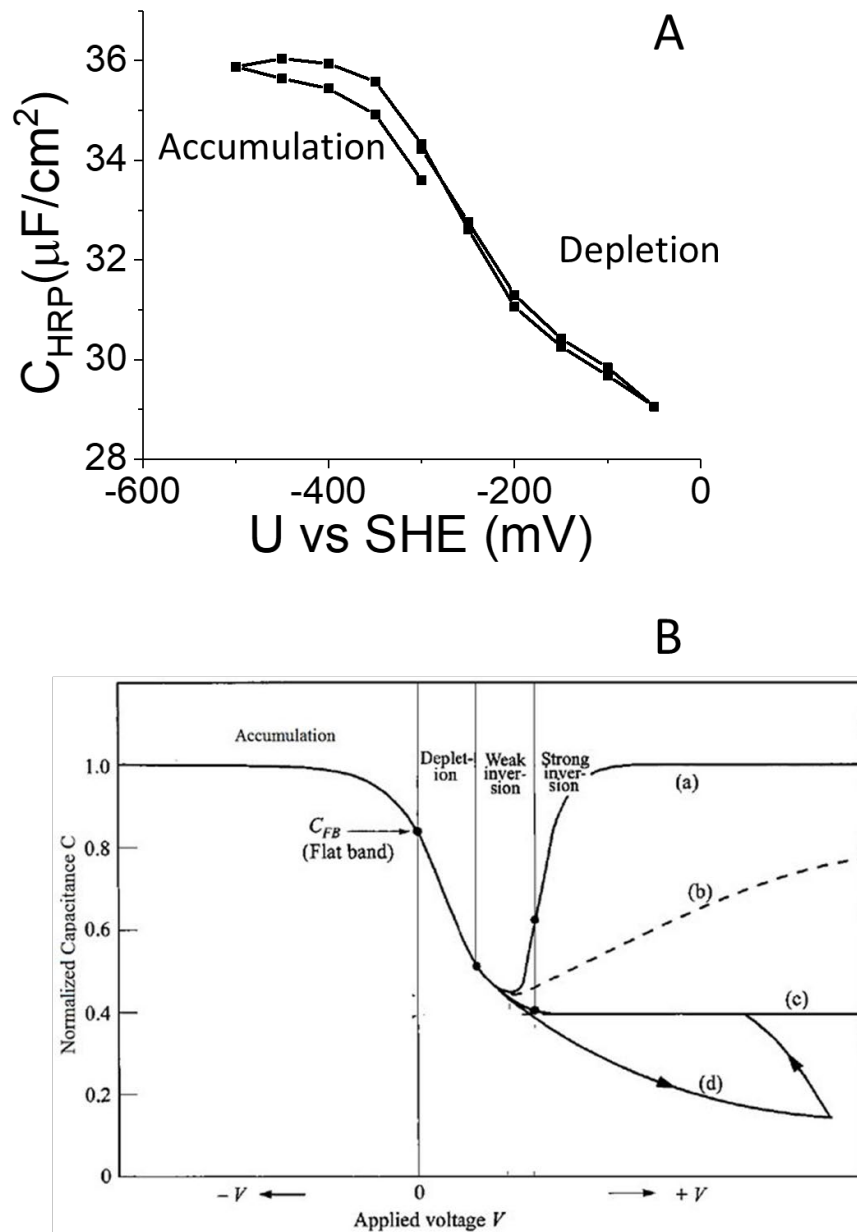


Figure 4.14 (A) Capacitance-potential curve for C_{HRP} measured at HRP modified a-HOPG surface. (B) Typical capacitance-potential curve for a p-type MOS capacitor ('MOSFETs', 2006). (a) Low frequency, (b) Intermediate frequency, (c) High frequency, (d) High frequency and fast sweep rate (going into deep depletion).

An HRP molecule consists of a polypeptide chain (forming the tertiary structure) and an iron ion containing active centre (heme group) and two calcium ions. It has been reported that peptide chains could behave like semiconductor material through highly ordered and directional intermolecular π - π interactions and hydrogen-bonding network (Tao et al., 2017). This property raises the possibility that HRP molecules could act as a semiconductor layer, constitutes a MOS capacitor together with the annealed HOPG electrode, with the annealed top layer of HOPG as the oxide layer and the HOPG beneath as the metal layer. (Figure 4.15).

A: Annealed HOPG with HRP Immobilised on the Surface

B: Metal-Oxide-Semiconductor Capacitor

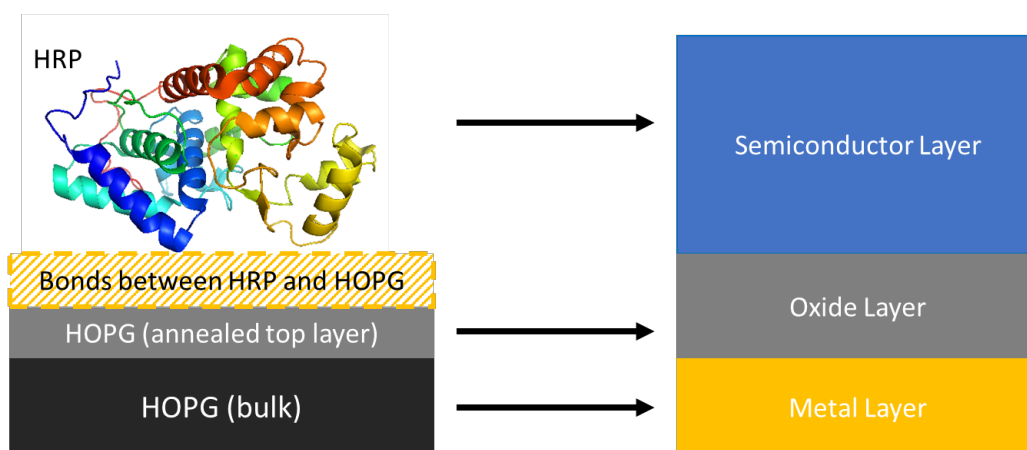


Figure 4.15 Metal-Oxide-Semiconductor (MOS) capacitor approximation. 3D plot of HRP structure was plotted with PyMOL(DeLano, 2002), with the accession code 1w4w from PDB(Carlsson et al., 2005).

Since the EIS measurement of HRP modified a-HOPG surface was performed with the potential range between -500 mV and -50 V vs SHE, no inversion region can be observed from the capacitance-potential curve. Further investigations could be helpful to study the electrochemical behaviour of HRP within a wider potential window to gain a more comprehensive understanding of the potential dependency of HRP capacitance.

4.3.4 HRP-catalysed Oxygen Reduction Reactions

Although as mentioned in section 1.4 that it is difficult to have direct electron transfer between the electrode materials and the HRP molecules immobilised on their surfaces without the presence of hydrogen peroxide, a mechanism of HRP catalysing the reduction of oxygen under electrochemical condition is proposed (Figure 4.16).

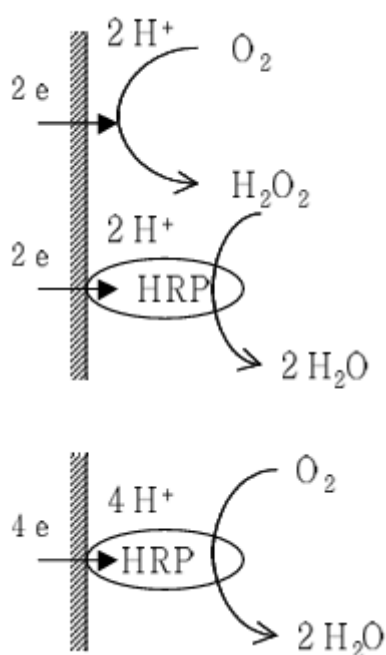


Figure 4.16 Mechanism of HRP-catalysed oxygen reduction reaction(Bergel & Lai, 2001).

Bergel and Lai proposed the mechanism to be HRP-catalysed electrochemical reduction of oxygen, however, it is also clearly mentioned in the publication that hydrogen peroxide comes from the direct electrochemical reduction of oxygen on the electrode, in which process HRP plays no role. But one point worth noticing from their work is due to the oxygen reduction and the following HRP-catalysed hydrogen peroxide reduction reactions, a current increase is observed from the CV at the most negative potential values, and that matches the observation in this work (Figure 4.3). Therefore, it would be arbitrary to attribute the current increase at negative condition to charging without considering the possibility of it being redox current.

During the experiments, methods, including using environmental control hood (Figure 3.6) to maintain an argon atmosphere and using argon-saturated electrolyte, has been taken to minimise the oxygen content within the system. But it is technically impossible to have an oxygen-free system using the current setup. Due to the setup limitations, such as imperfect sealing between the environmental control hood and the base of the SPM instrument, oxygen permeating through the argon supplying pipe, and even the trace amount of oxygen existing in the argon source, there could be very little amount of oxygen in the system, in the atmosphere or the electrolyte or both, that may lead to the current increase observed in the CV spectra (Figure 4.3).

The oxidation reduction reaction in aqueous environment is pH dependent. In alkaline media, the reaction pathways and the corresponding thermodynamic potentials at standard conditions (E^0) versus SHE are expressed as the following (Roquet et al., 1994):



While in acidic media, the pathways and thermodynamic potentials are (Wroblowa et al., 1976):



In this work, the electrolyte used was PBS (pH = 7.4), providing a slightly alkaline and nearly neutral environment. It has been reported that in neutral aqueous environment (3.5% NaCl solution), oxygen reduction (generating hydrogen peroxide) can be observed only in oxygen-saturated solutions at around 0.23V versus SHE. And in nitrogen-saturated solutions, there are no oxygen reduction reactions can be observed (Wu et al., 2011).

The impedance spectra of HRP immobilised annealed HOPG electrode were recorded using argon-saturated PBS within the potential window between -500 mV and -50 mV. Comparing to oxygen-saturated solutions, even if the experimental environment is not completely oxygen free, the oxygen content in the PBS used can still be regarded as

neglectable. And the most positive potential applied for impedance spectra recording is -0.05 V, which is not positive enough for oxygen reduction reaction in the oxygen-saturated solutions. To draw a conclusion, there should be no redox reactions involving oxygen reduction and hydrogen peroxidase decomposition catalysed by HRP in this system. Therefore, the current increase observed from the CV curves in figure 4.3 should result from charge accumulating on HRP molecules.

4.4 Conclusions

The potential dependency of the capacitance of HRP molecules immobilised on annealed HOPG surface was studied using EIS. It showed that the capacitance of HRP exhibits similar potential dependency as that of a MOS capacitor with a p-type semiconductor layer. Both the accumulation region and the depletion region are observed from the capacitance-potential curve of HRP molecules. Future experiments on measuring the capacitance of HRP when the potential being more positive than -50 mV could be performed to determine the inversion region. The ideal case is a threshold potential, where C_{HRP} reaches minimum could be identified and when potential becomes more positive, C_{HRP} increases due to electrons within HRP molecular structure replaces protons as charge carriers.

Based on the MOS capacitor approximation, the flat band potential of HRP molecules has been determined as the potential where the dC_{EDL}/dU vs U curve peaks (-300 mV). At the flat band potential, there should be no potential drop within the HRP molecular structure. The potential drop cannot be directly monitored by the integrated electrochemical characterisation methods, such as CV and EIS. Further investigation on monitoring the potential drop has been performed by EC-SPM techniques and will be presented in the next chapter.

This work provides a MOS approach to the description of HRP adsorbed on a-HOPG surface. Since redox enzymes draw great interest in the field of biosensors and bioelectronic nanodevices, this work could contribute to the development of these fields.

Chapter 5. Potential Dependent Imaging of Horseradish Peroxidase Molecules Using Electrochemical Scanning Probe Microscopy

HRP molecules adsorbed on HOPG surfaces has been imaged by several SPM techniques at single molecular level, including ex-situ STM (WANG et al., 2000), in-situ STM and SECPM (Baier & Stimming, 2009). Potential dependent electrochemical behaviours of enzymes, like glucose oxidase (Wang et al., 2008b), were investigated using EC-STM technique. As mentioned in previous sections, potential dependency of the capacitance of HRP molecules at a-HOPG/PBS is observed through analysing the impedance spectra. Here, SECPM has been applied to directly monitor the charge distribution at HOPG-PBS and HRP-PBS interfaces, as supporting information for the MOS analogy to describe the potential dependent capacitance behaviour of HRP molecules under electrochemical conditions. EC-STM was also used to as a comparison and indirectly monitoring of the charge distribution.

5.1 SECPM Imaging Single HRP Molecules on Annealed HOPG Surface

5.1.1 Experimental Details

SECPM was performed in constant potential mode to image HRP molecules adsorbed on a-HOPG surface in 10 mM PBS. To make the experimental conditions as close as possible to that for EIS measurement, substrate potential (U) was changed in the mode shown in figure 4.10 A. Other than varying substrate potentials, parameters used for SECPM imaging are listed in table 5.1.

Potential setpoint	20 mV
Integral gain	1
Proportional gain	5
Tip velocity	0.3 $\mu\text{m/s}$
Points per line	512
Scanner	J (scan range: 125 μm * 125 μm)

Table 5.1 Parameter setup for SECPM imaging HRP modified a-HOPG in 10 mM PBS.

Potential setpoint determines the distance between tip apex and substrate surface. Larger potential setpoint results in larger distance between tip and surface. Smaller tip-substrate separation offers better resolution but will also increase the possibility that the relative movement between tip and substrate surface introducing disturbance to surface topological structure or HRP adsorption (molecules swept away by the tip). The potential setpoint, 20 mV, was chosen as a compromise that the tip-substrate separation is large enough to minimise the influence on HRP adsorption and small enough to avoid sacrificing image resolution.

The combination of tip velocity and points per line determines the time required to capture one image. Slower tip velocity and higher points per line lead to better imaging quality but longer time for image capturing. For the combination used in this work (tip velocity = 0.3 $\mu\text{m/s}$, points per line = 512 for image size 100 nm * 100 nm), it will take 4 minutes 21 seconds to capture a single image. At least 19 images are required to perform the analysis and it would usually take at least 1 hour to find a perfect location with single molecules steadily sitting on the surface. As mentioned in Chapter 3, due to the limited space in the experimental setup, only 100 μL electrolyte was used and the electrolyte environment can last no longer than 3 hours before the ring-shape CE being exposed caused by electrolyte evaporation. This tip velocity and points per line combination is also a compromise between image quality and experimental limitation.

5.1.2 SECPM Imaging HRP Molecules at Single Molecular Level

Figure 5.1 shows images captured by SECPM of HRP modified a-HOPG surface at varying substrate potentials. Three single HRP molecules sitting close to the step edge are observed from all the images. The three HRP molecules show similar hemisphere structure with possible elongation to the same direction (pointing to the top left corner) in some of the images. This could be caused by the scanning direction that probe moving from bottom to top and left to right with reference to the substrate.

Measurements of the height, diameter, area of the imaged HRP molecules were performed. As can be seen from the SECPM images, no obvious contrast change could be observed with changing U and this is reflected from height versus potential curves (Figure 5.2). For HRP 1 and 3 (Figure 5.1 A), the heights vary between 0.75

nm ($U = -500$ mV for HRP 1 and $U = -400$ mV for HRP 3) and 1.05 nm ($U = -100$ mV for HRP 1 and $U = -300$ mV for HRP 3). For HRP 2, height variation is between 0.53 nm ($U = -300$ mV) and 0.95 nm ($U = -0250$ mV). Although there is no obvious potential dependency of the apparent height, larger height values are usually observed when the potential is around -300 mV for all the three HRP molecules (only exception is HRP 1 at $U = -100$ mV).

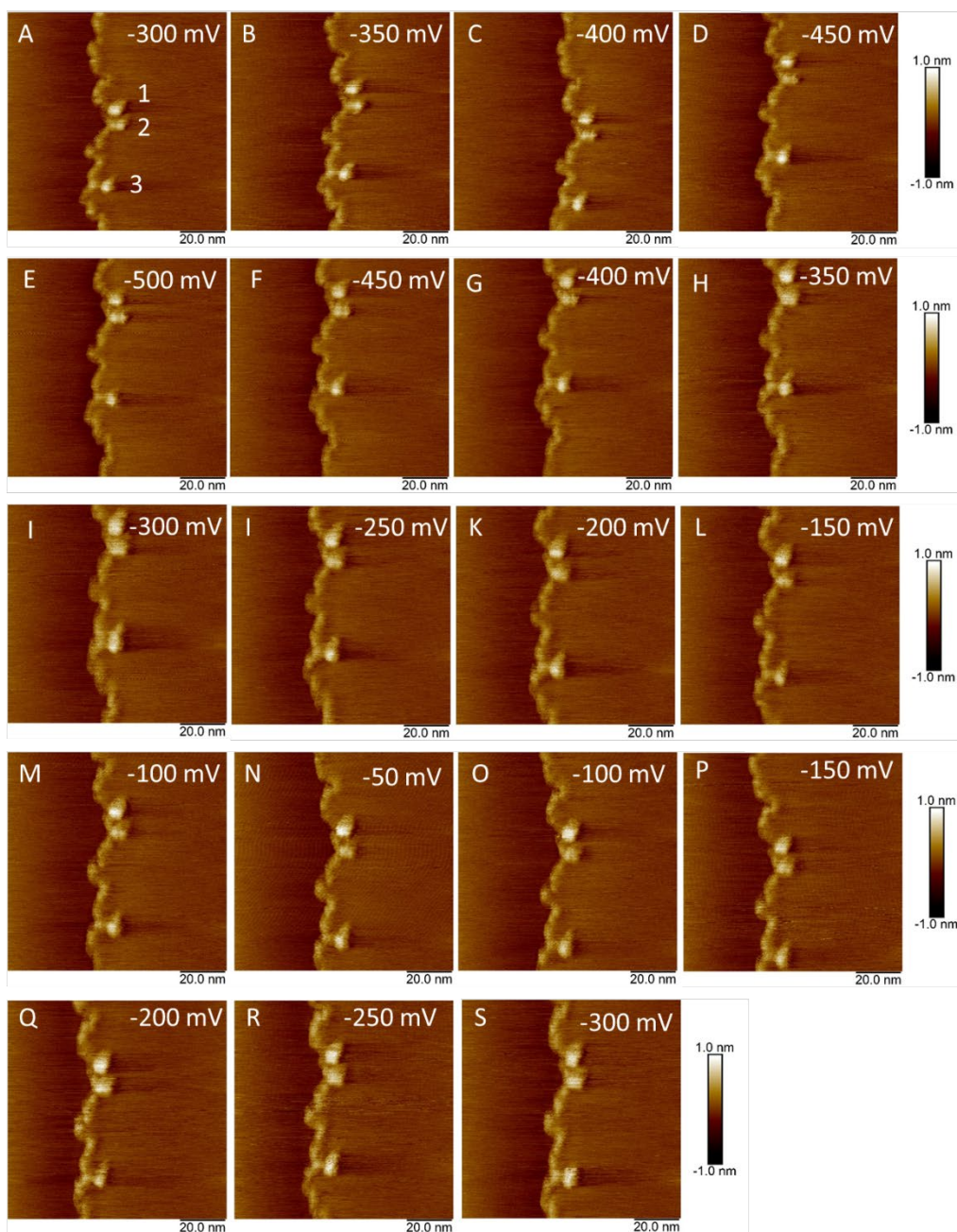


Figure 5.1 Series of SECPM images of HRP modified a-HOPG in 10 mM PBS (pH 7.4). Images were captured alphabetically as marked on the top left corner on each image at potentials as marked on the top right corner.

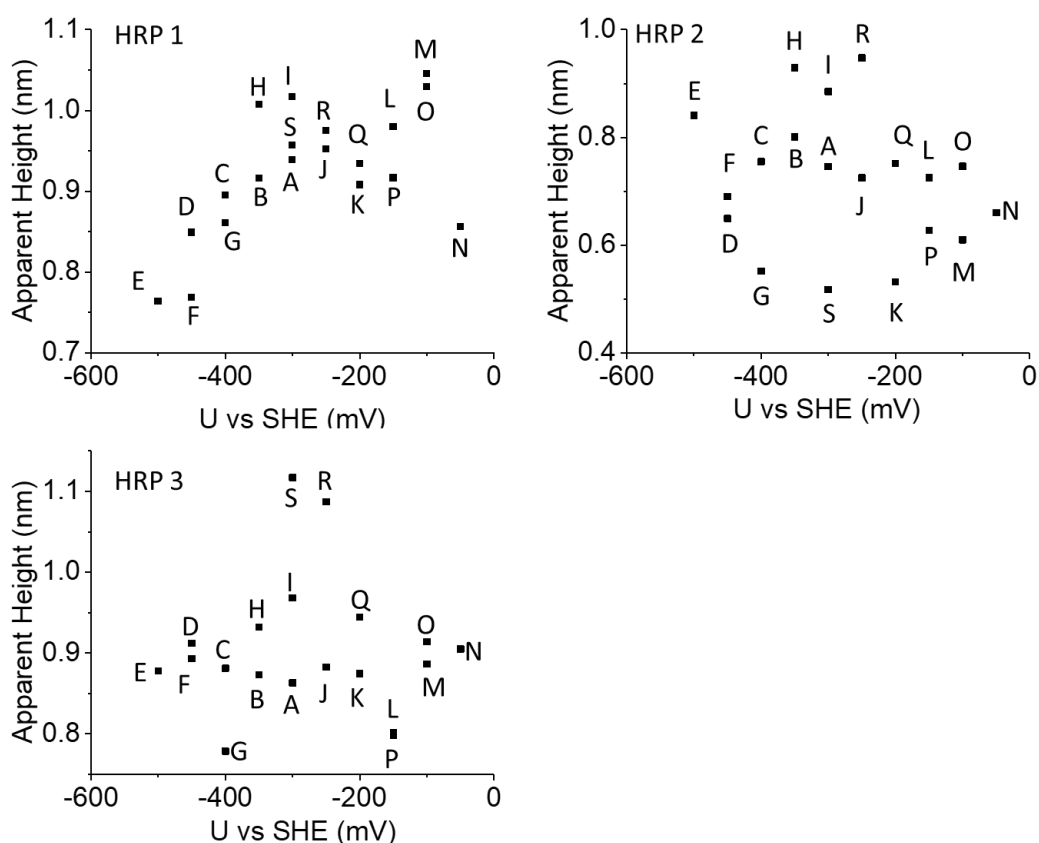


Figure 5.2 Potential dependency of HRP molecular apparent height from images of HRP modified a-HOPG surface by SECPM in 10 mM PBS (pH 7.4). HRP 1, 2 and 3 corresponding to the number in figure 5.1 A.

Diameter and area were taken from the particle analysis data (Figure 5.3) in two ways: with and without the elongated part. Volume of the molecules were calculated as the product of area and height, assuming HRP molecules as rods. As the analysis of height variation, diameter, area, and volume are graphed versus substrate potential (Figure 5.4, 5.5 and 5.6). In these figures, data with and without considering the elongated part are presented for comparison.

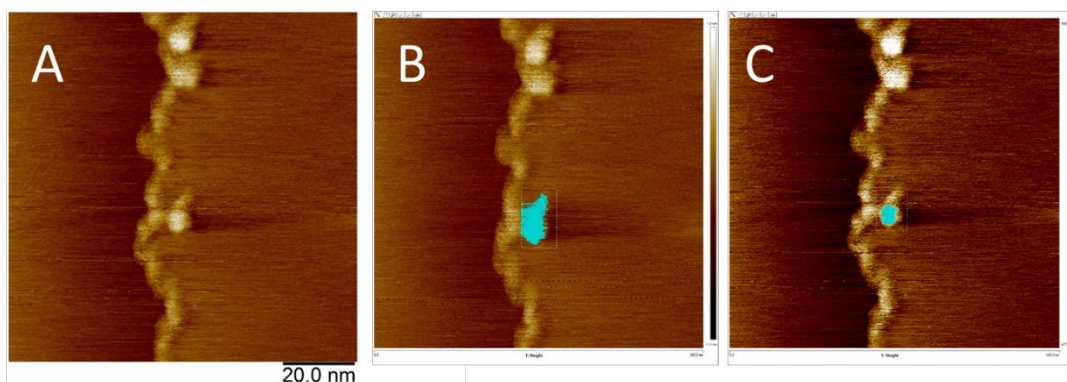


Figure 5.3 Software measurement of HRP molecular area and diameter. (A): the original image; (B): area and diameter measurement using the particle analysis function with the elongated part included; (C): measurement refining to exclude the elongated part.

Figure 5.4 shows the potential dependency of apparent area of the three HRP molecules. Trending lines (red lines in Figure 5.4, 5.5 and 5.6) were added manually to show an approximate tendency of HRP apparent size measured from SECPM images being potential dependent. Before excluding the influence of elongated part (Figure 5.4 a1, b1 and c1), the area variation could be divided into three phases. In phase 1, during which U decreasing from -300 mV to -500 mV (from point A to point E in all graphs), the apparent area values stay relatively constant. The maximum area difference is 7 nm² and it is observed between point D ($U = -450$ mV, area = 41 nm²) and C ($U = -400$ mV, area = 34 nm²) in figure 5.4 c1, the graph for HRP 3. Phase 2 is between point E ($U = -500$ mV) and N ($U = -50$ mV). In phase 2, the area vs potential curves of all the three HRP molecules peak at point I ($U = -300$ mV). For all the three molecules, the apparent area variation between point E and I is larger than that between point N and E, and the differences are listed in table 4.8. Phase 3 represents the process between point N and S, during which substrate potential decreasing from -50 mV to -300 mV. In phase 3, the potential dependency of apparent area is similar to that shown between point N and I (part of phase 2 when substrate potential is on the positive side of -300 mV).

After excluding the elongated part of each molecule, averagely around $1/3$ of apparent area decrease is observed for HRP 1 and 3, while $1/5$ of apparent area decrease for HRP 2. At potentials more negative than 300 mV, after comparing the apparent area values for the same molecule measured from images captured at the same potential

(A and I, B and H, C and G, D and F), significant differences could be observed for HRP 1 and 2 (Figure 5.4 a2 and b2), but not for HRP 3 (Figure 5.4 c2). At potentials more positive than -0.3 V, the differences mentioned above are much less significant. The exceptions occur between points J and R at -250 mV, and A, I and S at -300 mV on the curve for HRP 3 (Figure 5.4 c2). The apparent area values of HRP 3 measured from images R and S are much larger than those from other images.

Another feature observed from phase 2 for all the three HRP molecules is, before excluding the contribution of the elongated part of each molecule (Figure 5.4 a1, b1 and c1), the apparent area values measured at potentials more positive than -300 mV (J, K, L M and N) are generally larger than those measured at potentials on the negative side of -300 mV (H, G, F and E). After excluding the elongated part, the differences are less notable, indicating a relatively homogeneous influence on the apparent area decrease from potential shifting away from -300 mV, to both positive and negative directions.

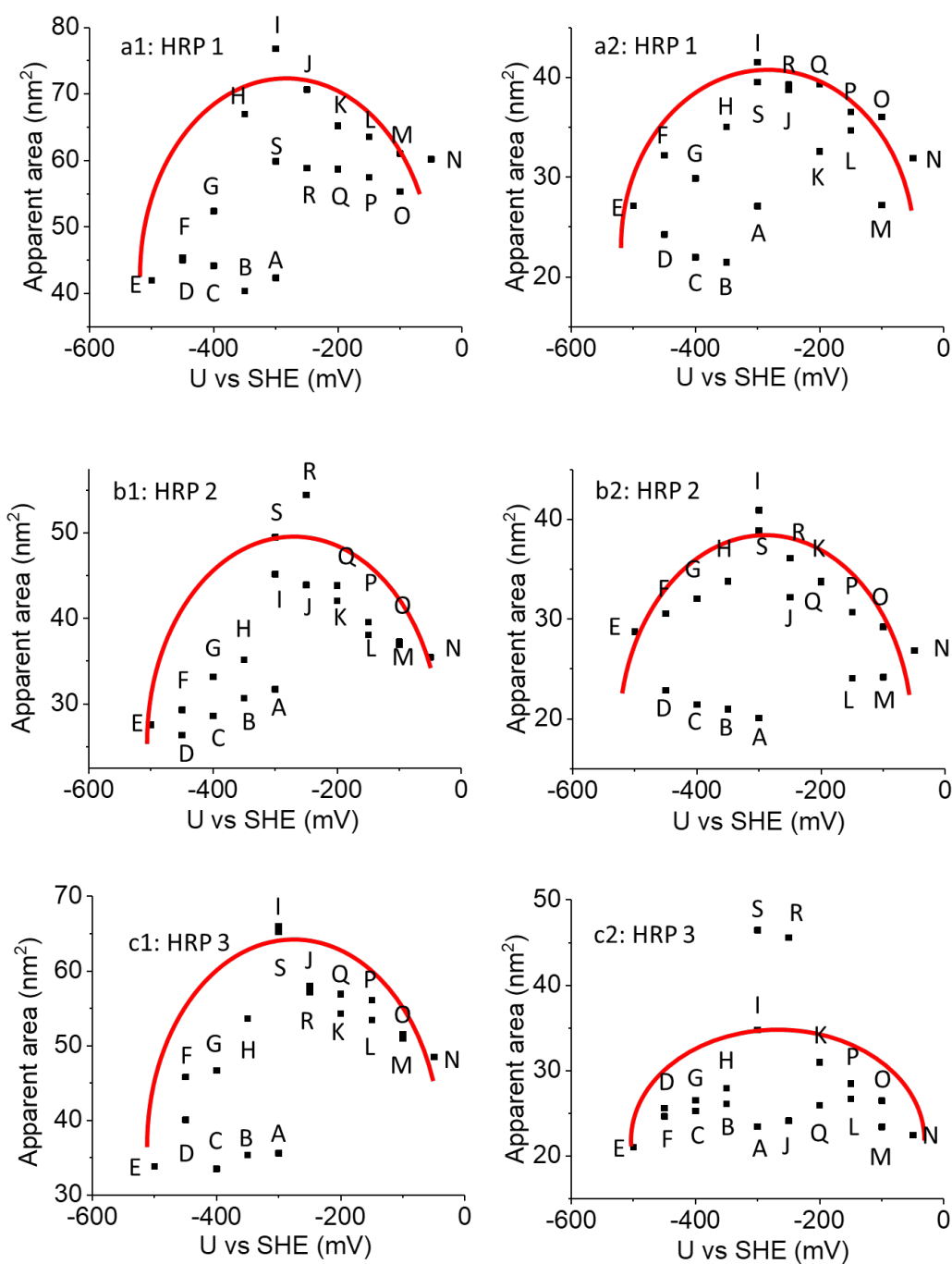


Figure 5.4 Potential dependency of HRP molecular apparent area measured from images of HRP modified a-HOPG surface by SECPM in 10 mM PBS (pH 7.4). HRP 1, 2 and 3 corresponds to the number in figure 5.1 A, with elongated part included in (a1), (b1) and (c1), excluded in (a2), (b2) and (c2). The red curves show a qualitative potential dependency of HRP apparent area.

Figure 5.5 shows curves of measured apparent diameter of the HRP molecules versus U. The apparent diameter is clearly also potential dependent. In all images, with the elongated part taken into measurement, the diameter values of HRP 1 and 3 (Figure 5.5 a1 and c) are larger than that of HRP 2 (Figure 5.5 b1). For HRP 1 and 3, diameter values vary between 6.5 nm and 10 nm, while for HRP 2, it varies between 5.8 nm and 8.4 nm. After excluding the elongated part, apparent diameter variations of all the three HRP molecules are in the range between 5 nm and 7.7 nm (Figure 5.5 a2, b2 and c2).

Diameters of the molecules are also measured using the function used for area measurement (particle analysis in Figure 5.3), so they show the similar potential dependency as the measured apparent area, which has been described above in detail.

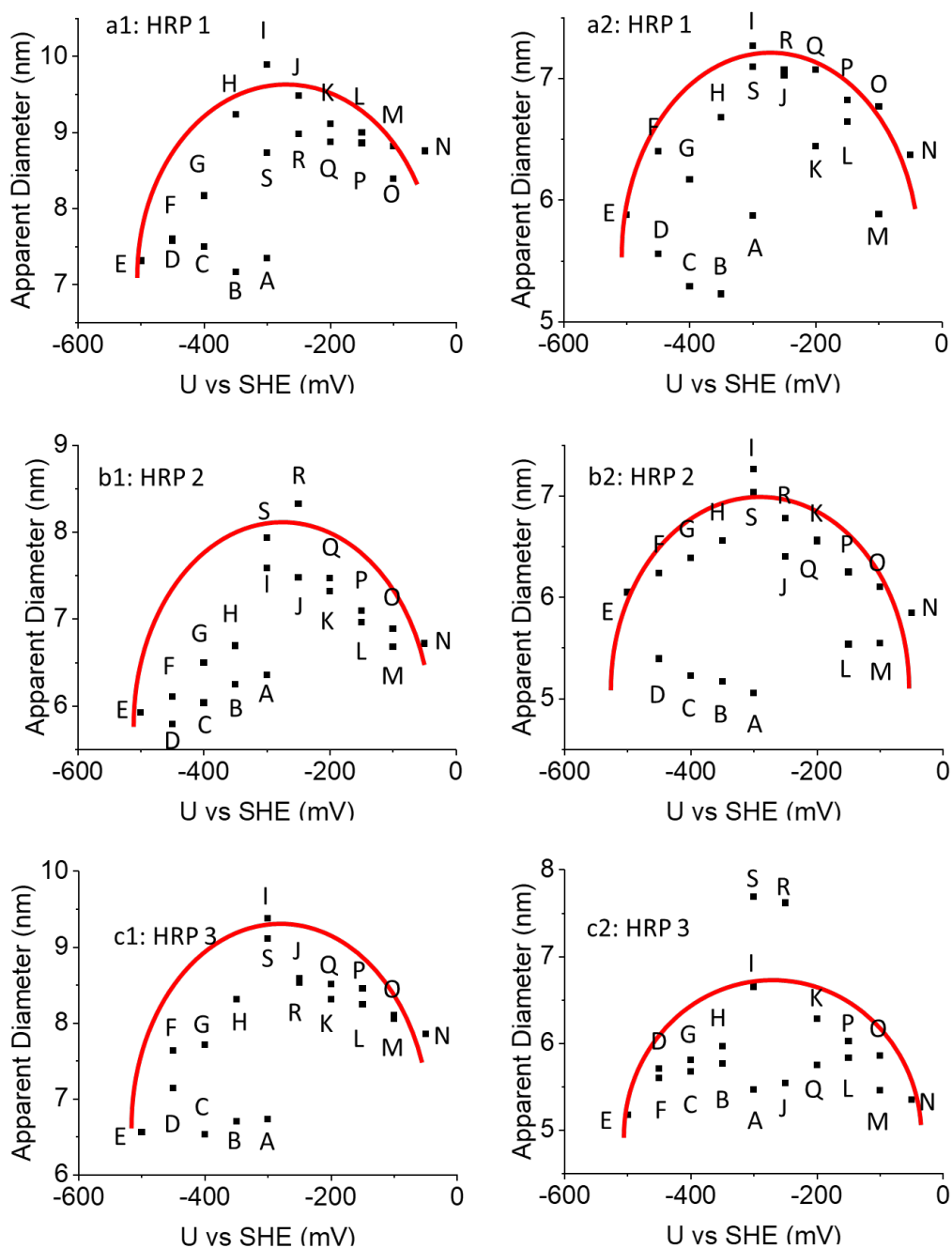


Figure 5.5 Potential dependency of HRP molecular apparent diameter measured from images of HRP modified a-HOPG surface by SECPM in 10 mM PBS (pH 7.4). HRP 1, 2 and 3 correspond to the number in figure 5.1 A, with elongated part included in (a1), (b1) and (c1), excluded in (a2), (b2) and (c2). The red curves show a qualitative potential dependency of HRP apparent diameter.

Volumes of adsorbed HRP molecules are approximately expressed as the product of apparent area and height and graphed versus substrate potential (Figure 5.6). Since the elongated part of the molecules does not influence the height measurement (height of elongated part being lower than that of the main part), the curves of volume versus U are divided into two sections: with (Figure 5.6 a1, b1 and c1) and without (Figure 5.6 a2, b2 and c2) the elongated part being included, just like the curves for area versus U and diameter versus U.

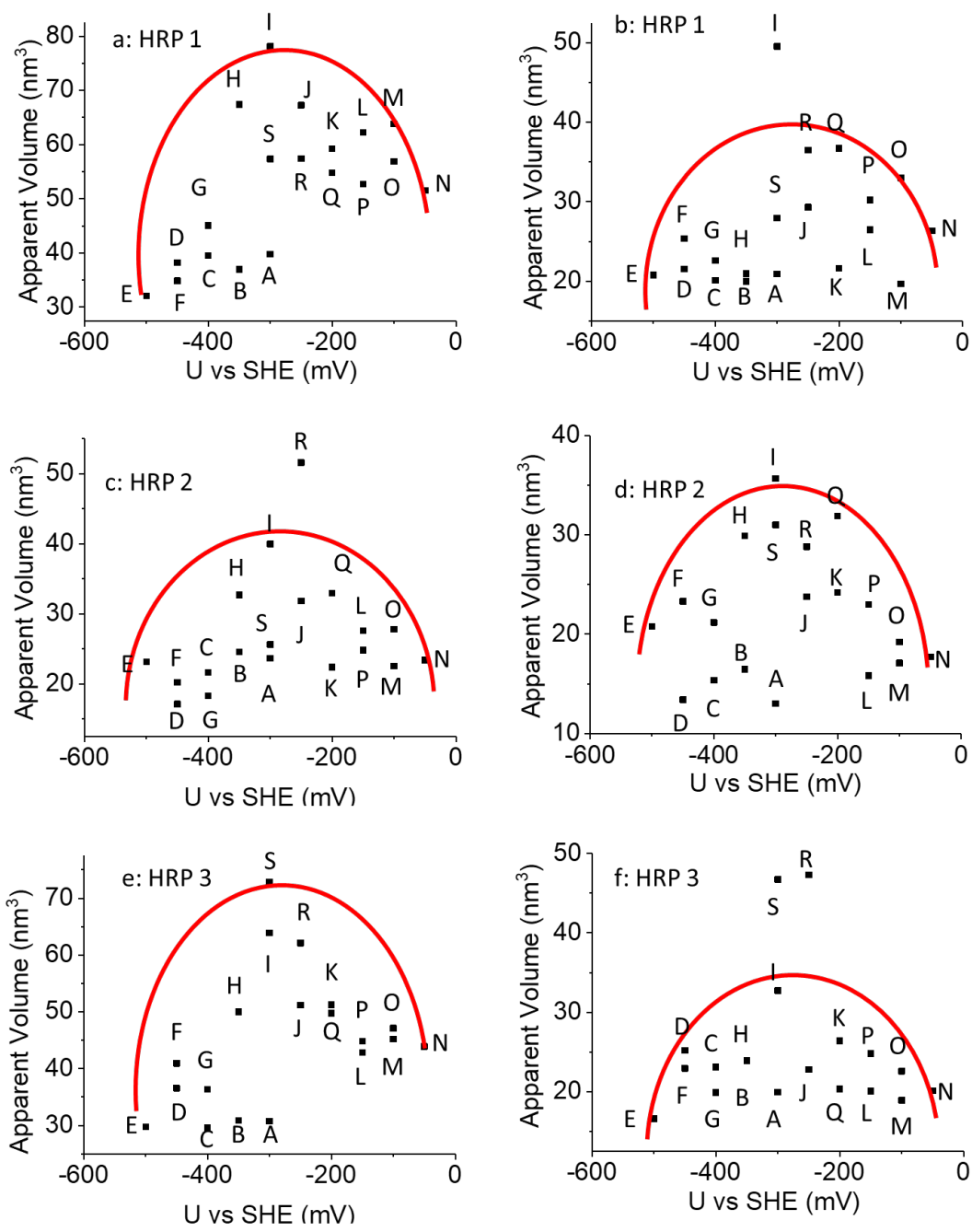


Figure 5.6 Potential dependency of HRP molecular apparent volume measured from images of HRP modified a-HOPG surface by SECPM in 10 mM PBS (pH 7.4). HRP 1, 2 and 3 correspond to the number in figure 5.1 A, with elongated part included in (a1), (b1) and (c1), excluded in (a2), (b2) and (c2). The red curves show a qualitative potential dependency of HRP apparent volume.

As described above, apparent height values vary between 0.5 nm and 1.1 nm, while apparent area values vary between 20 nm² and 80 nm². Numerically speaking, apparent area values contribute more to the final volume values, resulting in the volume versus potential curves exhibiting obvious similarity to the corresponding area versus potential curves.

To summarise, as can be observed from the SECPM images, the apparent size of single HRP molecules adsorbed on annealed HOPG surface is potential dependent. The maximum apparent size is observed when the substrate potential is -300 mV, and it decreases with potential shifting to both positive and negative directions. The exception is observed at the beginning stage of the imaging experiment (from image A to E in Figure 5.1), where no obvious apparent size potential dependency can be observed.

5.1.3 Discussions: Directly Monitoring the Potential Drop within HRP Molecular Structure

As discussed in section 4.3.3, if HRP molecules adsorbed on a-HOPG surface can behave like MOS capacitors, there should be potential dropping occurred within the tertiary structure while substrate potential shifting away from the “flat band potential”. It would be helpful to understand more about the MOS capacitor like HRP electrochemical behaviour if this potential drop could be directly monitored.

The relation between the potential at an arbitrary location x (φ_x) within the EDL and the potential at electrode surface ($x = 0$) could be approximately expressed as

$$\frac{\tanh\left(\frac{ze\varphi_x}{4k_B T}\right)}{\tanh\left(\frac{ze\varphi_0}{4k_B T}\right)} = \exp(-\kappa x) \quad (5.1)$$

where z is the absolute charge magnitude for a symmetrical electrolyte, e is the elementary charge, k_B is Boltzmann constant, T stands for room temperature in Kelvin and κ is the reciprocal of the Debye length.

As can be seen from equation 5.1, electrode potential, both at the HOPG surface and HRP surface, can be directly reflected by potential distribution within EDL.

SECPM maps the potential distribution in the EDL without significant perturbation to the substrate and current flowing that may cause potential damage to the fragile biomolecular structure. By performing potential dependent imaging of HRP molecules at single molecular level, one can establish a direct link between the apparent topological structure of HRP and the potential distribution in EDL, the feedback signal from which the topological information is converted.

From figure 5.2, 5.4, 5.5 and 5.6, potential dependent HRP apparent size variation is observed. Values of height, area, diameter and volume peak at around -300 mV and decrease while substrate potential shifting away. Since SECPM images reflect a convolution of both the electronic (potential) and topological structure, this apparent size variation could be attribute to either to the real size variation, that HRP molecules swelling or shrinking, or potential variation within the EDL, or both. In this work, the potential variation within the EDL around HRP molecules is discussed.

Figure 5.7 illustrates the potential dependent tip-substrate separation. During SECPM imaging in constant potential mode, the probe will approach to or retract away from the sample surface to keep the difference between the potential of sample surface and the local potential in EDL detected by the probe constant. SECPM approaching to the surface, which is reflected in the images as decrease of apparent height, indicates the decrease of the absolute value of the local potential and furtherly suggests the weakening of local electrical field under the precondition that other experimental conditions remain constant. One direct proof is the HRP apparent size decrease when U shifts away from -300 mV to -50 mV (Figure 5.7 B).

One point worth mentioning is due to the surface curvature of the globular HRP molecules, the influence of substrate potential changing on the EDL around HRP molecules is not only on the vertical direction, but also on lateral directions. So not only the apparent height, but the apparent area and diameter of HRP molecules on SECPM images will be potential dependent.

According to the theory mentioned above, when the potential shifts to the negative direction of -300 mV, the local electrical field should be strengthened due to the increase absolute value of substrate potential, leading to larger local potential at the location of probe apex. The probe should retract away from the sample surface to meet the pre-set potential setpoint, resulting in increasing HRP apparent size in the images. This is in conflict with the observation from the SECPM images of HRP modified a-

HOPG surface captured at U being more negative than -300 mV, that the apparent size of HRP molecules decreases with the increasing absolute U value. One possible explanation is the strengthening of local electrical field caused by increasing absolute U value being compensated by the potential drop within the HRP molecules.

The polypeptide chain forming the tertiary structure of HRP consists of 323 amino acid residues, 59 of which could be charged under electrochemical conditions by binding or losing hydron ions. Among the 59 amino acid residues, there are 21 arginine residues (19 of them located on the surface), 3 histidine residues (1 located on the surface) and 6 lysine residues (5 located on the surface) that can be positively charged, and 22 aspartic acid residues (16 located on the surface) and 7 glutamic acid residues (6 located on the surface) that can be negatively charged (Figure 5.8). Since the isoelectric point of HRP is 7.2 (Maehly, 1955), in 10 mM PBS electrolyte with pH being 7.4, HRP molecules are negatively charged.

Considering the polypeptide chain as a semiconductor material, as U getting more negative, the conduction band could be bent enough to meet the Fermi level, leading to HRP molecules capturing hydron ions and even becoming positively charged. This assumption could be supported by the CV curves of HRP modified a-HOPG surface, where sharp current density decrease (charging current as discussed in section 4.2) is observed after potential being more negative than -300 mV.

When a negative potential is applied to the substrate, negative charge will accumulate on the HOPG side at the solid-liquid interface. To balance the negative charge, positive ions in the electrolyte will accumulate at the electrolyte side near the interface, forming the electrochemical double layer. When U is more negative than -300 mV, increasing positive charge on the polypeptide chains will diminish the positive particle concentration in the EDL around HRP molecules, influencing the potential distribution in the EDL and furtherly leading to SECPM probe approaching to sample surface to maintain the constant potential difference between the tip and the sample surface. While when the probe is probing around the a-HOPG/PBS interface region, the enhanced local potential field caused by the increasing amount of positive charge to compensate the negative electrode potential will lead to probe retracting away from the surface for the constant potential difference between the probe and the electrode. The combination of probe approaching around HRP molecules and retracting around a-HOPG/PBS interface (black dotted line in Figure 5.7 C) results in the decrease of HRP apparent size observed from the SECPM images.

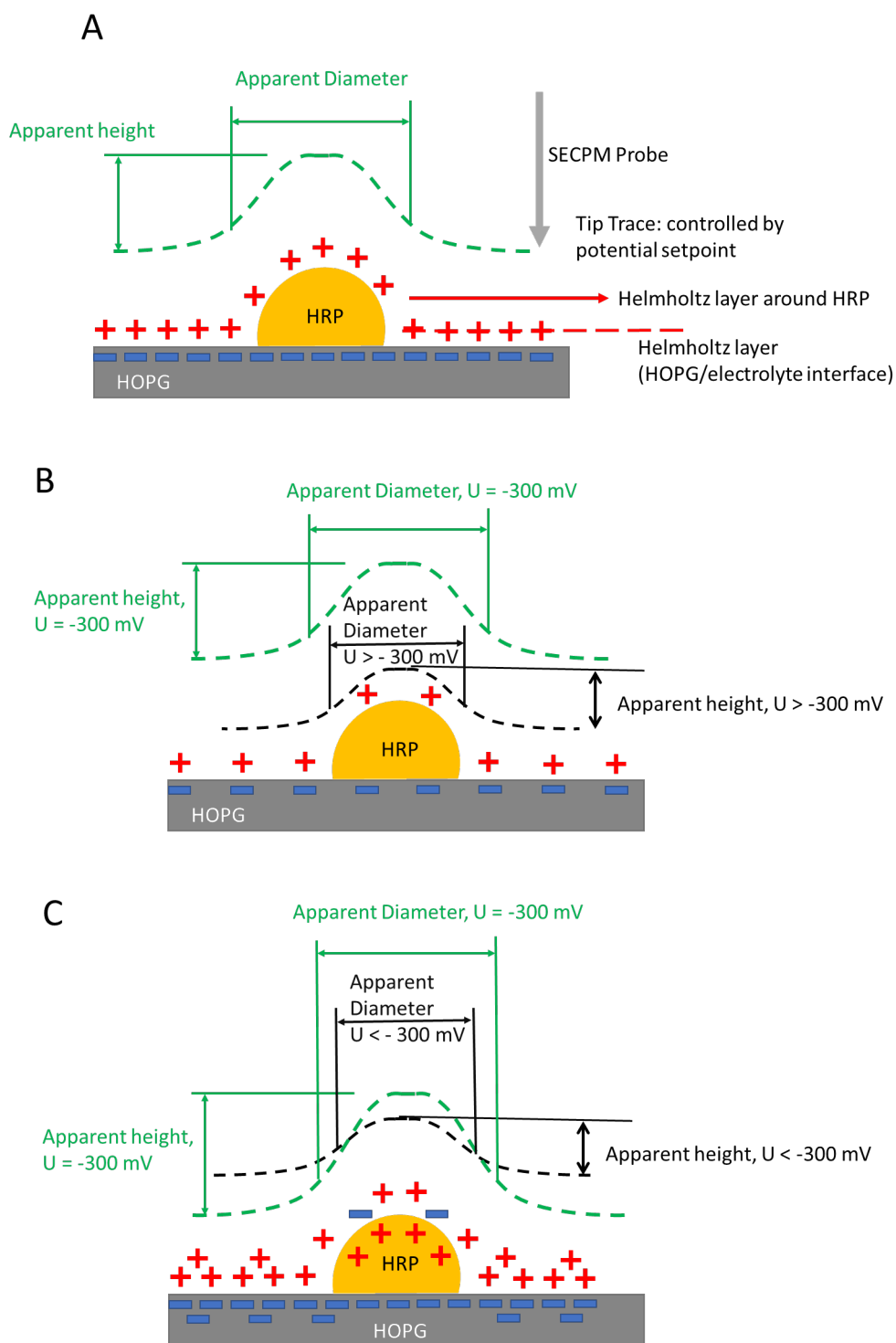


Figure 5.7 Illustration of potential dependent tip-substrate separation in SECPM. (A) A general illustration of charge distribution and tip-substrate separation (green dotted line) when $U = -300$ mV; (B) SECPM tip moving trace (black dotted line) when $U = -300$ mV; (B) SECPM tip moving trace (black dotted line) when U shifting to the positive side of -300 mV; (C) SECPM tip moving trace (black dotted line) when U shifting to the negative side of -300 mV.

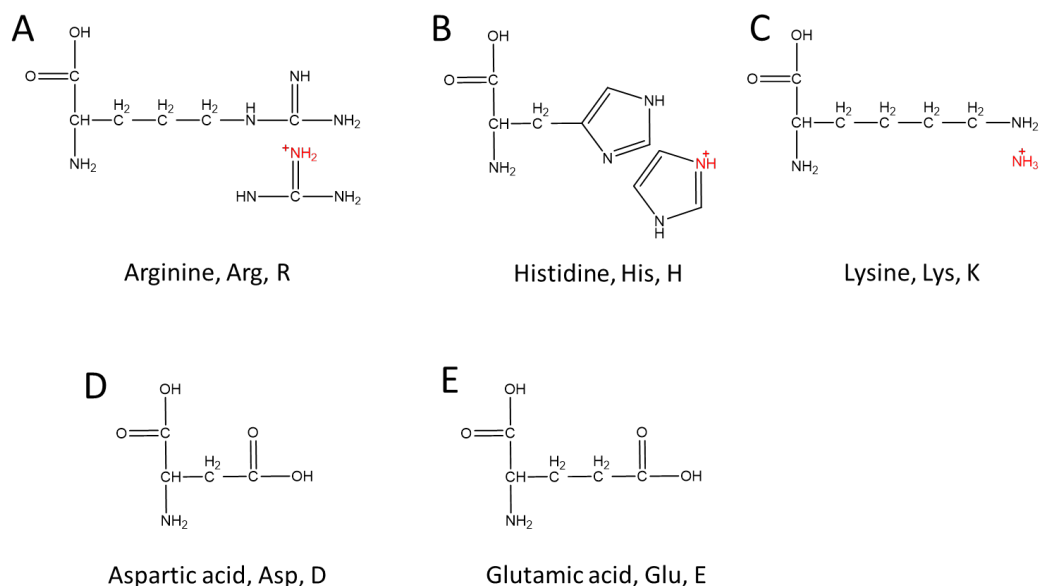


Figure 5.8 Molecular structure of (A) arginine, (B) histidine, (C) lysine (with the proton binding atom marked red), (D) aspartic acid and (E) glutamic acid.

5.2 EC-STM Imaging HRP Molecules Immobilised on Annealed HOPG Surface

5.2.1 Experimental Details

A sample prepared in the same method as the one used in SECPM imaging work was imaged by EC-STM. Other than changing the imaging technique (SECPM to EC-STM) and the sample, the other experimental conditions are the same as used in the SECPM imaging work discussed in 5.2.1. The parameters used for EC-STM setup are listed in table 5.2. One point worth being pointed out is the relatively high bias voltage applied between the tip and the substrate (U_{bias}), which is given by using the following equation:

$$U_{\text{bias}} = U_{\text{tip}} - U \quad (5.2)$$

where U_{tip} stands for the potential applied between the tip and the reference electrode and U is the potential applied between the WE (annealed HOPG modified with HRP molecules in this work) and the RE. Due to the poor conductivity of HRP molecules, a high U_{bias} (400 mV) is required to enable the tunnelling current to flow. In the meantime, this high U_{bias} is a challenge to the durability of tip insulation, which will be discussed in the following sections.

Current setpoint	300 pA
U_{bias}	400 mV
Integral gain	0.6
Proportional gain	1
Tip velocity	0.3 μm/s
Points per line	512
Scanner	J (125 μm * 125 μm)

Table 5.2 Parameter setup for SECPM imaging HRP modified a-HOPG in 10 mM PBS.

5.2.2 EC-STM Imaging: Single HRP Molecule and HRP Dimer

Figure 5.9 shows images of HRP modified a-HOPG surface captured by EC-STM under electrochemical conditions. Compared to the images captured by SECPM (Figure 5.1), the resolution of these images is relatively low, which is probably caused by both the poor HRP molecule conductivity and the relatively extreme imaging parameter setup. High U_{bias} may possibly cause high current leakage, which will influence the accurate detection of the feedback signal (tunnelling current). The current setpoint parameter, which determines the separation between tip apex and sample surface, is set at a relatively low value, 300 pA. This value is a compromise that the sample-tip separation is large enough to prevent the molecules being swept away by the moving tip, and in the meantime, minimise the sacrifice of imaging resolution.

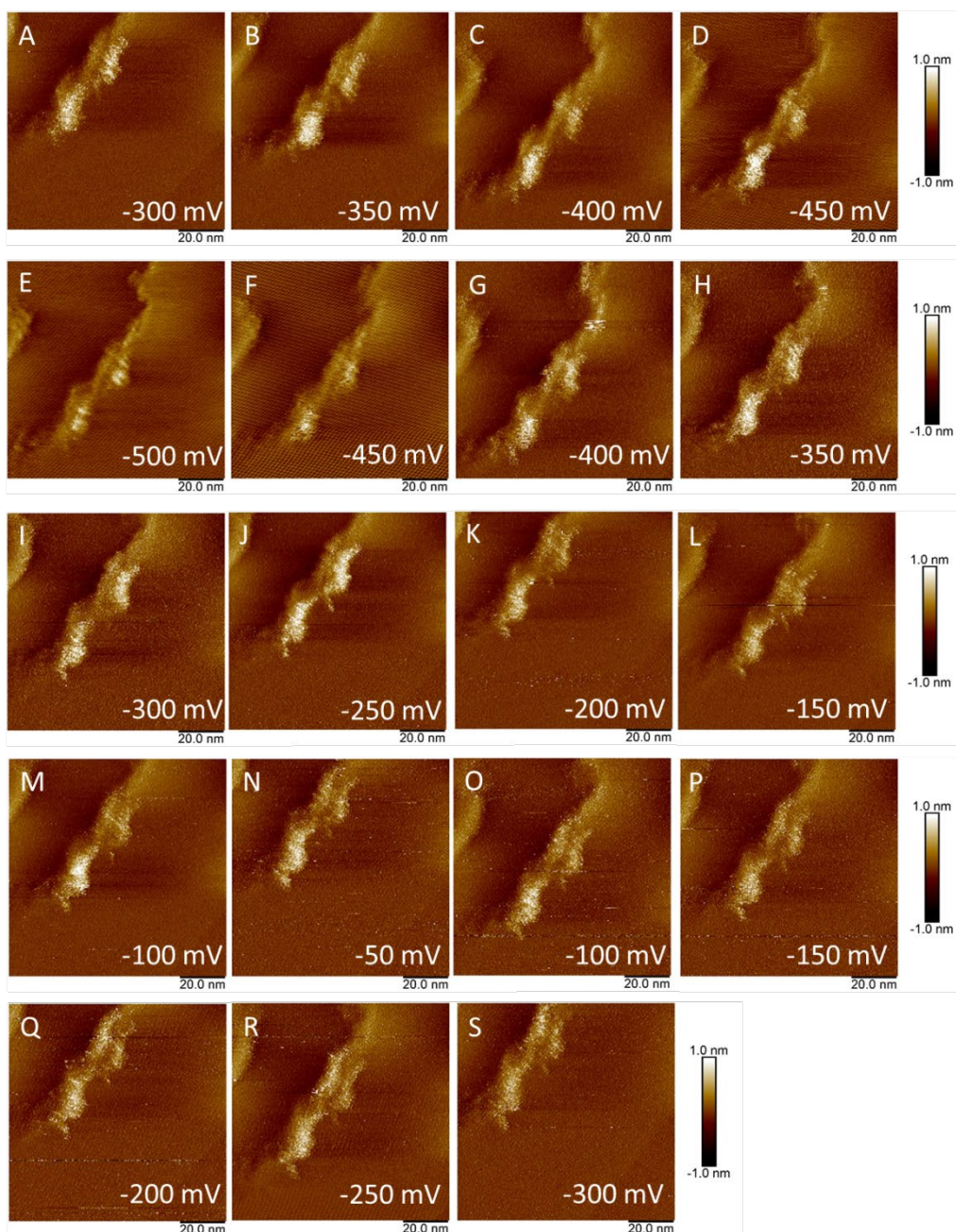


Figure 5.9 Series of EC-STM images of HRP modified a-HOPG in 10 mM PBS (pH 7.4). Images were captured subsequently according to the letter marked on the top left corner on each image at potentials as marked on the bottom right corner.

Figure 5.10 is a magnified version of figure 5.9 A and E. Due to the relatively poor resolution, the two particles observed sitting close to the step edge could be two dimers (formed by two individual HRP molecules), or a single molecule (marked as 1 in Figure 5.10 A) and a dimer (Figure 5.10 E). The obvious boundary of the two molecules forming the dimers could be observed from only figure 5.9 E. So in the following section, the two observed particles are measured and mentioned as dimers until further noticed.

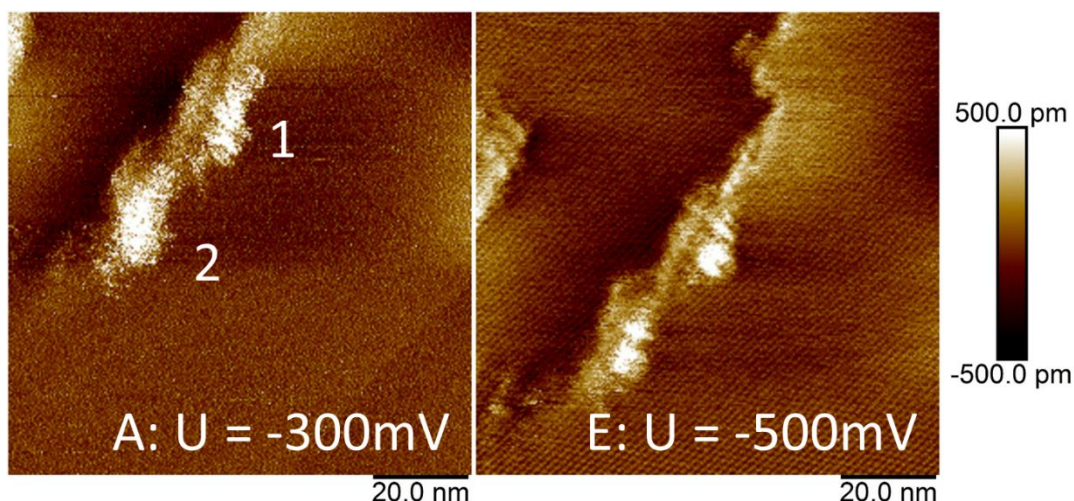


Figure 5.10 Magnified version of image A and E in figure 5.9.

Like the analysis for HRP molecules imaged by SECPM, the height, diameter, area and volume of the two dimers imaged by EC-STM are measured, calculated and graphed versus substrate potential (Figure 5.11, 5.12, 5.13 and 5.14), respectively.

As can be seen from figure 5.11, height of the two dimers vary between 0.7 nm and 1.6 nm. Compared to the height variation of the single molecules imaged by SECPM (Figure 5.2), the minimum height variation is almost the same, but the maximum shows nearly 50% increase. Since the dimers are formed by two HRP molecules sitting right next to each other, rather than one on top of the other, the real height of the dimer should be the same as a single HRP molecule. The apparent height of the dimers and single molecules from images captured by EC-STM and SECPM are converted from the feedback signals (tunnelling current for EC-STM and potential for SECPM). So the difference between the apparent height values could be generated from the different imaging mechanisms of the EC-SPM techniques. Despite the difference in values, the apparent height of dimers shows similar potential dependency as that of single molecules imaged by SECPM, that they both show weak potential dependency. The large apparent height values show mainly when the potential is around -300 mV. A few exceptions are observed from the height versus potential graph for dimer No. 2, height values larger than 1.2 nm are observed at point D ($U = -450$ mV), M ($U = -100$ mV), N ($U = -50$ mV) and O ($U = -100$ mV).

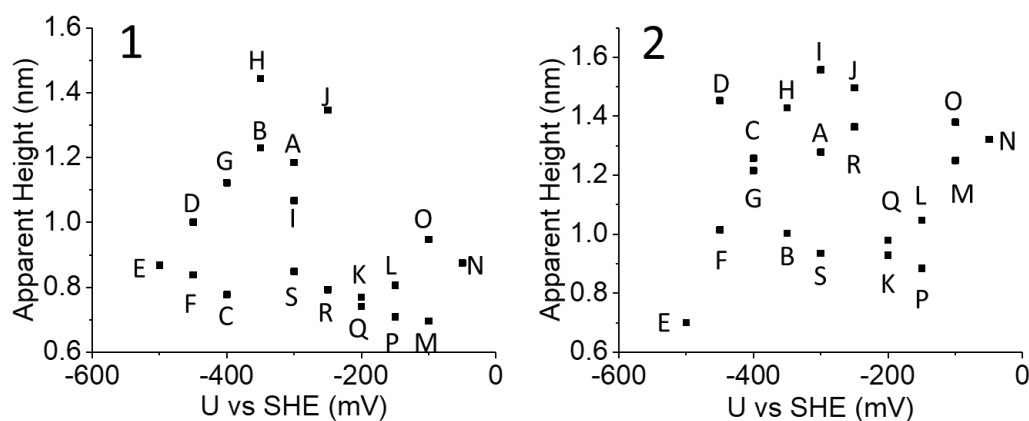


Figure 5.11 Potential dependency of HRP apparent height measured from images of HRP modified a-HOPG surface by EC-STM in 10 mM PBS (pH 7.4). 1 and 2 correspond to the number marked in figure 5.9 A, representing the two particles observed.

Figure 5.12 depicts the potential dependency of the apparent area of the dimers. For dimer No. 1, apparent area varies between 30 nm² and 50 nm², which is similar to that of the single molecules imaged by SECPM (Figure 5.4). While for dimer No. 2, apparent area variation is between 80 nm² and 165 nm², and these values are nearly twice of those measured from the SECPM images of single molecules. This result suggests that dimer 1 could be a single HRP molecule and dimer 2 is a dimer, formed by two HRP molecules.

Direct comparison between images of HRP molecules adsorbed on electrochemically oxidized HOPG surface captured by both SECPM and EC-STM at the same location were made and published by C. Baier and U. Stimming in 2009 (Baier & Stimming, 2009). From the direct comparison, it is exhibited that the apparent size of HRP molecules measured from images captured by EC-STM (4.3 * 3.4 * 2.4 nm³) is smaller than that measured from images captured by SECPM (5.4 * 5.2 * 3.2 nm³). So the possibility that the small part forming dimer No. 1 being a HRP molecule should not be simply ruled out.

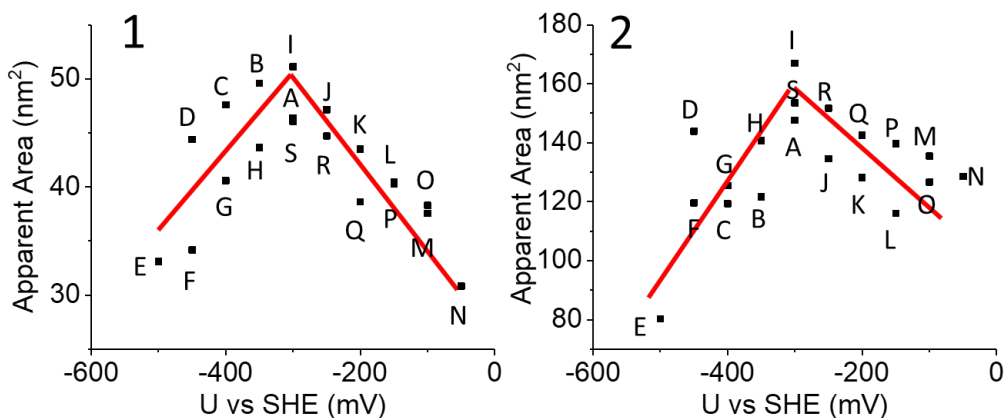


Figure 5.12 Potential dependency of HRP apparent area measured from images of HRP modified a-HOPG surface by EC-STM in 10 mM PBS (pH 7.4). 1 and 2 correspond to the number marked in figure 5.9 A, representing the two particles observed. The red lines show a qualitative potential dependency of HRP apparent area.

Diameters of the two dimers are also measured and graphed versus substrate potential (Figure 5.13). Since the objects imaged are dimers, here the measured diameter is considered as the combined diameters of two single molecules. For both the two dimers, the diameter versus potential curves show similar variation tendency as the curves for single HRP molecules imaged by SECPM, that the curves peak when U is -300 mV and drop with potential shifting to both positive and negative directions. Diameter of dimer 1 varies between 6.2 nm and 8 nm, which is similar to the variation range of a single molecule (Figure 5.5). For dimer 2, the variation range is from 12 nm and 14.5 nm, with one exception at point E (Figure 5.13-2), where the measured diameter is 10 nm ($U = -500$ mV). These values are nearly twice of those showed in figure 5.5 a2, b2 and c2, the curves of refined diameter versus potential.

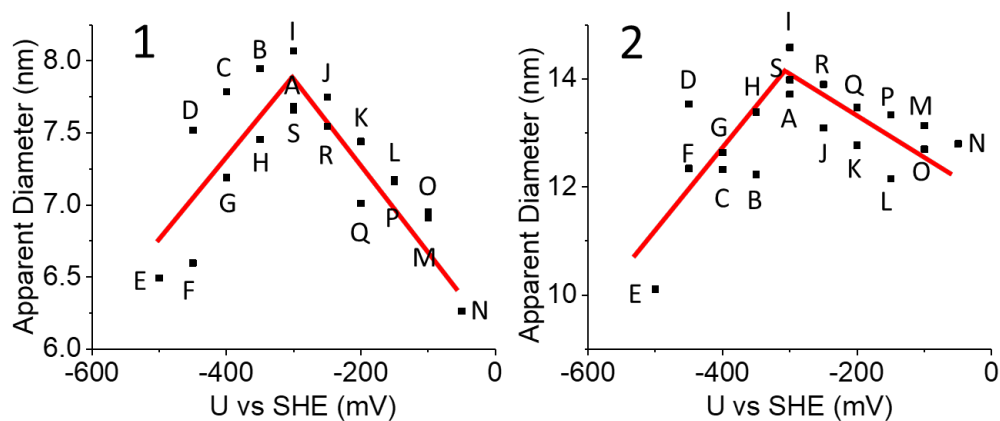


Figure 5.13 Potential dependency of HRP apparent diameter measured from images of HRP modified a-HOPG surface by EC-STM in 10 mM PBS (pH 7.4). 1 and 2 correspond to the number marked in figure 5.9 A, representing the two particles observed. The red lines show a qualitative potential dependency of HRP apparent diameter.

In figure 5.14, the curves of dimer volume versus potential are showed. As mentioned in section 5.1.2, since volume is calculated as the product of height and area, so numerically speaking, area values contribute more to the final volume results. The volume values show similar potential dependency as the apparent area values. For dimer 1, the calculated volume values are close to the corresponding ones of single HRP molecules imaged by SECPM (Figure 5.6). For dimer 2, due to the larger height and area, the calculated volumes are more than twice of the single HRP molecular volume. This could be attributed to the relatively poor resolution of the images captured by EC-STM, which leads to less accurate height and area measurement.

With all the measurement and calculation combined, the particle 1 should be a single HRP molecule rather than a dimer.

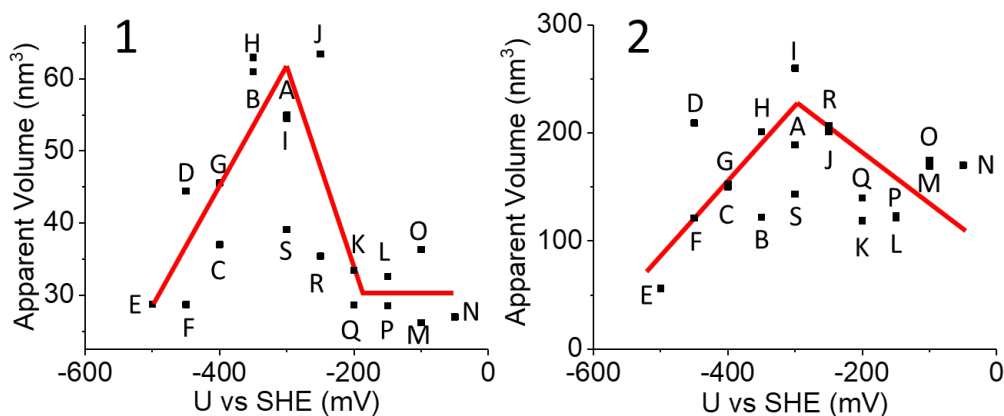


Figure 5.14 Potential dependency of HRP apparent volume calculated using data measured from images of HRP modified a-HOPG surface by EC-STM in 10 mM PBS (pH 7.4). 1 and 2 correspond to the number marked in figure 5.9 A, representing the two particles observed. The red lines show a qualitative potential dependency of HRP apparent volume.

As a brief summarization, due to the poor conductivity of HRP molecules, compared to SECPM, EC-STM resolved the enzyme molecules to a relatively low extent. Distortion and noise signals are observed from the EC-STM images. Despite the resolution difference, apparent size of HRP molecules adsorbed on a-HOPG surface measured from images captured by both EC-STM and SECPM show similar potential dependency, that the values tend to peak when U is around -300 mV. And as a support evidence to choose suitable equivalent model to analysis the impedance spectra of HRP modified a-HOPG surface, it can be seen from the SECPM and EC-STM images that HRP molecules stayed on the surface over a long timespan, suggesting low desorption rate. The Warburg element in model C in figure 4.11 C to represent the adsorption-desorption kinetics is not necessary in this situation.

5.2.3 Discussions: Indirect Potential Drop Monitoring, Influence on the Bias Voltage

Potential dependent contrast decay of glucose oxidase (GOD) on HOPG has been observed and analysed in detail (Wang et al., 2008b). The apparent height change is attributed to Faradaic current generated by the redox reactions happened at the active centre of GOD being detected by the tip during STM scanning.

In the work for this thesis, HRP modified a-HOPG surface was imaged by EC-STM as a comparison to the SECPM imaging results. A single HRP molecule and a dimer are identified from the EC-STM images and their apparent size variation is also observed with similar potential dependency as the ones imaged by SECPM. The difference between HRP and GOD is that during EC-STM potential dependent scanning, there is no redox reaction at the active centre of HRP molecules. But the mechanism that Wang et al. proposed could help the interpretation of the potential dependency of HRP apparent size in EC-STM images.

As proposed by M. Wang et al. that the current detected by the EC-STM tip (I), depending on which the tip-substrate separation is adjusted, is a sum of the tunnelling current (I_t) and the Faradaic current (I_f) generated by the redox reaction at the GOD active centre. In constant current mode, tip-substrate separation in EC-STM is constantly adjusted by the feedback loop to make I match the set point (I^0) by having the tip approach to or retract away from the sample surface. This potential dependent tip-substrate separation distance being reflect in the EC-STM images is the potential dependent height variation of GODs.

Since there was no Faradaic current during the EC-STM potential dependent scanning on the HRP modified a-HOPG surface, other factors that will influence the tunnelling current should be considered. For STM, the tunnelling current is determined by the tip-substrate separation distance (z), the bias voltage (U_{bias}) applied between the tip and the substrate, and the effective barrier height (ϕ_{eff}) which depends on the tip and substrate material according to equation 5.3 (Scheel et al., 1982)

$$I_t \propto U_{bias} \exp [-A\sqrt{\phi_{eff}z}] \quad (5.3)$$

where A is $10.12eV^{-1/2}nm^{-1}$. U_{bias} is calculated as equation 5.2.

For the operation of the EC-STM instrument, U_{bias} and U values are manually set before the experiments, and U_{tip} will be automatically controlled according to equation 5.2.

As discussed in section 4.3.3, potential drop occurred within the HRP molecular structure when the substrate potential becoming more negative than -300 mV, leading to the potential between HRP molecules and reference electrode higher than U . In this case, when the EC-STM is scanning over the HRP molecules, the real bias voltage should be

$$U'_{bias} = U_{tip} - U_{HRP} \quad (5.4)$$

where U'_{bias} is the potential difference between the EC-STM tip and HRP molecules, and U_{HRP} is the potential difference between HRP molecules and reference electrode.

From Equation 5.2 and 5.4 the difference between the setup U_{bias} and U'_{bias} could be calculated using the following equation:

$$\Delta U = U'_{bias} - U_{bias} = U - U_{HRP} \quad (5.5)$$

where ΔU is the difference between the real bias voltage and the setup bias voltage.

Assuming that a tip-substrate separation H^0 corresponds to a tunnelling current that detected by the tip being I^0 , one can consider three cases with initially $I = I^0$ and H (tip location) = H^0 :

- (a) $\Delta U = 0$, then $I = I^0$, and finally $H = H^0$, meaning the tip remains at the same position;
- (b) $\Delta U > 0$, then $I > I^0$, and finally $H > H^0$, meaning tip retracting away from the surface to maintain constant tunnelling current;
- (c) $\Delta U < 0$, then $I < I^0$, and finally $H < H^0$, meaning tip approaching to the surface to maintain constant tunnelling current.

Figure 5.15 illustrates the three tip-sample separation modes corresponds to the three cases discussed above.

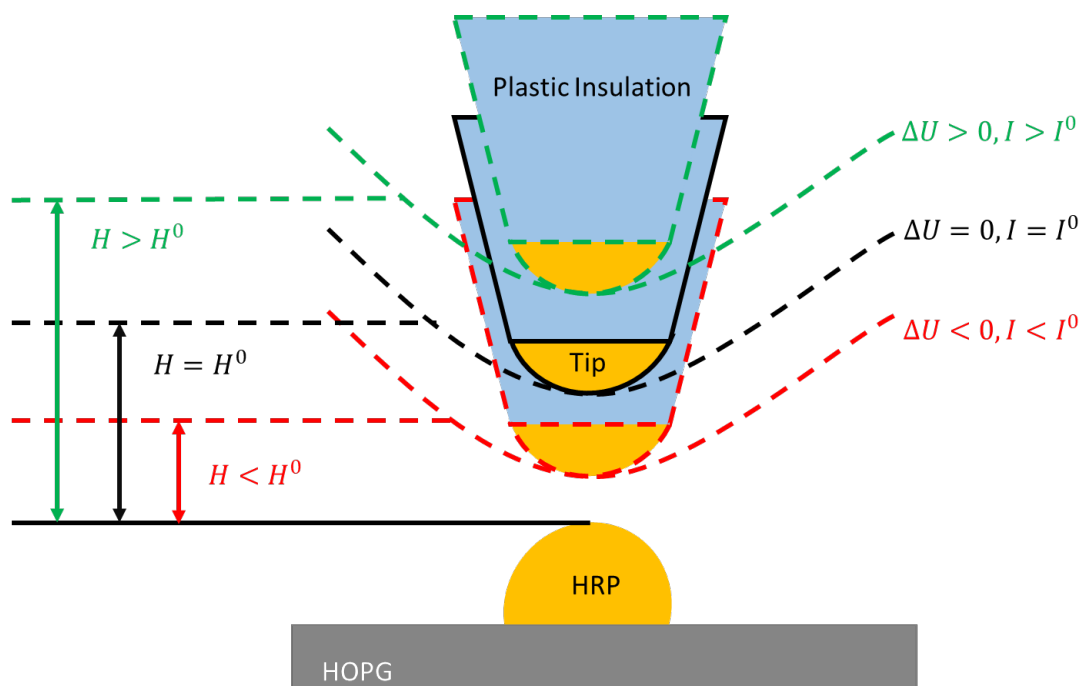


Figure 5.15 Illustration of EC-STM imaging HRP modified HOPG.

In the EC-STM potential dependent imaging HRP modified a-HOPG surface experiment, when U was on the negative side of -300 mV, a potential drop caused probably by hydrogen ions being attracted to HRP molecules occurred, leading to case (c) mentioned above that $\Delta U < 0$ and EC-STM tip approaching to the surface. This is reflected in the apparent size versus potential curves for the single molecule and the dimer that apparent size decrease with potential getting more negative (Figure 5.11, 5.12, 5.13 and 5.14).

No obvious current density increase or decrease can be observed from the CV for HRP modified a-HOPG in 10 mM PBS (Figure 4.3) when the potential being more positive than -300 mV. In this case, there is no charging or discharging to the HRP molecules and so no potential drop within the molecular structure. Without the potential drop, ΔU equals to zero, which means there should be no obvious apparent size variation for HRP molecules.

As can be seen from figure 5.11-2, 5.12-2, 5.13-2 and 5.14-2, the decrease of HRP apparent size, including area, diameter and volume, is much more pronounced on the negative side of -300 mV than that on the positive side. The exception is the apparent height values, which fluctuate too much to show any obvious potential dependency.

For the single HRP molecules, the size versus potential curves are shown in figure 5.11-1, 5.12-1, 5.13-1 and 5.14-1, the apparent size decrease is equally pronounced on both sides of -300 mV. One possible explanation is due to the relatively low resolution, it is hard to tell the exact boundary of the single molecule from the EC-STM images (Figure 5.9). In most of the images in figure 5.9, especially the ones captured at the potential close to -300 mV, the single molecule is completely merged with the surroundings, causing the lack of accuracy in the measurement of the apparent size. And since it is almost impossible to tell the molecular boundary, this inaccurate measurement cannot be easily corrected by excluding the elongated part as what has been done to measurement of HRP molecules in SECPM images (Figure 5.3).

However, the boundary merging situation should not influence the measurement of the height, and obvious contrast decay is observed during the procedure that U increasing from -300 mV to -50 mV. One reasonable assumption could be the single molecule was swept away before figure 5.9 K (U = -200 mV) being captured. This assumption is supported by the sharp decay observed in Figure 5.11-1 from point J to point K. After point K, the apparent height values behave nearly potential independent and stay at values close to that of point K, which furtherly indicates the desorption of the single molecule.

5.3 Conclusions

SECPM and EC-STM have been applied to monitor the potential drop within HRP molecular structure under electrochemical conditions. For the first time, potential dependent SECPM imaging of HRP molecules at single molecular level has been performed. From the SECPM images, apparent molecular size decay has been observed when the substrate potential shifted away from the flat band potential (-300 mV).

EC-STM was also applied to perform potential dependent imaging of HRP molecules on annealed HOPG surface. Potential dependency of HRP apparent size similar to that observed by SECPM has been observed using EC-STM.

As a technique that directly measures the potential distribution in the EDL, the SECPM imaging results support the MOS approximation proposed to interpret the potential dependent capacitance behaviour of HRP molecules measured by EIS.

As comparison and complementary, EC-STM results provide indirect supports to the MOS approximation. The contribution from potential drop within the HRP molecular structure is suggested to be included in the bias voltage, through which, the potential drop could be reflected as the HRP apparent size variation in EC-STM images.

Comparing to SECPM, EC-STM resolves HRP molecules to a lower extent, and this has been proved by the direct comparison of images of HRP modified HOPG electrode captured by both techniques at the same location (Baier & Stimming, 2009). But EC-STM is still a powerful technique to study the potential variation within the enzyme molecular structure from the current point of view.

One advantage of using EC-STM and SECPM is the easiness and convenience of switching between these two techniques. Once probe insulation being highly durable under relatively extreme imaging conditions can be achieved, potential dependent imaging of the same enzyme molecules at the same location at single molecular level performed by these two techniques will be a great contribution to the further study of bioelectronic devices.

Chapter 6. Direct Probing of Electrochemical Double Layer Using Scanning Electrochemical Potential Microscopy

In 2004, SECPM was originally introduced as a technique to investigate the Au(111) electrode/NaBF₄ solution interface by using a miniaturized potential probe to measure the potential distribution along the electrochemical double layer with sub-nanometre spatial resolution (Woo et al., 2004). It was further improved and applied to Pt/KCl and SiO₂ (on Si)/KCl interfaces by Allen J. Bard et al (Hurth et al., 2007). Here in this work, SECPM was applied to acquire potential versus distance curves at freshly cleaved HOPG/PBS interface, to help gain more understanding of the EDL structure and the mechanism of SECPM technique.

6.1 Debye Length Calculation and Experimental Parameter Selection

To investigate the influence of ionic strength on the potential distribution in EDL, PBS with three different concentrations (10 mM, 1 mM and 0.1 mM) were used in the experiment. Since electrolyte concentration directly determines the Debye length, which further will influence the potential distribution in the EDL, different tip-substrate separation distances were set to record the potential distribution spectra. Debye length of each electrolyte is calculated using the following equation (Dukhin & Goetz, 2017):

$$\kappa^{-1} = \sqrt{\frac{\varepsilon_r \varepsilon_0 k_B T}{2 \times 10^3 N_A e^2 I}} \quad (6.1)$$

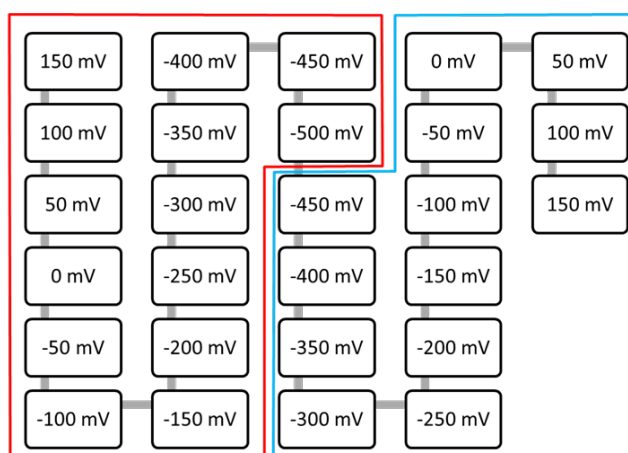
where κ^{-1} represents the Debye length, ε_0 is the vacuum permittivity, ε_r is the dielectric constant of water, k_B is Boltzmann constant, T stands for room temperature in Kelvin, N_A is Avogadro constant, e is the elementary charge, and I stands for the ionic strength of the electrolyte (Na⁺, H⁺, OH⁻, H₂PO₄⁻ and HPO₄²⁻) in molar units. The calculated Debye length for each electrolyte and corresponding instrumental parameter setup used in the experiment are listed in table 6.1.

Electrolyte concentration (mM)	10	1	0.1
Debye length (nm)	2.096	6.629	20.957
Chosen tip-substrate separation (nm)	10	40	110
Tip velocity (nm/s)	0.5	0.5	1
Time required per spectrum (s)	40	160	220
Points per line	512	512	1024
Points per nm	51.2	12.8	9.3

Table 6.1 Debye length of electrolytes and corresponding experimental parameters.

Tip-substrate separation determines the scan range of the potential profile and it was set to be at least 5 times of the Debye length to fully cover the potential decay length. Tip velocity determines the velocity of tip retracting away/approaching to the sample surface. It would be ideal that for all the experiments, same number of data points per nanometre could be collect for better comparison, but 512 and 1024 points per spectrum are the only two values accepted by the system.

Other than electrolyte concentration, another influence factor to the potential distribution in the EDL is the substrate potential U . Potential profiling spectra were recorded with varying substrate potentials. With the substrate potential decreasing from 150 mV to -500 mV (with 50 mV interval), one spectrum was recorded at each potential. Same recording procedure was repeated right after the spectrum at $U = -500$ mV was recorded but with the potential increasing back from -500 mV to 150 mV, to study if the potential varying direction will influence the potential distribution and check the reproducibility of the whole experiment (Figure 6.1). The notations up and down are used to separate the two spectra recorded at the same U .



Red frame: U decreasing from 150 mV to -500 mV, noted as down

Blue frame: U increasing from -500 mV to 150 mV, noted as up

Figure 6.1 Potential variation pattern according to which the SECPM potential profiling spectra were recorded.

6.2 Potential Profiling Curve Analysis

SECPM potential profiling spectra: curves of recorded potential (ϕ) versus the tip-substrate separation, were recorded under the experimental conditions mentioned above. All the experiments were repeated for 3 times to test the reproducibility. After finishing one experiment, the left electrolyte was removed and another 100 μ L electrolyte was introduced to exclude the influence of solvent evaporation.

To check the reliability and reproducibility of SECPM potential detection under electrochemical conditions, the potential difference ($\Delta\phi$) between the detected potential at the end and the start points of each potential profiling curve was calculated as:

$$(\Delta\phi) = \phi_{end} - \phi_{start} \quad (6.2)$$

where ϕ_{start} is the potential difference recorded at the first point of each potential profiling curve (around 5 mV) and ϕ_{end} is the potential difference recorded at the last point. The calculated $\Delta\phi$ values were graphed versus their corresponding substrate potentials (Figure 6.2).

As can be seen from Figure 6.2, the slope of all the potential difference versus substrate potential curves are close to -1, suggesting the potential decay in the system being linearly proportional to the applied potential.

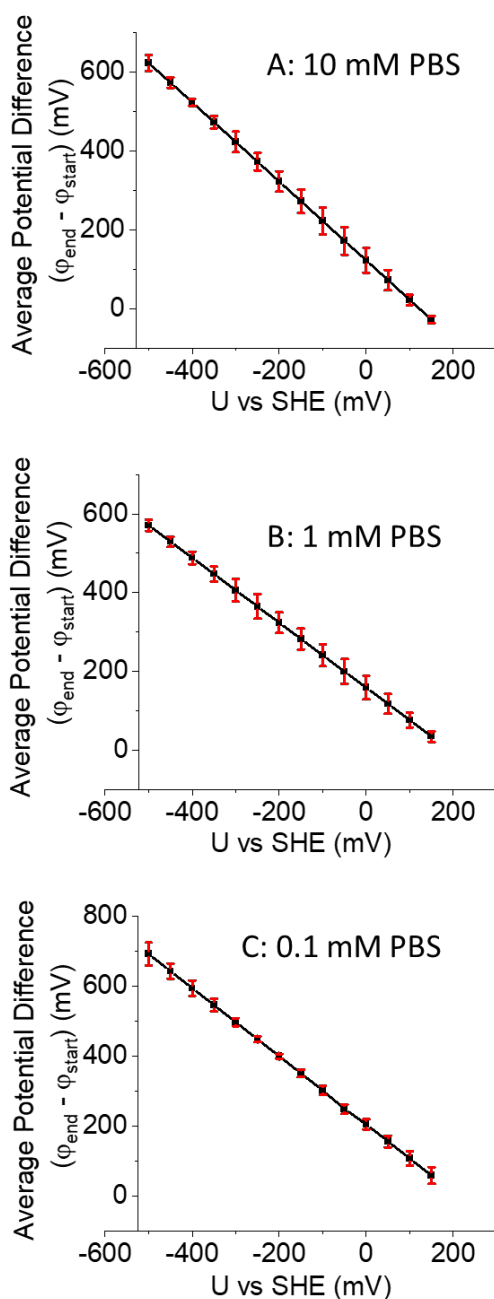


Figure 6.2 Potential dependency of the potential difference between the detected potentials at the beginning and end of each potential profiling curves recorded at f-HOPG and (A) 10 mM PBS, (B) 1mM PBS and (C) 0.1 mM PBS interfaces

Figure 6.3 shows potential profiling curves recorded at -200 mV (down as marked in Figure 6.1) in all the profiling experiments. As can be seen from the curves, the maximum difference within the curves is about 40 mV, which is observed from figure 6.3 B, the potential profiling curves recorded in 1 mM PBS, between experiment 1 (red) and 2 (yellow). This maximum difference is about 10% of the maximum potential. The curves in figure 6.3 suggest good reproducibility of the SECPM potential profiling experiments. And for all the three different electrolyte concentrations, the results recorded in experiment 2 (yellow) and 3 (blue) agree with each other quite well. So the following analysis was made using the data recorded in experiment 2 (yellow).

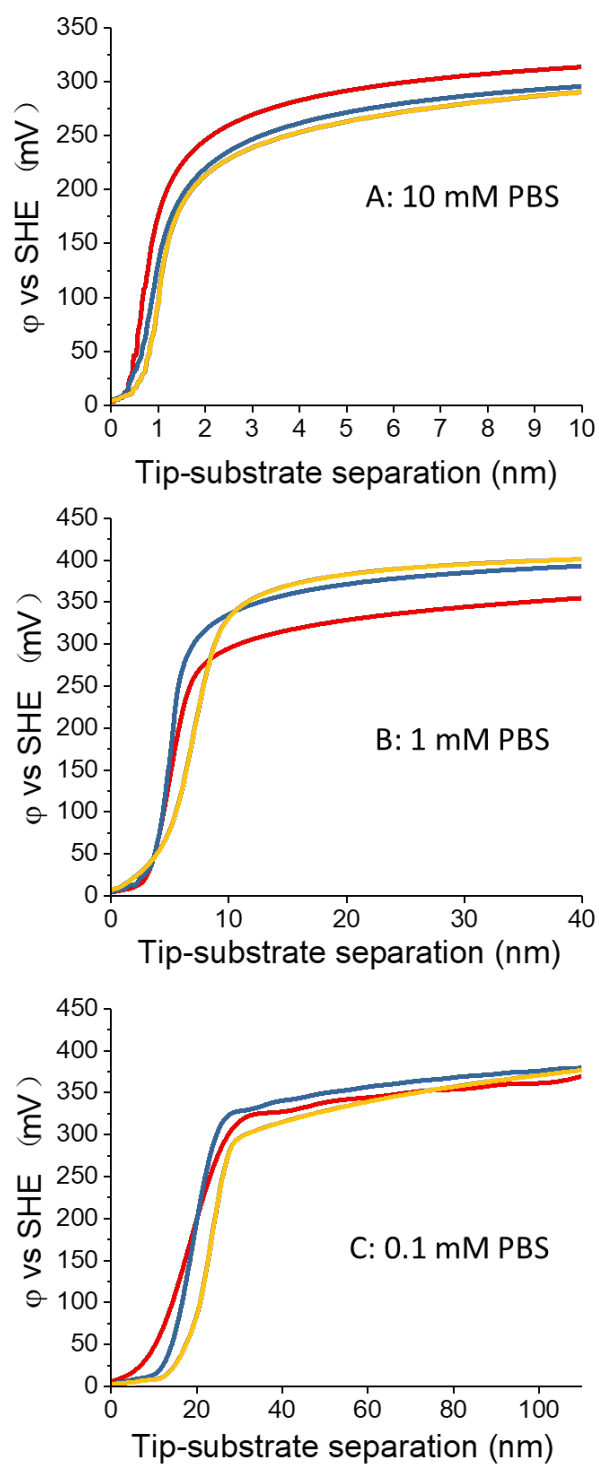


Figure 6.3 Direct comparison within potential profiling curves recorded at f-HOPG and (A) 10 mM PBS, (B) 1mM PBS and (C) 0.1 mM PBS interfaces at -200 mV (down as marked in Figure 4.29). The colour colours stand for experiment 1 (red), 2 (yellow) and 3 (blue) performed one after another.

Another test to check the reproducibility is direct comparison of potential profiling curves recorded at the same substrate potential at different time. In figure 6.4, potential profiling curves recorded when substrate potential was -400 mV at HOPG surface in 10 mM, 1 mM and 0.1 mM PBS are presented. As can be seen from the figure 6.4 A, when the electrolyte concentration was 10 mM, the potential profiling lines, red and blue (recorded later than red) almost overlap, with slight difference when the tip-substrate separation is between 2.5 nm and 5 nm. In figure 6.4 B, electrolyte concentration decreases to 1 mM, and obvious potential difference can be observed between 5 nm and 30 nm tip-substrate separation, especially when tip-substrate separation is around 7 nm, the difference of the potentials at the two curves are nearly 100 mV. More significant potential difference can be seen in figure 6.4 C, where the electrolyte concentration is 0.1 mM. An average potential difference of 170 mV is observed from the two potential profiling curves, and the difference peaks to be almost 300 mV at around 40 nm tip-substrate separation.

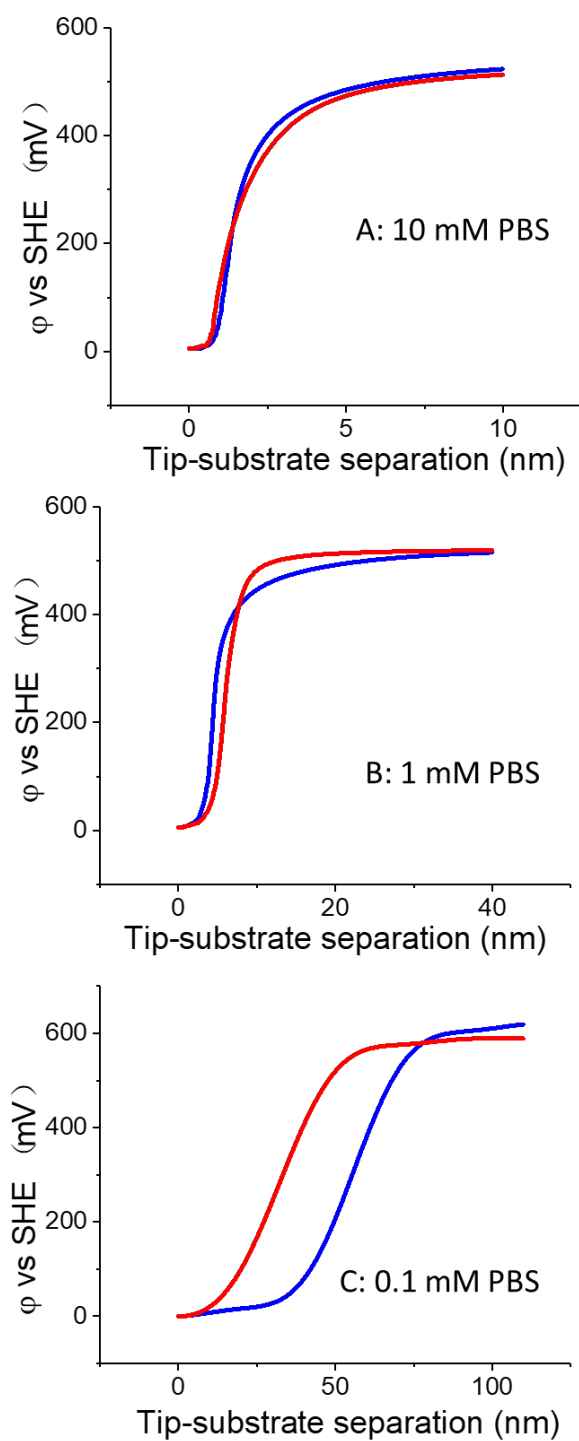


Figure 6.4 Comparison between SECPM potential profiling curves recorded at -400 mV down (red) and up (blue) (as in Figure 6.1) at HOPG and (A) 10 mM, (B) 1 mM and (C) 0.1 mM PBS interfaces at -400 mV.

The reason of choosing spectra recorded at -400 mV to make the comparison is the relative short timespan between the capture of these spectra (-400 mV down and up, Figure 6.1). As explained previously, due to the space limitation in the experimental setup, only around 100 μ L electrolyte could be introduced into the system. Electrolyte evaporation could be a vital influence on the potential profiling experiment. Figure 6.5 shows potential profiling spectra recorded at HOPG surface in 10 mM PBS at different substrate potentials. The differences between the two spectra are calculated using the following equation

$$\Delta\varphi(x_{max}) = \varphi(x_{max})_{up} - \varphi(x_{max})_{down} \quad (6.3)$$

where $\Delta\varphi$ stands for the difference between the local potential of two spectra recorded at the same substrate potential, x_{max} stands for the maximum tip-substrate separation, φ_{up} is the local potential in the potential profiling curves recorded at the potential in the blue square marked as up in figure 6.1, and φ_{down} is the local potential in the potential profiling curves recorded at the potential in the red square marked as down.

$\Delta\varphi(x_{max})$ at 0 mV, -200 mV and -400 mV are -20 mV, 14 mV and 10 mV, respectively. It is obvious that for a more positive potential, the time gap between the recording of two spectra at it gets longer, leading to more time for solvent evaporation. So only the spectra recorded at the potentials in the down section in Figure 6.1 (potential decreasing from 150 mV to -500 mV) are used for further analysis.

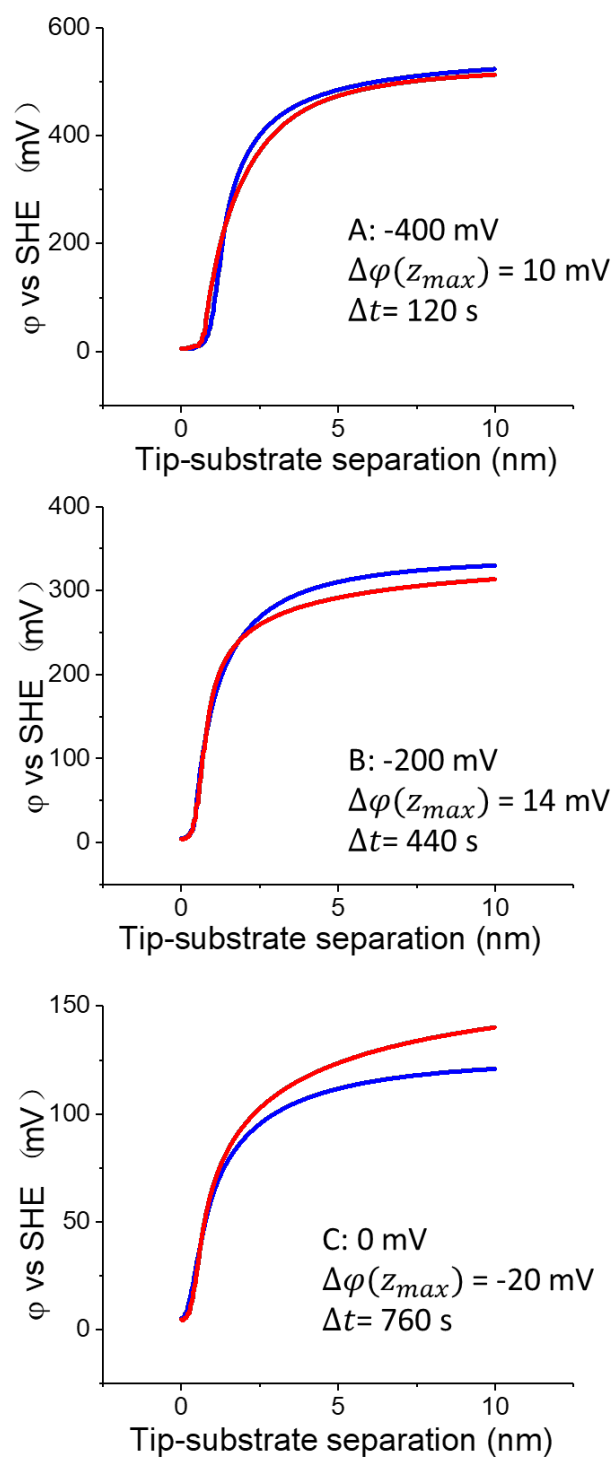


Figure 6.5 Comparison between SECPM potential profiling curves recorded at HOPG surface in 10 mM PBS at (A) -400 mV, (B) -200 mV and (C) 0 mV. Colours of spectra recorded at potential in down (red) and up (blue) frame in figure 6.1.

Figure 6.6 depicts potential profiling spectra taken on freshly cleaved HOPG surface in PBS. In all the spectra, the potential profiling curve starts at 5 mV, rather than the substrate potential, on Y-axis. That is because SECPM detects the difference between the potential of WE and the potential of the position where the apex locates. The value 5 mV is a pre-set value for potential setpoint, the parameter for SECPM standing for the tip-sample potential difference that the feedback holds constant in constant potential mode. Potential setpoint determines the tip-sample separation distance. Smaller potential setpoint leads to smaller tip-sample separation and furtherly higher imaging resolution. However, the tip crashes easily when potential setpoint is smaller than 5 mV. So, in SECPM spectroscopy mode, 5 mV is the minimum potential setpoint accepted by the operation software and the tip-sample separation distance corresponding to 5 mV potential difference is automatically recorded as 0 nm by the system in all the potential profiling curves.

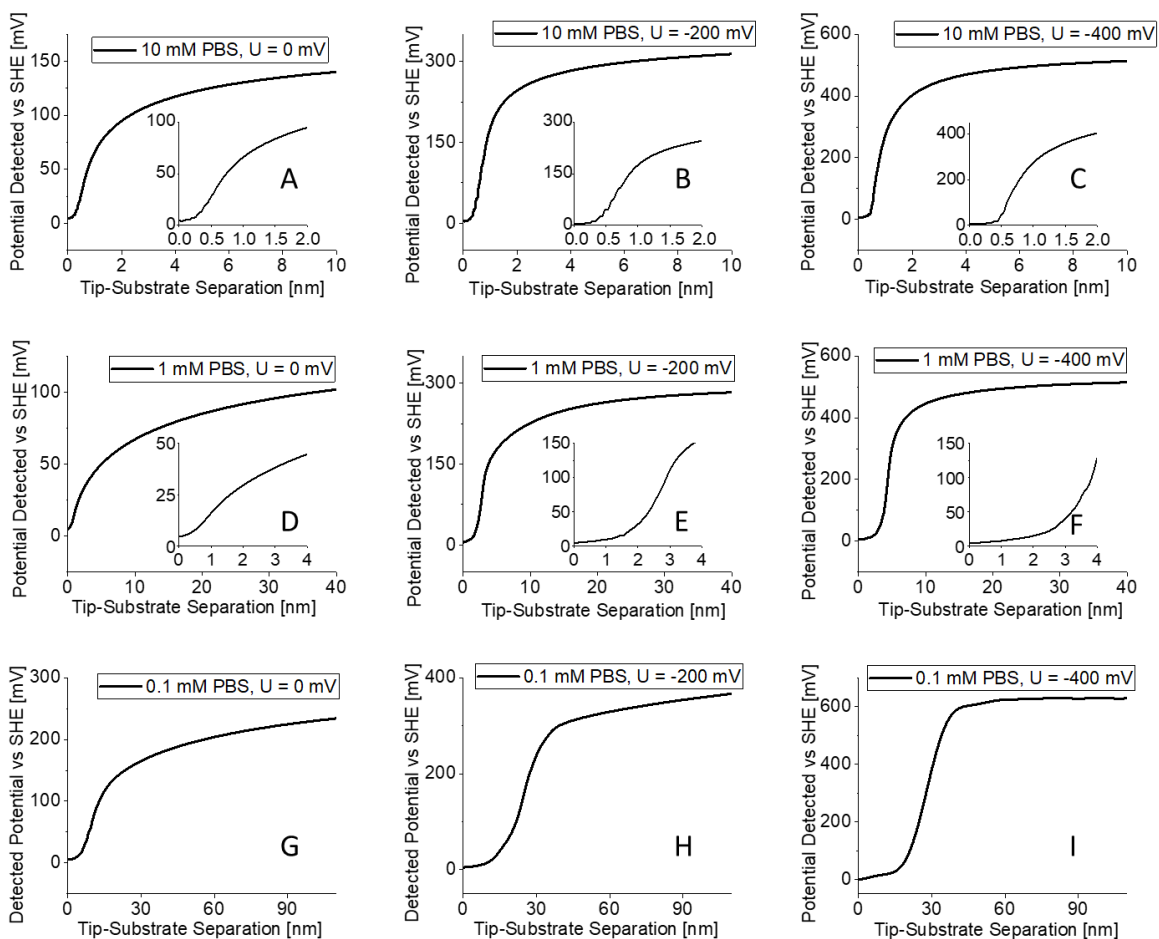


Figure 6.6 SECPM potential profiling of the EDL at highly oriented pyrolytic graphite (HOPG) and 10 mM (A, B and C), 1 mM (D, E and F) and 0.1 mM (G, H and I) PBS interfaces at potentials: (A, D and G) 0 mV, (B, E and H) -200 mV, and (C, F and I) -400 mV.

One feature worth noticing is at the beginning of every potential profiling curve, there is no immediate response of potential decay. As can be seen from Figure 6.6, the tip-substrate separation distance without immediate response of potential decay is directly proportional to substrate potential U and inversely proportional to the electrolyte concentration. In an ideal case, which can be predicted by Poisson's equation, the potential decay should happen immediately while the tip retracting away from the electrode surface. (Figure 6.7). The delay of potential decay response could be attribute to the inaccuracy of potential detection caused by the overlapping of EDL existing at both the HOPG/PBS and tip/PBS interfaces at close tip-substrate separation distance.

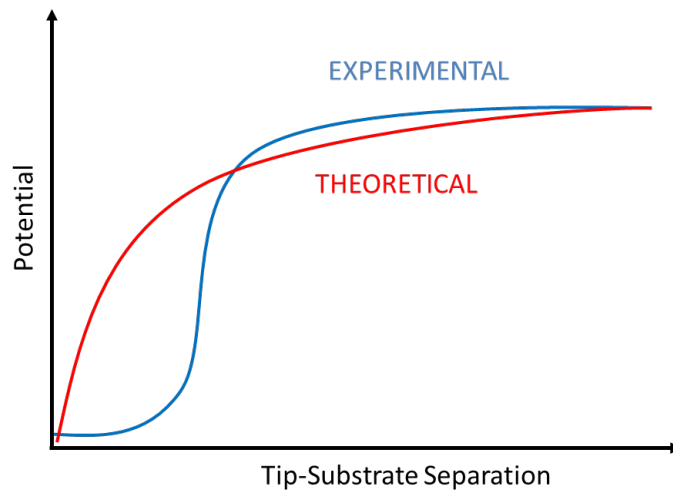


Figure 6.7 Theoretical and experimental potential distribution along the EDL.

Other than lack of immediate potential decay response at the beginning of the curves, steep potential decay is also observed from all the curves. One interesting feature is, when the PBS concentration is 10 mM and 1 mM, the decay lengths of the potential profiles are shorter than their corresponding Debye length, and the potential decay gets steeper with decreasing substrate potential. While in the case that PBS concentration is 0.1 mM (Debye length is 20.9 nm), when substrate potential is -200 mV or -400 mV, the observed potential decay lengths are longer than the Debye length.

After the steep potential decay, the φ values get close to constant as the tip-substrate separation becoming larger than the thickness of the diffuse layer. As can be seen from figure 6.6, maximum φ shows obvious potential dependency, that the measured value of φ reaches maximum when the electrode potential being -400 mV and shows minimum at 0 mV.

When U shifts away from 150 mV to the positive direction, the potential decay occurs to the negative direction with reference to the y-axis (Figure 6.8).

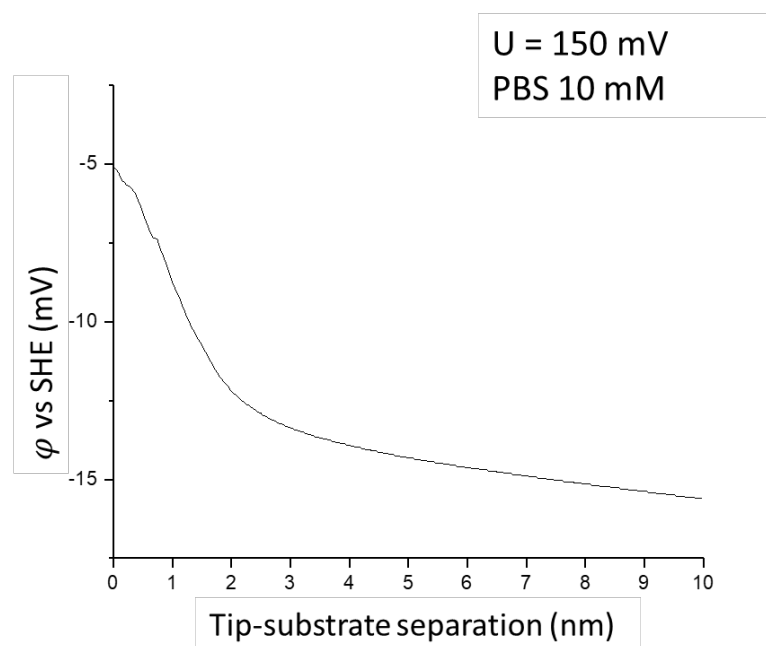


Figure 6.8 SECPM potential profiling curve recorded at HOPG surface in 10 mM PBS (pH 7.4) at 150 mV vs SHE.

To summarise, SECPM shows high reproducibility in potential profiling. The recorded potential versus tip-substrate separation curves do not follow the theoretical prediction based on Gouy-Chapman-Stern theory.

As can be seen from Figure 3.10, the tip used for potential profiling is nearly a cross section of a metal wire with diameter of 0.25 mm, which is much larger than the Debye length of the electrolytes (Table 6.1). EDL exists both at the substrate-electrolyte interface and the tip-electrolyte interface. At close tip-substrate distance, the situation will be the two EDLs overlapping each other, instead of the ideal situation in which a dimensionless probe measuring the potential distribution without introducing any perturbation into the EDL.

Further discussion will be given in the following section.

6.3 Discussions

Here in this work, it is the first time that both potential and electrolyte concentration dependency being observed from the SECPM potential profiling spectra. The spectra acquired in this experiment do not fit the Gouy-Chapman-Stern model. In particular,

the absence of immediate response of potential decay at the beginning of the spectra cannot be explained by current theoretical EDL models.

One possible explanation is the overlapping of EDLs existing at the HOPG/PBS interface and probe/PBS interface. Due to the probe preparation technique, the probe apex used to detect the potential within the EDL is nearly the cross section of a metal wire, the diameter of which is 0.25 mm. Comparing to the electrolyte Debye length (2.09 nm to 20.9 nm) and the maximum tip-substrate separation (10 nm to 110 nm), the huge apex (diameter 0.25 mm) could introduce both physical and electrical influence on the EDL at HOPG/PBS interface. Even if an ideal nanometre sized apex could be used, the EDL overlapping still cannot be ruled out. Research has been done on the ion filled nanogap between the tip and the electrode surface, suggesting perturbation from the tip to the potential measurement at close tip-separation distance (Kornyshev & Kuznetsov, 2006).

Other than the experimental conditions, efforts have also been made to the improvement of the current theoretical model to describe EDL at solid-liquid interface. Poisson equation assumed the electrolyte relative permittivity (ϵ_r) as a constant. While F. Booth(Booth, 1951, 1955) proposed a theory based on previous work done by Debye(Debye, 1929), Kirkwood(Kirkwood, 1939), Onsager(Onsager, 1936) and Fröhlich(H., 1949), to explain how polar solvent responded to electric field by introducing an electric field dependent ϵ_r . S. K. Mitra and his colleagues(Das et al., 2012) applied Booth's model to a theoretical description of how did the ϵ_r change in the EDL, indicating an increasing ϵ_r with increasing distance from the interface, and a late response of potential decay at the beginning of the ϵ_r increasing curves.

The mechanism of how the SECPM tip detects the potential within the EDL at the interface of electrolyte and a WE at a fixed potential is still disputable. In 2018, B. Horrocks and his colleagues published their theory on the mechanism of SECPM, in which SECPM is described to behave like EC-STM when the tip apex is close to the substrate, with detected signal contributed by tunnelling current, Faradaic current and leakage current at the amplifier to which the probe is connected (Friedl et al., 2018). In this mechanism, the potential detected by the SECPM probe is the summary of the potentials corresponding to the three kinds of current mentioned above.

Theoretically speaking, the high impedance tip amplifier built in the SECPM hardware setup should preclude any current passing through the tip. However, one point

remaining controversial is the existence of tunnelling current between SECPM tip and the substrate at close tip-substrate distance. Horrocks et al. suggested that SECPM operated like STM at close tip-substrate distance, and the tunnelling process dominated the potential detection of SECPM probe. Until the tip-substrate separation became large enough to create great tunnelling resistance, SECPM potential profiling curves will remain insensitive to the local electric potential.

At sufficiently large tip-substrate separation distance that makes tunnelling resistance much greater than faradaic resistance, faradaic process will start to make the main contribution to the potential detected by SECPM. Here, faradaic process is represented as the discharge of tip capacitance responding to the variation of tip-substrate distance. Assuming the high impedance amplifier could minimise the leakage current to be negligible, with large tip-substrate distance, SECPM could respond to the local electric field in the EDL.

Using the mechanism proposed by B. Horrocks et al., a regression model to the experimental data showed in figure 6.6 F ($U = -400$ mV in 1 mM PBS) has been defined to generate an approach curve $E(z)$ using the following equations:

$$E(z) = \frac{R_{\parallel}}{R_t} E(c) + \frac{R_{\parallel}}{R_F} [E_m + \varphi(z)] \quad (6.4)$$

$$\frac{\tanh(f\varphi/4)}{\tanh(\frac{f\varphi_2}{4})} = e^{-\kappa z} \quad (6.5)$$

where $\frac{1}{R_{\parallel}} = \frac{1}{R_t} + \frac{1}{R_F} + \frac{1}{R_{inp}}$, R_t is the tunnelling resistance, R_F is the Faradaic resistance assumed to be time-independent for simplicity, R_{inp} is the input impedance of the amplifier, E_c is the contact potential (Traunsteiner et al., 2015), E_m is the mixed potential of the tip in the bulk solution, $f = F/RT$ (F : Faraday constant, R : universal gas constant and T : temperature in Kelvin), φ_2 is the potential at the outer Helmholtz plane. For the sake of simplicity, tunnelling resistance is modelled as a simple exponential

$$R_t = R_t^0 \exp(\beta z) \quad (6.6)$$

with inverse distance parameter $\beta = 1.9832 \text{ nm}^{-1}$. The local electric potential $\varphi(z)$ is modelled as two separate parts: (a) a linear potential drop within the Helmholtz layer and (b) an exponential decay in the diffuse layer as expressed below:

$$\varphi(z) = \varphi_{OHP} \exp(-\kappa(z - z_{OHP})) \quad (6.7)$$

Figure 6.9 shows the comparison between the experimental potential profiling curve acquired in 1 mM PBS with -400 mV substrate potential and the regression model using equation 6.4, 6.5, 6.6 and 6.7. As can be seen from the graph, the theoretical regression curve fits the experimental data quite well and the fitting can be improved by introducing a complete model for the local electric potential $\varphi(z)$.

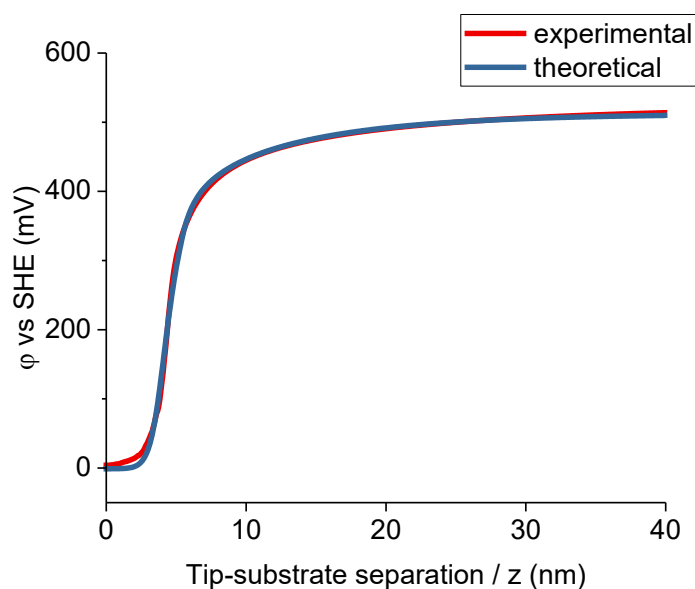


Figure 6.9 SECPM potential profiling curves of HOPG in 1 mM PBS (pH 7.4) with substrate potential as -400 mV. Red curve: experimentally acquired data, same as the curve in figure 6.6 F. Blue curve: regression fitting curve using equation 6.4, 6.5, 6.6 and 6.7. The parameters used for calculation were: inverse Debye length $\kappa = 6.62 \text{ nm}^{-1}$; inverse tunnelling length $\beta^{-1} = 1.983 \text{ nm}^{-1}$; contact potential $E_c = 513.3 \text{ mV}$; tunnelling resistance $R_t = 8.18 \text{ M}\Omega$; Faradaic resistance $R_F = 18 \text{ G}\Omega$; and Amplifier input impedance $R_{inp} = 1 \text{ P}\Omega$.

6.4 Conclusions

SECPM is a powerful tool to perform potential profiling in the EDL at solid-liquid interface. Potential dependency and electrolyte concentration dependency of the potential distribution have been observed from the potential profiling curves, from which future quantitative analysis could benefit. Numerical analysis has been done regarding the tip geometry for SECPM imaging and potential profiling (Hamou et al., 2010b). Further studies on the tip materials, fabrication and insulation techniques could help the preparation of tip with minimum perturbation to the EDL.

Chapter 7. Conclusions

The research work in this thesis consists of two parts. The first part is about the electrochemical behaviour of horseradish peroxidase (HRP) at solid-liquid interface without the presence of commonly used substrates, such as hydrogen peroxide, the redox reactions of which involve HRP as an enzyme. The second part continues the investigation of using scanning electrochemical potential microscopy (SECPM) to perform direct local potential probing within the electrochemical double layer (EDL).

HRP has been studied thoroughly about its molecular structure, enzymatic behaviours, and possible applications in the field of bioelectronic devices. Most of these works has been done by applying HRP as a catalyst, the electrochemical behaviours of HRP itself are rarely reported. In this work, the potential dependent capacitance of HRP is reported for the first time and a metal oxide semiconductor (MOS) capacitor approach has been proposed as an explanation for the experimental results. The MOS capacitor approach is furtherly supported by the experimental results acquired by SECPM and electrochemical scanning tunnelling microscopy (EC-STM).

HRP molecules were characterised as adsorbent on annealed highly oriented pyrolytic graphite (HOPG) surface. Scanning probe microscopy (SPM) techniques, including atomic force microscopy (AFM), EC-STM and SECPM were applied to characterise the HOPG surface before and after thermal treatment as comparison. SPM images showed the smooth HOPG surface was roughened by the thermal treatment, with sharp step edges turned hackly and flat basal plane bestrewed with defects formed by carbon oxidation.

HRP adsorption on annealed HOPG surface was done by drop casting technique. Solutions with different HRP concentrations were tested to achieve maximum surface coverage by the molecules while avoiding HRP aggregation through intermolecular interaction. HRP modified annealed HOPG samples were imaged by AFM in liquid condition, confirming the surface of the sample prepared by drop casting with 0.04 mg/mL HRP solution was covered with large amount of single HRP molecules.

Cyclic voltammetry (CV) was applied as preliminary experimental condition screening procedure. CV curves were recorded within the potential range between -800 mV and

800 mV vs standard hydrogen electrode (SHE) at freshly cleaved HOPG (f-HOPG) surface, annealed HOPG (a-HOPG) surface and HRP modified a-HOPG surface in 10 mM phosphate buffer solution (PBS). No significant redox peaks were observed from the CV curves for HRP modified a-HOPG surface, suggesting no charge transfer reactions happened to the adsorbed HRP molecules. Sharp current density increase was observed when the potential became more negative than -300 mV vs SHE. Charge accumulated during the CV scan was calculated and found being independent on the CV sweeping rate. Instead of redox current, current charging the adsorbed HRP molecules was observed from the CV curves.

Since the HRP molecules were charged during the CV scan, electrochemical impedance spectroscopy (EIS) was used to monitor the capacitance of adsorbed HRP molecules. The observed HRP capacitance was significantly potential dependent, with behaviour analogous to that of a typical p-type MOS capacitor. Accumulation region and depletion region were observed from the capacitance-potential curve of HRP molecules. The charging current observed from the CV curves fitted perfectly to the accumulation region, in which positive charge started to accumulate on HRP molecules.

An MOS capacitor approach as a description of the potential dependent capacitance behaviour of HRP molecules was proposed, assuming the HRP modified annealed HOPG to be a MOS capacitor, in which HRP molecules correspond to the semiconductor layer, annealed top layer of HOPG and the bulk HOPG are regarded as the oxide layer and metal layer, respectively.

This work could be furtherly extended by conducting EIS measurements with substrate potentials on the positive side of -50 mV vs SHE. Based on the theory of MOS capacitors, an inversion region should be observed when the gate potential, the substrate potential in this work, being more positive than a certain threshold value.

Form the capacitance-potential curve of the adsorbed HRP molecules, the rate of HRP capacitance variation (dC/dU) was calculated and graphed versus substrate potential. Like a MOS capacitor, the flat band potential, at which there should be no potential drop in the HRP molecule, was determined as the peak of the dC/dU vs potential curve occurred at -300 mV vs SHE. Since EIS is not capable of directly monitoring the potential variation within the HRP molecules, other techniques should be considered to test the feasibility of the MOS approximation.

SECPM maps the potential distribution within the EDL at solid-liquid interface. As the EDL potential distribution being directly related to the substrate potential, SECPM could monitor the potential variation within the HRP structure by monitoring the potential variation in the EDL at HRP-electrolyte interface.

This is the first time that SECPM being applied to perform potential dependent imaging of biomolecules at single molecular level under in situ conditions. The apparent sizes, including height, area, diameter, and volume were measured, calculated, and graphed versus the substrate potential at which the images were captured, respectively. The apparent size versus potential curves exhibited shapes similar to that of the dC/dU vs U curve, peaking at -300 mV and then descending while potential shifting away from -300 mV to both positive and negative directions.

Apparent size versus potential curves peaking at -300 mV indicated a maximum EDL strength. As potential shifting to the positive direction, concentration of the positive particles, by which the negative charges accumulated in the HOPG side of the interface was balanced, will be reduced due to the increasing repelling electrostatic force, resulting in the weakening of local EDL strength, and furtherly the decreasing of HRP apparent size.

On the negative side of -300 mV, the size-potential curves also exhibited decreasing tendency, which was in conflict with the fact that the EDL strength should be enhanced due to the increasing attracting electrostatic force to the positively charged the particles in the electrolyte. This phenomenon could be explained by the MOS approximation of HRP molecules, that potential drop occurred in the HRP structure and being reinforced as the potential getting more negative than its "flat band potential". The increasing electrostatic force at the electrode surface was neutralized and surpassed by the potential drop in the HRP structure, resulting in the weakening strength of EDL around HRP molecules.

SECPM images present a convolution of electrical properties and topological structure of the HRP molecules. Using SECPM, potential variation within the HRP structure can be visualized and reflected as the apparent size variation of the HRP molecules in the images. This technique provides a new perspective of directly monitoring the potential variation within the particles at nanometre scale and offers possibilities to deal with a variety of electrochemical surface science problems under physiological conditions.

One disadvantage of SECPM technique is the inevitable HRP apparent size decrease with substrate potential being more positive than -300 mV vs SHE. A promising remedy is EC-STM, the switch to which from SECPM can be easily achieved without any perturbation to the sample, enabling direct comparison between the potential density distribution within the EDL and the local density of states (LDOS) of the sample surface.

An HRP modified a-HOPG sample prepared in the same method as the one imaged by SECPM was imaged using EC-STM under the same experimental conditions. Instead of single molecules, an HRP dimer was observed from the EC-STM images. Apparent size of the dimer, including height, area, diameter, and volume were measured, calculated, and graphed versus substrate potential. Comparing to the apparent size versus potential curves obtained from the SECPM images, these curves from EC-STM images also peaked at -300 mV and exhibited decreasing tendency as potential shifting away. One significant difference was the apparent size decrease while potential shifting away from -300 mV was much more pronounced on the negative side.

This result could also be explained by the MOS approximation that due to the potential drop within the HRP structure, the bias voltage between the tip and the HRP dimer became smaller than that between the tip and the substrate, resulting in tip approaching to the sample surface to maintain the constant tunnelling current feedback signal.

For a MOS capacitor, potential drop within the body (the semiconductor layer) also occurs when the potential is on the positive side of its flat band potential, just not as significant as the case of potential being on the negative side. This could explain the slight decrease in apparent dimer size on the positive side of the apparent size versus potential curves.

The combination of SECPM and EC-STM results solidifies the MOS capacitor approximation in the description of HRP capacitance potential dependency. Although comparing to SECPM, EC-STM cannot resolve the HRP molecules to a higher extent because of the relatively poor sample conductivity, direct comparison of images captured by these two techniques at the same location on the same sample could widen the understanding of enzyme electrochemical behaviours. The major limitation preventing the switch between EC-STM and SECPM is the poor durability of insulation

coating of the tip under relatively harsh electrochemical conditions. Further studies could be extended on the improvement of probe fabrication and insulation technologies.

The MOS capacitor approximation of describing the electrochemical behaviour of HRP molecules raises the possibility that globular proteins with a metal ion containing active centre could behave like bioelectronic devices. Comparing to the conventional bioelectronics, enzyme molecules can be conveniently acquired from plants or microorganism, possess impeccable biocompatibility, smaller in dimensions and other advantages from which a variety of field could benefit. Future endeavour could be casted on the exploration of more enzyme molecules with potential of behaving like bioelectronic and the development of techniques to control the enzymatic bioelectronic behaviours.

The second part of this work continues the SECPM potential profiling experiment initiated by Woo et al. and Hurth et al. In this work, for the first time that both the potential dependency and the electrolyte concentration dependency of the potential decay in the EDL were observed through direct probing of potential distribution. The observed potential decay was nearly in qualitative agreement with the prediction of Gouy-Chapman-Stern theory that potential decay happened within the range close to the Debye length of the corresponding electrolyte.

The late response of potential decay at close distance from the electrode surface was also observed. The tip-substrate separation over which no immediate potential decay response was directly proportional to the absolute values of substrate potential and inversely proportional to the electrolyte concentration. This late response of potential decay does not fit the Gouy-Chapman-Stern theory but could be approximately modelled by the mechanism proposed by Friedl et al., in which SECPM is assumed to function like EC-STM at close tip-sample separation. However, the contribution of tunnelling current and Faradaic current to the potential detected by SECPM tip is highly controversial. More experimental data is required to support the existence of tunnelling current and identify the redox reactions from which the Faradaic current being generated.

SECPM exhibits high reproducibility and reliability in profiling the potential distribution in the EDL. For the first time that potential decay following the prediction of Gouy-Chapman-Stern model was observed in real space. This result provides direct data to study the EDL overlapping and could contribute to the further development of new tools,

both experimental and theoretical, for a better understanding of the EDL structure and the SECPM potential detection mechanism.

References

- Ahirwal, G.K. & Mitra, C. (2009) Direct Electrochemistry of Horseradish Peroxidase-Gold Nanoparticles Conjugate. *Sensors*. 9 (2), 881–894.
- Aicart-Ramos, C., Valhondo Falcón, M., Ortiz de Montellano, P.R. & Rodriguez-Crespo, I. (2012) Covalent attachment of heme to the protein moiety in an insect E75 nitric oxide sensor. *Biochemistry*. 51 (37), 7403–7416.
- Armstrong, F.A. & Wilson, G.S. (2000) Recent developments in faradaic bioelectrochemistry. *Electrochimica Acta*. 45 (15), 2623–2645.
- Baier, C. & Stimming, U. (2009) Imaging Single Enzyme Molecules under In Situ Conditions. *Angewandte Chemie International Edition*. 48 (30), 5542–5544.
- Baker, H.M., Anderson, B.F. & Baker, E.N. (2003) Dealing with iron: Common structural principles in proteins that transport iron and heme. *Proceedings of the National Academy of Sciences*. 100 (7), 3579 LP – 3583.
- Bard, A.J. & Faulkner, L.R. (2001) *Electrochemical Methods: Fundamentals and Applications*. 2nd Editio. Wiley.
- Bard, A.J. & Faulkner, L.R. (2000) *Electrochemical Methods: Fundamentals and Applications*. Second Edi. David Harris & Elizabeth Swain (eds.). John Wiley & Sons, Ltd.
- Bergel, A. & Lai, M.E. (2001) *Catalysis of Oxygen Reduction by Catalase and HRP on Glassy Carbon Electrodes: Comparison of the Mechanisms*. 1998.
- Binnig, G., Quate, C.F. & Gerber, C. (1986) Atomic force microscope. *Physical Review Letters*. 56 (9), 930–933.
- Binnig, G. & Rohrer, H. (1983) Scanning tunnelling microscopy. *Surface Science*. 126 (1–3), 236–244.
- Binnig, G., Rohrer, H., Gerber, C. & Weibel, E. (1982) Surface Studies by Scanning Tunnelling Microscopy. *Physical Review Letters*. 49 (1), 57–61.
- Booth, F. (1955) Dielectric Constant of Polar Liquids at High Field Strengths. *The Journal of Chemical Physics*. 23 (3), 453–457.
- Booth, F. (1951) The Dielectric Constant of Water and the Saturation Effect. *The Journal of Chemical Physics*. 19 (4), 391–394.

- Bowman, S.E.J. & Bren, K.L. (2008) The chemistry and biochemistry of heme c: functional bases for covalent attachment. *Natural product reports*. 25 (6), 1118–1130.
- Brusova, Z., Gorton, L. & Magner, E. (2006) Comment on “Direct Electrochemistry and Electrocatalysis of Heme Proteins Entrapped in Agarose Hydrogel Films in Room-Temperature Ionic Liquids”. *Langmuir*. 22 (26), 11453–11455.
- Carlsson, G.H., Nicholls, P., Svistunenko, D., Berglund, G.I. & Hajdu, J. (2005) Complexes of horseradish peroxidase with formate, acetate, and carbon monoxide. *Biochemistry*. 44 (2), 635–642.
- Chang, H. & Bard, A.J. (1991) Scanning Tunnelling Microscopy Studies of Carbon-Oxygen Reactions on Highly Oriented Pyrolytic Graphite. *Journal of the American Chemical Society*. 113 (15), 5588–5596.
- Chapman, D.L. (1913) LI. A contribution to the theory of electrocapillarity . *The London, Edinburgh, and Dublin Philosophical Magazine and Journal of Science*. 25 (148), 475–481.
- Choi, W., Shin, H.-C., Kim, J.M., Choi, J.-Y. & Yoon, W.-S. (2020) Modeling and Applications of Electrochemical Impedance Spectroscopy (EIS) for Lithium-ion Batteries. *J. Electrochem. Sci. Technol.* 11 (1), 1–13.
- Corbella, C., Pascual, E., Oncins, G., Canal, C., Andújar, J.L. & Bertran, E. (2005) Composition and morphology of metal-containing diamond-like carbon films obtained by reactive magnetron sputtering. *Thin Solid Films*. 482 (1), 293–298.
- Das, S., Chakraborty, S. & Mitra, S.K. (2012) Redefining electrical double layer thickness in narrow confinements: Effect of solvent polarization. *Physical Review E*. 85 (5), 051508.
- Debye, P. (1929) Polar molecules. *Journal of the Society of Chemical Industry*. 48 (43), 1036–10.
- Di, J., Shen, C., Peng, S., Tu, Y. & Li, S. (2005) A one-step method to construct a third-generation biosensor based on horseradish peroxidase and gold nanoparticles embedded in silica sol-gel network on gold modified electrode. *Analytica Chimica Acta*. 553 (1–2), 196–200.
- Dukhin, A.S. & Goetz, P.J. (2017) 'Chapter 2 - Fundamentals of Interface and Colloid

Science, in Andrei S Dukhin & Philip J B T - Characterization of Liquids Goetz Dispersions, Emulsions, and Porous Materials Using Ultrasound (Third Edition) (eds.) [Online]. Elsevier. pp. 19–83.

Dunford, H.B. (2002) Oxidations of iron(II)/(III) by hydrogen peroxide: from aquo to enzyme. *Coordination Chemistry Reviews*. 233–234311–318.

Friedl, J., Gu, J., Stimming, U. & Horrocks, B.R. (2018) On the Mechanism of Scanning Electrochemical Potential Microscopy. *ChemElectroChem*. 5 (1), 25–28.

Fritzen-Garcia, M.B., Zoldan, V.C., Oliveira, I.R.W.Z., Soldi, V., Pasa, A.A. & Creczynski-Pasa, T.B. (2013) Peroxidase immobilized on phospholipid bilayers supported on au (111) by DTT self-assembled monolayers: Application to dopamine determination. *Biotechnology and Bioengineering*. 110 (2), 374–382.

George, S. & Lee, H.K. (2009) Direct Electrochemistry and Electrocatalysis of Hemoglobin in Nafion/Carbon Nanochip Film on Glassy Carbon Electrode. *The Journal of Physical Chemistry B*. 113 (47), 15445–15454.

Ghilane, J., Hapiot, P. & Bard, A.J. (2006) Metal/Polypyrrole Quasi-Reference Electrode for Voltammetry in Nonaqueous and Aqueous Solutions. *Analytical Chemistry*. 78 (19), 6868–6872.

Gouy, M. (1910) Sur la constitution de la charge électrique à la surface d'un électrolyte. *Journal de Physique Théorique et Appliquée*. 9 (1), 457–468.

Grahame, D.C. (1947) The electrical double layer and the theory of electrocapillarity. *Chemical Reviews*. 41 (3), 441–501.

de Groot, M.T., Merks, M. & Koper, M.T.M. (2005) Heme Release in Myoglobin–DDAB Films and Its Role in Electrochemical NO Reduction. *Journal of the American Chemical Society*. 127 (46), 16224–16232.

H., F. (1949) *Theory Of Dielectrics*. Oxford: Clarendon Press.

Hamou, R.F., Biedermann, P.U., Erbe, A. & Rohwerder, M. (2010a) Numerical analysis of Debye screening effect in electrode surface potential mapping by scanning electrochemical potential microscopy. *Electrochemistry Communications*. 12 (10), 1391–1394.

Hamou, R.F., Biedermann, P.U., Erbe, A. & Rohwerder, M. (2010b) Numerical

- simulation of probing the electric double layer by scanning electrochemical potential microscopy. *Electrochimica Acta*. 55 (18), 5210–5222.
- Heering, H.A., Hirst, J. & Armstrong, F.A. (1998) Interpreting the Catalytic Voltammetry of Electroactive Enzymes Adsorbed on Electrodes. *The Journal of Physical Chemistry B*. 102 (35), 6889–6902.
- Helmholtz, H. (1853) Ueber einige Gesetze der Vertheilung elektrischer Ströme in körperlichen Leitern mit Anwendung auf die thierisch-elektrischen Versuche. *Annalen der Physik und Chemie*. 165 (6), 211–233.
- Hillier, A.C., Kirn, S. & Bard, A.J. (1996) Measurement of double-layer forces at the electrode/electrolyte interface using the atomic force microscope: Potential and anion dependent interactions. *Journal of Physical Chemistry*. 100 (48), 18808–18817.
- von Hippel, A.R. & Morgan, S.O. (1955) Dielectrics and Waves. *Journal of The Electrochemical Society*. 102 (3), 68C.
- Hu, K., Chai, Z., Whitesell, J.K. & Bard, A.J. (1999) In situ monitoring of diffuse double layer structure changes of electrochemically addressable self-assembled monolayers with an atomic force microscope. *Langmuir*. 15 (9), 3343–3347.
- Huang, H., Hu, N., Zeng, Y. & Zhou, G. (2002) Electrochemistry and electrocatalysis with heme proteins in chitosan biopolymer films. *Analytical Biochemistry*. 308 (1), 141–151.
- Huang, R. & Hu, N. (2003) Direct voltammetry and electrochemical catalysis with horseradish peroxidase in polyacrylamide hydrogel films. *Biophysical Chemistry*. 104 (1), 199–208.
- Hurth, C., Li, C. & Bard, A.J. (2007) Direct Probing of Electrical Double Layers by Scanning Electrochemical Potential Microscopy. *The Journal of Physical Chemistry C*. 111 (12), 4620–4627.
- Jenner, L.P. & Butt, J.N. (2018) Electrochemistry of surface-confined enzymes: Inspiration, insight and opportunity for sustainable biotechnology. *Current Opinion in Electrochemistry*. 881–88.
- Ji, H., Zhao, X., Qiao, Z., Jung, J., Zhu, Y., Lu, Y., Zhang, L.L., MacDonald, A.H. & Ruoff, R.S. (2014) Capacitance of carbon-based electrical double-layer capacitors.

Nature Communications. 5 (1), 3317.

Jones, P. & Dunford, H.B. (2005) The mechanism of Compound I formation revisited. *Journal of Inorganic Biochemistry*. 99 (12), 2292–2298.

KENDREW, J.C., DICKERSON, R.E., STRANDBERG, B.E., HART, R.G., DAVIES, D.R., PHILLIPS, D.C. & SHORE, V.C. (1960) Structure of Myoglobin: A Three-Dimensional Fourier Synthesis at 2 Å. Resolution. *Nature*. 185 (4711), 422–427.

Kirkwood, J.G. (1939) The dielectric polarization of polar liquids. *The Journal of Chemical Physics*. 7 (10), 911–919.

Kornyshev, A.A. & Kuznetsov, A.M. (2006) Potential distribution in an in situ nano-gap. *Electrochemistry Communications*. 8 (5), 679–682.

Krainer, F.W. & Glieder, A. (2015) An updated view on horseradish peroxidases: recombinant production and biotechnological applications. *Applied Microbiology and Biotechnology*. 99 (4), 1611–1625.

Kremer, F. & Schonhals, A. (2003) EIS 3. *Broadband Dielectric Spectroscopy*. Berlin: Springer Berlin Heidelberg.

Lapshin, R. V (1998) Automatic lateral calibration of tunnelling microscope scanners. *Review of Scientific Instruments*. 69 (9), 3268–3276.

Lee, T.H. (2003) Nyquist plot. *The Design of CMOS Radio-Frequency Integrated Circuits*. 2nd edition. Cambridge: Cambridge University Press.

Léger, C. & Bertrand, P. (2008) Direct Electrochemistry of Redox Enzymes as a Tool for Mechanistic Studies. *Chemical Reviews*. 108 (7), 2379–2438.

Liang, Y., McLaughlin, D., Csoklich, C., Schneider, O. & Bandarenka, A.S. (2019) The nature of active centers catalyzing oxygen electro-reduction at platinum surfaces in alkaline media. *Energy & Environmental Science*. 12 (1), 351–357.

Limoges, B. & Savéant, J.-M. (2004) Catalysis by immobilized redox enzymes. Diagnosis of inactivation and reactivation effects through odd cyclic voltammetric responses. *Journal of Electroanalytical Chemistry*. 562 (1), 43–52.

Liong, E.C., Dou, Y., Scott, E.E., Olson, J.S. & Phillips Jr., G.N. (2001) Waterproofing the Heme Pocket: ROLE OF PROXIMAL AMINO ACID SIDE CHAINS IN PREVENTING HEMIN LOSS FROM MYOGLOBIN *. *Journal of Biological*

- Chemistry*. 276 (12), 9093–9100.
- Liu, Y., Hu, L.M. & Yang, S.Q. (2008) Amplification of bioelectrocatalytic signalling based on silver nanoparticles and DNA-derived horseradish peroxidase biosensors. *Microchimica Acta*. 160 (3), 357–365.
- Lustenberger, P., Rohrer, H., Christoph, R. & Siegenthaler, H. (1988) Scanning tunnelling microscopy at potential controlled electrode surfaces in electrolytic environment. *Journal of Electroanalytical Chemistry*. 243 (1), 225–235.
- Maehly, A.C.B.T.-M. in E. (1955) '[143] Plant peroxidase', in [Online]. Academic Press. pp. 801–813.
- Magonov, S.N. (1993) Surface Characterization of Materials at Ambient Conditions by Scanning Tunnelling Microscopy (STM) and Atomic Force Microscopy (AFM). *Applied Spectroscopy Reviews*. 28 (1–2), 1–121.
- Mano, N. & de Poulpiquet, A. (2018) O₂ Reduction in Enzymatic Biofuel Cells. *Chemical Reviews*. 118 (5), 2392–2468.
- Masa, J. & Schuhmann, W. (2016) Electrocatalysis and bioelectrocatalysis – Distinction without a difference. *Nano Energy*. 29466–475.
- Matsumoto, M., Manako, T. & Imai, H. (2009) Electrochemical STM Investigation of Oxidative Corrosion of the Surface of Highly Oriented Pyrolytic Graphite. *Journal of The Electrochemical Society*. 156 (10), B1208.
- Mazurenko, I., de Poulpiquet, A. & Lojou, E. (2017) Recent developments in high surface area bioelectrodes for enzymatic fuel cells. *Current Opinion in Electrochemistry*. 5 (1), 74–84.
- McCann, M.M. (2004) *Nanoindentation-of-Gold-Single-Crystals*. [Online]. Virginia Tech.
- Michel, H., Behr, J., Harrenga, A. & Kannt, A. (1998) CYTOCHROME C OXIDASE: Structure and Spectroscopy. *Annual Review of Biophysics and Biomolecular Structure*. 27 (1), 329–356.
- Milton, R.D. & Minteer, S.D. (2017) Direct enzymatic bioelectrocatalysis: differentiating between myth and reality. *Journal of The Royal Society Interface*. 14 (131), 20170253.

- Müller, T., Werblowsky, T.L., Florio, G.M., Berne, B.J. & Flynn, G.W. (2005) Ultra-high vacuum scanning tunnelling microscopy and theoretical studies of 1-halohexane monolayers on graphite. *Proceedings of the National Academy of Sciences of the United States of America*. 102 (15), 5315 LP – 5322.
- Niu, Y., Liu, J., Chen, W., Yin, C., Weng, W., Li, X., Wang, X., Li, G. & Sun, W. (2018) A direct electron transfer biosensor based on a horseradish peroxidase and gold nanotriangle modified electrode and electrocatalysis. *Analytical Methods*. 10 (44), 5297–5304.
- Nonnenmacher, M., O'Boyle, M.P. & Wickramasinghe, H.K. (1991) Kelvin probe force microscopy Sascha Sadewasser & Thilo Glatzel (eds.). *Applied Physics Letters*. 58 (25), 2921–2923.
- Onsager, L. (1936) Electric Moments of Molecules in Liquids. *Journal of the American Chemical Society*. 58 (8), 1486–1493.
- Otake, Y. & Jenkins, R.G. (1993) Characterization of oxygen-containing surface complexes created on a microporous carbon by air and nitric acid treatment. *Carbon*. 31 (1), 109–121.
- Pandey, V.P., Awasthi, M., Singh, S., Tiwari, S. & Dwivedi, U.N. (2017) A Comprehensive Review on Function and Application of Plant Peroxidases. *Biochemistry & Analytical Biochemistry*. 06 (01), 1–16.
- Pankratov, D., Sotres, J., Barrantes, A., Arnebrant, T. & Shleev, S. (2014) Interfacial behavior and activity of laccase and bilirubin oxidase on bare gold surfaces. *Langmuir*. 30 (10), 2943–2951.
- Patel, N., Davies, M.C., Heaton, R.J., Roberts, C.J., Tendler, S.J.B. & Williams, P.M. (1998) A scanning probe microscopy study of the physisorption and chemisorption of protein molecules onto carboxylate terminated self-assembled monolayers. *Applied Physics A: Materials Science and Processing*. 66 (SUPPL. 1), 569–574.
- PERUTZ, M.F., ROSSMANN, M.G., CULLIS, A.N.N.F., MUIRHEAD, H., WILL, G. & NORTH, A.C.T. (1960) Structure of Hæmoglobin: A Three-Dimensional Fourier Synthesis at 5.5-Å. Resolution, Obtained by X-Ray Analysis. *Nature*. 185 (4711), 416–422.
- Pope, M.A., Punckt, C. & Aksay, I.A. (2011) Intrinsic Capacitance and Redox Activity

- of Functionalized Graphene Sheets. *The Journal of Physical Chemistry C*. 115 (41), 20326–20334.
- Poulos, Thomas L (2014) Heme enzyme structure and function. *Chemical reviews*. 114 (7), 3919–3962.
- Poulos, Thomas L. (2014) Heme Enzyme Structure and Function. *Chemical Reviews*. 114 (7), 3919–3962.
- Rabe, M., Verdes, D. & Seeger, S. (2011) Understanding protein adsorption phenomena at solid surfaces. *Advances in Colloid and Interface Science*. 162 (1–2), 87–106.
- Randin, J.-P. & Yeager, E. (1971) Differential Capacitance Study of Stress-Annealed Pyrolytic Graphite Electrodes. *Journal of The Electrochemical Society*. 118 (5), 711.
- Randles, J.E.B. (1947) Kinetics of rapid electrode reactions. *Faraday Discussions*. 111–19.
- Ranieri, A., Bortolotti, C.A., Rocco, G. Di, Battistuzzi, G., Sola, M. & Borsari, M. (2019) Electrocatalytic Properties of Immobilized Heme Proteins: Basic Principles and Applications. *ChemElectroChem*. 6 (20), 5172–5185.
- Roberts, W.S., Davis, F., Collyer, S.D. & Higson, S.P.J. (2011) Construction and interrogation of enzyme microarrays using scanning electrochemical microscopy - Optimisation of adsorption and determination of enzymatic activity. *Analyst*. 136 (24), 5287–5293.
- Roquet, L., Belgsir, E.M., Léger, J.-M. & Lamy, C. (1994) Kinetics and mechanisms of the electrocatalytic oxidation of glycerol as investigated by chromatographic analysis of the reaction products: Potential and pH effects. *Electrochimica Acta*. 39 (16), 2387–2394.
- Ruzgas, T., Csöregi, E., Emnéus, J., Gorton, L. & Marko-Varga, G. (1996) Peroxidase-modified electrodes: Fundamentals and application. *Analytica Chimica Acta*. 330 (2–3), 123–138.
- Scheel, H.J., Binning, G. & Rohrer, H. (1982) Atomically flat LPE-grown facets seen by scanning tunnelling microscopy. *Journal of Crystal Growth*. 60 (1), 199–202.

- Senda, M. & Delahay, P. (1961) Electrode processes with specific or non-specific adsorption: Faradaic impedance and rectification. *Journal of Physical Chemistry*. 65 (9), 1580–1588.
- Sheng, Q.-L., Zheng, J.-B., Shang-Guan, X.-D., Lin, W.-H., Li, Y.-Y. & Liu, R.-X. (2010) Direct electrochemistry and electrocatalysis of heme-proteins immobilized in porous carbon nanofiber/room-temperature ionic liquid composite film. *Electrochimica Acta*. 55 (9), 3185–3191.
- Shi, F., Zheng, W., Wang, W., Hou, F., Lei, B., Sun, Z. & Sun, W. (2015) Application of graphene–copper sulfide nanocomposite modified electrode for electrochemistry and electrocatalysis of hemoglobin. *Biosensors and Bioelectronics*. 64131–137.
- Shivakumar, A., BG, J. & MR, D. (2017) Role of Peroxidase in Clinical Assays: A Short Review. *Journal of Clinical Nutrition & Dietetics*. 03 (02), 1–7.
- Sluyters-Rhbach, M. & Sluyters, J.H. (1970) equivalent circuit. *Electroanalytical Chemistry, Vol. 4*. 2nd edition. Allen J. Bard (ed.). New York: Marcel Dekker.
- SONNENFELD, R. & HANSMA, P.K. (1986) Atomic-Resolution Microscopy in Water. *Science*. 232 (4747), 211–213.
- Sonnenfeld, R., Schneir, J., Drake, B., Hansma, P.K. & Aspnes, D.E. (1987) Semiconductor topography in aqueous environments: Tunnelling microscopy of chemomechanically polished (001) GaAs. *Applied Physics Letters*. 50 (24), 1742–1744.
- Stern, O. (1924) Zur Theorie der Elektrolytischen Doppelschicht. *Zeitschrift fur Elektrochemie*. 30508–516.
- Sun, Y.X., Zhang, J.T., Huang, S.W. & Wang, S.F. (2007) Hydrogen peroxide biosensor based on the bioelectrocatalysis of horseradish peroxidase incorporated in a new hydrogel film. *Sensors and Actuators, B: Chemical*. 124 (2), 494–500.
- Tao, K., Makam, P., Aizen, R. & Gazit, E. (2017) Self-assembling peptide semiconductors. *Science (New York, N.Y.)*. 358 (6365), eaam9756.
- Tertis, M., Florea, A., Sandulescu, R. & Cristea, C. (2013) Carbon based electrodes modified with horseradish peroxidase immobilized in conducting polymers for

- acetaminophen analysis. *Sensors (Switzerland)*. 13 (4), 4841–4854.
- Todorovic, S., Jung, C., Hildebrandt, P. & Murgida, D.H. (2006) Conformational transitions and redox potential shifts of cytochrome P450 induced by immobilization. *JBIC Journal of Biological Inorganic Chemistry*. 11 (1), 119–127.
- Traunsteiner, C., Tu, K. & Kunze-Liebhäuser, J. (2015) High-Resolution Imaging of the Initial Stages of Oxidation of Cu(111) with Scanning Electrochemical Potential Microscopy. *ChemElectroChem*. 2 (1), 77–84.
- Viswanathan, R. & Heaney, M.B. (1995) Direct Imaging of the Percolation Network in a Three-Dimensional Disordered Conductor-Insulator Composite. *Physical Review Letters*. 75 (24), 4433–4436.
- Volkov, A.A. & Prokhorov, A.S. (2003) Broadband Dielectric Spectroscopy of Solids. *Radiophysics and Quantum Electronics*. 46 (8), 657–665.
- WANG, E., WANG, H. & LI, Z. (2000) Protein Structural Characterization by Scanning Tunnelling Microscopy with Electrochemistry. *Analytical Sciences*. 16 (2), 205–209.
- Wang, M., Bugarski, S. & Stimming, U. (2008a) Probing single flavoprotein molecules on graphite in aqueous solution with scanning tunnelling microscopy. *Small*. 4 (8), 1110–1114.
- Wang, M., Bugarski, S. & Stimming, U. (2008b) Topological and Electron-Transfer Properties of Glucose Oxidase Adsorbed on Highly Oriented Pyrolytic Graphite Electrodes. *The Journal of Physical Chemistry C*. 112 (13), 5165–5173.
- Wang, Z., Luo, X., Wan, Q., Wu, K. & Yang, N. (2014) Versatile Matrix for Constructing Enzyme-Based Biosensors. *ACS Applied Materials & Interfaces*. 6 (19), 17296–17305.
- Welinder, K.G., Smillie, L.B. & Schonbaum, G.R. (1972) Amino Acid Sequence Studies of Horseradish Peroxidase. I. Tryptic Peptides. *Canadian Journal of Biochemistry*. 50 (1), 44–62.
- Westerhoff, U., Kurbach, K., Lienesch, F. & Kurrat, M. (2016) Analysis of Lithium-Ion Battery Models Based on Electrochemical Impedance Spectroscopy. *Energy Technology*. 4 (12), 1620–1630.

- Wiggins-Camacho, J.D. & Stevenson, K.J. (2009) Effect of Nitrogen Concentration on Capacitance, Density of States, Electronic Conductivity, and Morphology of N-Doped Carbon Nanotube Electrodes. *The Journal of Physical Chemistry C*. 113 (44), 19082–19090.
- Wolfschmidt, H., Baier, C., Gsell, S., Fischer, M., Schreck, M. & Stimming, U. (2010) STM, SECPM, AFM and electrochemistry on single crystalline surfaces. *Materials*. 3 (8), 4196–4213.
- Woo, D.H., Yoo, J.S., Park, S.M., Jeon, I.C. & Kang, H. (2004) Direct Probing into the Electrochemical Interface Using a Novel Potential Probe: Au(111) Electrode/NaBF₄ Solution Interface. *Bulletin of the Korean Chemical Society*. 25 (4), 577–580.
- Wroblowa, H.S., Yen-Chi-Pan & Razumney, G. (1976) Electroreduction of oxygen: A new mechanistic criterion. *Journal of Electroanalytical Chemistry and Interfacial Electrochemistry*. 69 (2), 195–201.
- Wu, J., Wang, Y., Zhang, D. & Hou, B. (2011) Studies on the electrochemical reduction of oxygen catalyzed by reduced graphene sheets in neutral media. *Journal of Power Sources*. 196 (3), 1141–1144.
- Wu, Y., Shen, Q. & Hu, S. (2006) Direct electrochemistry and electrocatalysis of heme-proteins in regenerated silk fibroin film. *Analytica Chimica Acta*. 558 (1), 179–186.
- Yarlagadda, R.K.R. (2010) Bode Plot. *Analog and Digital Signals and Systems*. Boston, MA: Springer US.
- Yoon, Y.H., Woo, D.H., Shin, T., Chung, T.D. & Kang, H. (2011) Real-space investigation of electrical double layers. Potential gradient measurement with a nanometer potential probe. *Journal of Physical Chemistry C*. 115 (35), 17384–17391.
- Yu, J. & Ju, H. (2002) Preparation of porous titania sol-gel matrix for immobilization of horseradish peroxidase by a vapor deposition method. *Analytical Chemistry*. 74 (14), 3579–3583.
- Yuan, R., Liu, Y., Li, Q.F., Chai, Y.Q., Mo, C.L., Zhong, X., Tang, D.P. & Dai, J.Y. (2005) Electrochemical characteristics of a platinum electrode modified with a matrix of polyvinyl butyral and colloidal Ag containing immobilized horseradish peroxidase. *Analytical and Bioanalytical Chemistry*. 381 (3), 762–768.

- Zhang, J., Chi, Q., Dong, S. & Wang, E. (1996) In situ electrochemical scanning tunnelling microscopy investigation of structure for horseradish peroxidase and its electric catalytic property. *Bioelectrochemistry and Bioenergetics*. 39 (2), 267–274.
- Zhang, Y., He, P. & Hu, N. (2004) Horseradish peroxidase immobilized in TiO₂ nanoparticle films on pyrolytic graphite electrodes: direct electrochemistry and bioelectrocatalysis. *Electrochimica Acta*. 49 (12), 1981–1988.
- Zhao, Y.-D., Zhang, W.-D., Chen, H., Luo, Q.-M. & Li, S.F.Y. (2002) Direct electrochemistry of horseradish peroxidase at carbon nanotube powder microelectrode. *Sensors and Actuators B: Chemical*. 87 (1), 168–172.
- Zhou, J., Campbell, C., Heller, A. & Bard, A.J. (2002) Scanning electrochemical microscopy. 44. Imaging of horseradish peroxidase immobilized on insulating substrates. *Analytical Chemistry*. 74 (16), 4007–4010.
- Zou, Y., Walton, A.S., Kinloch, I.A. & Dryfe, R.A.W. (2016) Investigation of the Differential Capacitance of Highly Ordered Pyrolytic Graphite as a Model Material of Graphene. *Langmuir*. 32 (44), 11448–11455.